NORTHWESTERN UNIVERSITY

MITIGATING MAGNETIC FIELD IMPERFECTIONS FOR PRECISION MEASUREMENT OF THE ELECTRON ELECTRIC DIPOLE MOMENT

A DISSERTATION

SUBMITTED TO THE GRADUATE SCHOOL
IN PARTIAL FULFILLMENT OF THE REQUIREMENTS

for the degree

DOCTOR OF PHILOSOPHY

Field of Physics

By

Siyuan Liu

EVANSTON, ILLINOIS

May 2024

ABSTRACT

Searches for the electron electric dipole moment (eEDM) sensitively probe for physics beyond the Standard Model that are time-reversal violating interactions. The ACME Collaboration increased the eEDM sensitivity by a factor of 100 six years ago, and a recent measurement by the JILA eEDM group increased the sensitivity by an additional factor of 2.5, to $|d_e| < 4.1 \times 10^{-30}\, e \cdot \mathrm{cm}$. The third generation of the Advanced Cold Molecule Electron EDM experiment (ACME III) aims to enhance the sensitivity to the electron EDM by more than an additional order of magnitude. A critical challenge in ACME III is the precise control of the magnetic fields and gradients that significantly influence both systematic and statistical uncertainties. The described design, construction and performance of a magnetic shield and field coil achieves a residual magnetic field below $10\,\mu$G and field uniformity better than $1\,\mu$G/cm as of this writing, without residual magnetization building up caused by magnetic fields that must be produced and reversed in the shielded volume. This apparatus, combined with a longer coherence time and an increased signal, position ACME III to probe new physics at energy scales of tens of TeV, comparable and even well above the reach of the Large Hadron Collider (LHC).

ACKNOWLEDGEMENTS

As I reflect on the past six years of my work towards the next generation of an electron EDM measurement, I am overwhelmed by the realization that this journey would have been impossible without the support of my supervisor, colleagues, friends, and family. I have been incredibly fortunate to collaborate with numerous talented individuals, and I express my deepest gratitude to all who have contributed to creating such an enriching environment for learning and discovery.

First and foremost, I extend my heartfelt appreciation to my advisor, Professor Gerald (Jerry) Gabrielse. His guidance, support, and encouragement have been instrumental throughout my Ph.D. studies. Jerry's consistent provision of invaluable advice and insights, coupled with his unwavering patience during my moments of struggle, has been truly remarkable. I consider myself exceptionally fortunate to have had the opportunity to work under his mentorship.

I am also deeply grateful to the co-advisors in the ACME collaboration: Professor John Doyle (Harvard University) and Professor David DeMille (University of Chicago). Their expertise and insights have been invaluable, and I have thoroughly enjoyed our thought-provoking discussions.

My sincere thanks go to my committee members, Professor Michael Schmitt and Professor Timothy Kovachy. Their well-structured lectures in the courses I attended during my early years laid a solid foundation for my research. I am also appreciative of their insightful comments and suggestions on my work, from the candidacy exam to the final defense.

This work would not have been possible without the support and assistance of my colleagues in the Gabrielse group and the ACME collaboration. I am indebted to Xing Fan for imparting laboratory skills and providing "impedance matching" both as a senior student and as a research professor. My heartfelt thanks to Peiran Hu, Zhen Han, Ayami Hiramoto, Maya Watts, Collin Diver, and Takahiko Masuda for their valuable discussions, unwavering support, and tireless efforts

in completing the experiment. I also express my gratitude to the former members of the group who significantly contributed to my training and development in the early stages of my Ph.D. study: Cole Meisenhelder, Daniel Ang, Xing Wu, Cris Panda, John Mitchell, and many others. Thank you all for being both friends and colleagues.

I would like to acknowledge other members of the Gabrielse group who have made working in the lab a pleasant experience and have shared in the challenge of building the most complex experiments: Benedict Sukra, Andra Ionescu, Nathaniel McDonough, Tom Myers, and many others.

While it is challenging to list all names, I extend my thanks to all my friends for accompanying me through the highs and lows of graduate school and life in the US. I have learned immensely from their dedication, consistency, and passion for life.

Last, but certainly not least, I am profoundly grateful to my family for their unconditional love and support. I feel incredibly fortunate to have Bingjie Hao, my wife, who shared this journey as my lab mate in the early years. Her dedication to her own work and her unwavering support of mine have been a constant source of inspiration. I am also deeply thankful to my parents, whose encouragement, wisdom, and love have been a steadfast presence. Our countless conversations have been instrumental in helping me navigate the challenges of doctoral studies.

To all who have contributed to this journey, whether named or unnamed, I offer my sincerest gratitude. This work is as much a testament to your support as it is to my efforts.

TABLE OF CONTENTS

LIST OF TABLES

LIST OF FIGURES

LIST OF PUBLICATIONS

The results of this dissertation are the subject of the following references:

1. **S. Liu**, M. Watts, D. G. Ang, B. Hao, C. Meisenhelder, C. Diver, D. Lascar, A. Hiramoto, T. Masuda, P. Hu, Z. Han, X. Wu, D. DeMille, J.M. Doyle, X. Fan, and G. Gabrielse, **Compact Actively-Shielded Magnetic Field Coil within Mu-Metal Shields**. (under review).

CHAPTER 1

INTRODUCTION

The Standard Model (SM) has remained one of the greatest triumphs [1] in modern physics since its inception in the mid-20th century. It is built on decades of theoretical advancements and experimental validations, including the initial development of electroweak gauge symmetry [2, 3] and the independent discoveries of asymptotic freedom [4]. With the advancement of modern accelerator technologies, constituents in the Standard Model have been discovered one after the other, including the charm quark in 1974 [5], the τ lepton in 1975 [6], the bottom quark in 1977 [7], the gluons in 1979 [8], the W and Z bosons in 1983 [9, 10], the top quark in 1995 [11], the τ neutrino in 2001 [12], and eventually, the Higgs Boson in 2012 [13, 14]. Predictions from the Standard Model has also been tested to extrodinary part-per-trillion precision, with one of the most notable examples being the precision measurement of the electron magnetic moment [15]. The Standard Model remains extraordinarily successful, withstanding decades of increasingly precise tests across a vast range of energy scales, with emerging tensions like the muon g-2 result potentially pointing towards exciting new frontiers in physics.

Despite its successes, the Standard Model, in conjunction with general relativity, does not offer a complete description of the universe. Anomalies observed in the cosmological structures and phenomena, such as the galatic rotation curves [16] and the gravitational lensing observations [17], suggest the existance of dark matter, which remain unexplained within the SM framework. New physics scenarios including supersymmetry [18], light axions [19], and modifications to general relativity [20] have been proposed to address these discrepancies.

1.1 The electric dipole moment and fundamental symmetries in the universe

One particular challenge to the Standard Model (SM) is the matter-antimatter asymmetry. According to the SM, the universe was created with essentially equal amounts of matter and antimatter during Big Bang [21]. However, observations within our solar system and across the observable universe consistently show only trace amounts of antimatter.

1.1.1 Discrete symmetries in universe

In order to understand this problem, we must first consider the three discrete symmetries: charge conjugation (C), parity reversal (P), and time reversal (T):

- Charge conjugation (C) is the transformation that changes a particle to its antiparticle, $\psi \to \bar{\psi}$.
- Parity reversal (P) is the transformation that inverts the spatial coordinates, $(x, y, z) \to -(x, y, z)$.
- Time reversal (T) is the transformation that inverts the direction of time, $t \to -t$.

The C, P and T transformations are not individual symmetries of the Standard Model (SM). Indeed, violations of all three symmetries have been observed. The initial evidence emerged in

1957 with the detection of P violation in the β-decay of ^{60}Co during the famous C. S. Wu experiment [22]. Following this discovery, investigations expanded to include CP violation, where CP represents the combined symmetry operations of C and parity P. CP violation was first observed in the decay processes of the K meson [23], and subsequently in B [24] and D mesons [25]. Further instances of CP violation [26] and T violation [27] have since been recorded.

Although C, P and T are not symmetries of the Standard Model, the combination of CPT was posited to be an exact symmetry. This CPT theorem is based on Lorentz invariance and the spin statistics of the fundamental particles, thus any violation of CPT would entail significant implications [28]. While there are theoretical frameworks that propose CPT violations [29], empirical tests have not detected any violations of CPT across various sectors [30, 31]. As a result, within the framework where CPT symmetry is preserved, any observed CP violations necessitate corresponding T violations to uphold the overall CPT symmetry.

1.1.2 Conditions for matter-antimatter asymmetry

To create an asymmetry between matter and antimatter, the four Sakharov conditions must be met [32]:

1. Baryon number B must be violated.
2. Charge conjugation (C) symmetry must be violated.
3. Charge-parity (CP) violation, also implying time reversal (T) violation if CPT symmetry holds, is required.
4. The early universes evolution must be out of thermal equilibrium. In equilibrium, matter and antimatter, having identical masses, would be produced in equal amounts due to their equal Boltzmann factors, $\exp[-m_\psi c^2/kT]$ and $\exp[-m_{\bar{\psi}} c^2/kT]$.

In the Standard Model, the parity violation is ubiquitous because W bosons interact only with left-handed matter fields, while the degree of chirality in interactions with Z bosons is parametrized by the Weinberg angle $\sin^2\theta_W \approx 0.23$ [33]. As a result, P violation is not a limiting ingredient for the four conditions above in the SM. On the other hand, T violation in the SM is notably limited. The recognized sources of T violation, which are equivalent to CP violation, include the complex phase in the Cabibbo-Kobayashi-Maskawa (CKM) matrix for weak interactions [34], and a similar Pontecorvo-Maki-Nakagawa-Sakata (PMNS) matrix for neutrino mixing. Additionally, T violation in strong interactions, represented by the θ_{QCD} parameter, is stringently constrained by experimental data, with its exceptionally small value of less than 10^{-10} [35], leading to what is known as the strong CP problem. The cumulative effect of these violations falls short of accounting for the observed matter-antimatter asymmetry in the universe. Consequently, an additional source of CP violation beyond what is currently described by the SM is necessary to fully explain this asymmetry.

1.1.3 Probing T violation with electrons

The Electric dipole moment (EDM) of a fundamental particle provides a great tool to search for T violations beyond the Standard Model. The EDM, denoted as $\mathbf{d}$, interacts with an electric field $\mathbf{E}$ via the Hamiltonian $H_d = -\mathbf{d}\cdot\mathbf{E}$, where $\mathbf{E}$ is an electric field. Classically, if two electric charges $+q$ and $-q$ are separated by a distance l, there is an EDM $d = ql$ pointing from the negative to the positive charge. This system thus would have lower energy if $\mathbf{d}$ is aligned with applied electric field $\mathbf{E}$, and higher energy if $\mathbf{d}$ is anti-aligned with $\mathbf{E}$.

For fundamental particles like electrons, the situation differs significantly; Spin is the only intrinsic vector allowed. If this were not the case, an alternative to Pauli's exclusion principle would be required, where the spin and another internal degree of freedom would determine the internal state of a particle. For the electrons present in every atom in the world, such a scenario is inconsistent with extensive observations in atomic physics. Therefore, the EDM of an electron must align with its spin vector, either parallel or anti-parallel, just in the same way as its magnetic moment. As demonstrated in Figure 1.1, both P and T transformation would resulting in an electron with its EDM *parallel* to it spin become an electron with its EDM *anti-parallel* to its spin, which is intrinsically different from the original state. Thus, the existance of a non-zero EDM of an electron would be a clear indication of both P and T violation. [36].

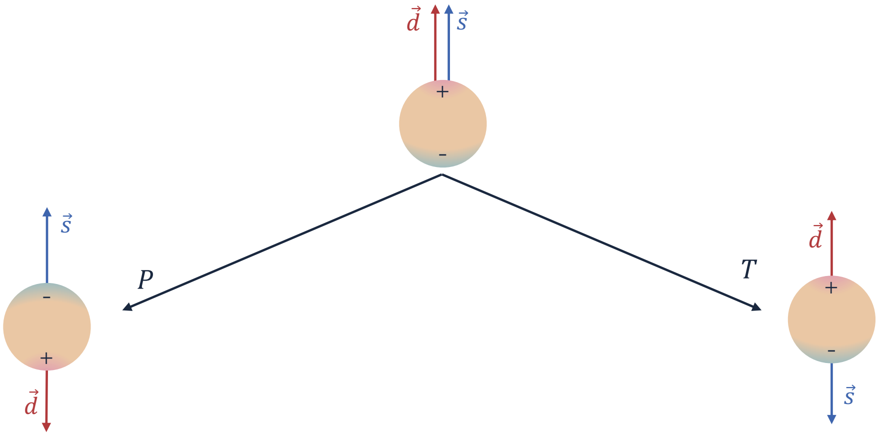

Figure 1.1: **The discreate symmetries of electrons.** The original electron is distinguishable from the result of both P and T transformations so a non-zero electron EDM must violate P and T symmetry.

The T violation contained in the SM is strictly limited. T violations in the CKM matrix that could affect electron properties are only mediated by quarks and W bosons, leading to the lowest non-zero contribution to the electron EDM being a three-loop Feynman diagram. Moreover, Khriplovich and Pospelov demonstrated that all three-loop diagrams exactly cancel out [37]; the largest contribution for the electron EDM, arising from four-loop diagrams involving the CP-violating phase in the CKM matrix, is $|d_e| \sim 6 \times 10^{-40}\, e \cdot$ cm [38], approximately ten orders of magnitude below the current experimental sensitivity. Another source of the T violation in the

SM, the strong CP-violating phase θ_{QCD}, is constraint to be $|d_e| < 10^{-38}\, e \cdot \mathrm{cm}$ by the measurement of neutron EDMs [39, 40] (because neutron's greater mass makes it more sensitive to these effects). Contributions from CP violations in the neutrino sector are considered negligible due to the neutrinos' extremely small mass.

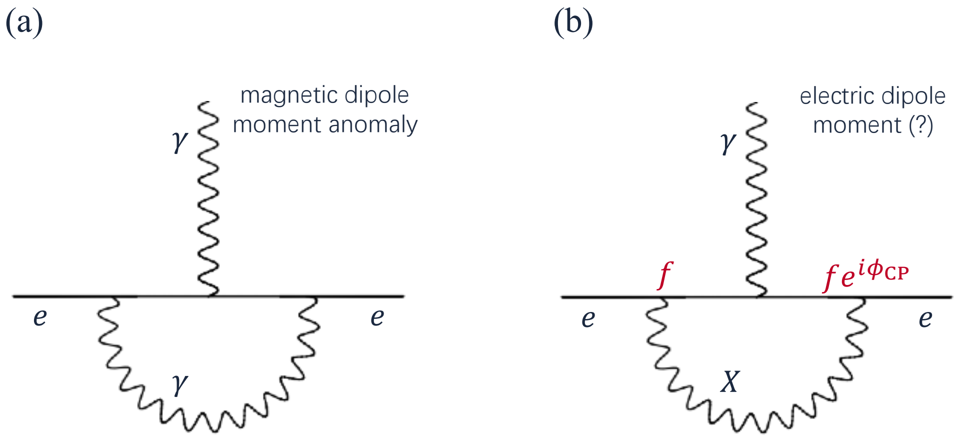

Figure 1.2: **Feynman diagrams for generating electron's dipole moments.** (a) Leading-order contribution of the anomalous magnetic moment of the electron. (b) A simple example of leading-order contribution to the electron EDM from a particle beyond the Standard Model, with intrinsic CP-violating phase ϕ_{CP}.

Various theories that extend beyond the Standard Model predict the existence of a non-zero electron EDM. they generally propose an unknown new particle that interacts with the electron. The particle has a mass m_X, engages with the electron through a coupling coefficient f, and incorporates an intrinsic CP-violating phase ϕ_{CP}. In this case, the electron is working as a "quantum sensor" that captures the traces of virtual particles that couples to it, and reflect all the CP-violating effects in its EDM. The interaction responsible for generating the electron EDM occurs between the electron and this new particle X as shown in Figure 1.2 (b). For comparison, a reference diagram illustrating the leading-order contribution to the electron's anomalous magnetic moment is presented in Figure 1.2 (a). One might be surprised to see the similarities between the two diagrams, and would expect a similar expression for these two diagrams. The result for the electron's anomalous magnetic moment, $\frac{\mu_a}{2} = (\frac{\alpha}{2\pi})\mu_{\rm B}$, is famously calculated by Julian Schwinger [41]. Thus, the contributions in d_e from Figure 1.2 (b) is then approximately [35, 42]:

$$d_e \sim \left[\left(\frac{f}{e}\right)^2 \sin\phi_{\rm CP}\left(\frac{m_e}{m_X}\right)^2\right]\left(\frac{\alpha}{2\pi}\right)\left(\frac{\mu_{\rm B}}{c}\right) \sim 10^{-3}\left(\frac{m_e}{m_X}\right)^2\left(\frac{\mu_{\rm B}}{c}\right) \tag{1.1}$$

where the square braces provide the scaling relative to the anomalous magnetic dipole moment and the EDM of the electron, naively assuming $\frac{f}{e} \sim 1$ and $\phi_{\rm CP} \sim 1$. If we take the current experimental limit of $d_e < 4.1 \times 10^{-30}\, e\cdot$cm [43], we can infer that the new particle X should have a mass scale of $m_X \sim 38\,$TeV. This is extraordinary compared to the energy scales accessible by the Large Hadron Collider (LHC) at CERN, which has a center-of-mass energy of $14\,$TeV [44].

Note that, this approach relies on simplistic assumptions about unknown physical parameters and is model-dependent. It is specifically designed to probe processes that violate CP symmetry and have direct interactions with the electron, which is only a small subset of particle physics. The results presented here pertain to a single-loop contribution. However, it's possible that CP-violating new physics could also manifest at higher loop orders, which would adhere to the scaling outlined in Eq. 1.2, where n represents the loop order [28]:

$$d_e \sim \left[\left(\frac{f}{e}\right)^2 \sin\phi_{\rm CP}\left(\frac{m_e}{m_X}\right)^2\right]\left(\frac{\alpha}{2\pi}\right)^n\left(\frac{\mu_{\rm B}}{c}\right) \tag{1.2}$$

Such scaling implies that a two-loop contribution could correspond to an $m_X \sim 1.3\,$TeV for the current experimental limit on d_e. Nevertheless, the search for the electron EDM remains a potent method for investigating CP-violating new physics beyond the Standard Model and complements direct searches being conducted at the LHC.

1.2 Measuring the electron EDM

1.2.1 EDM of a bound electron system

Free electrons are unsuitable for precise eEDM searches, because the $\mathbf{E}$ needed to create the EDM interaction would accelerate the electron, which would drastically reduce their available measurement time. This necessitates the use of bound electrons to achieve meaningful observation duration. However, for the bound electrons, the electrostatic binding within the atom or molecule ensures that the net electric field experienced by the electron remains zero, despite the application of an external electric field. The Hamiltonian associated with the EDM interaction would become zero for any electronic state with fixed electron spin: $\langle H_{\mathrm{de}}\rangle = -\langle \mathbf{d}_e \cdot \mathbf{E}\rangle = -\mathbf{d}_e \cdot \langle \mathbf{E}\rangle = 0$, with $\langle \mathbf{E}\rangle = 0$ as a result for the electron's electrostatic binding. This result is known as Schiff's theorem, with a more rigorous derivation from Dirac equation in [45].

It is possible to evade Schiff's theorem and measure meaningful EDMs in a bound system, if relativistic effects are considered, as demonstrated by the pioneering work of Sandars [46]. Relativistic effects cause the contraction of the dipole moment vector $\mathbf{d}_e$ along the electron's momentum direction, which varies with the electron's position within the nucleus's Coulomb potential. Consequently, $\langle \mathbf{d}_e \cdot \mathbf{E}\rangle \neq \langle \mathbf{d}_e\rangle \cdot \langle \mathbf{E}\rangle$, allowing for a nonzero first-order energy shift in an electrostatically bound state [47]. The effective electric field in such scenarios, defined as $E_{\text{eff}} = \langle \mathbf{d}_e \cdot \mathbf{E}\rangle$, often significantly exceeds the magnitude of any applied laboratory field. As one would expect for a relativistic effect, E_{eff} scales with $\alpha^2 Z^3$, where α is the fine-structure constant and Z is the atomic number of the nucleus. Heavy atoms are more sensitive to the electron EDM, making them ideal candidates for EDM measurements.

In the context of bound systems such as atoms or molecules, it is worth noticing that the eEDM measured in these systems, admits an alternative interpretation. Generally, the measured energy shift is more accurately described by the equation [48, 49, 36]:

$$U = -d_e E_{\text{eff}} + W_S C_S \tag{1.3}$$

Where C_S is a dimensionless electron-nucleon coupling parameter that also violates time-reversal symmetry (T), and W_S is a constant specific to the species under study. In calculating the EDM value, it is conventionally assumed that $C_S = 0$. However, it is equally plausible to interpret the measured shifts assuming $d_e = 0$. Applying this interpretation to the current best measurement on eEDM, one would infer $|C_S| < 4.5 \times 10^{-10}$ at a 90% confidence level [43].

Despite these considerations, SM constraints on such semi-leptonic interactions are significantly tighter, with recent results placing constraints on $C_S \sim 6.9 \times 10^{-16}$ at leading order (LO) and next-to-leading order (NLO) [36]. This corresponds to an effective electron EDM (d_e) of approximately $1 \times 10^{-35}\, e \cdot$cm. Notably, these figures are still about five orders of magnitude below the current experimental limits and nearly all theoretical predictions beyond SM. However, for many BSM theories, the expected effect of C_S is typically smaller. If we intepret the measured eEDM as from the contribution of C_S, the energy scale for new physics that creates these effect would be on the order of $\sim 10^5$ TeV [50].

1.2.2 General measurement technique and sensitivity limits

The electric dipole moment (EDM) Hamiltonian $H_{\text{de}} = -\mathbf{d}_e \cdot \mathbf{E}$ has a similar form to the magnetic dipole moment Hamiltonian $H_\mu = -\mu \cdot \mathbf{B}$. In 1950, Norman Ramsey pioneered the separated oscillatory fields technique to measure nuclear magnetic moments [51], and suggested that atomic systems would be used to measure eEDM [52]. Since then, Ramsey's scheme has been adapted in most of the eEDM experiments today. This method proceeds the measurement in five steps:

1. A particle beam is prepared in an eigenstate along the z-axis of the Bloch sphere, typically using a magnetic state selector to deflect undesired spin projections.
2. A $\pi/2$ pulse is applied by an electromagnetic field oscillating at frequency ω, creating a coherent superposition of the two eigenstates in the xy-plane of the Bloch sphere.
3. The particles traverse a region with a constant field along the z-axis, causing the state to precess in the xy-plane at the Larmor frequency ω_L.
4. Another $\pi/2$ pulse at frequency ω maps the azimuthal angle (precession phase) of the Bloch sphere onto the polar angle (state population), based on the frequency difference $\omega_L - \omega$.
5. The population of each state is recorded, for example, by another magnetic state selector, allowing for a precise determination of the precession frequency ω_L.

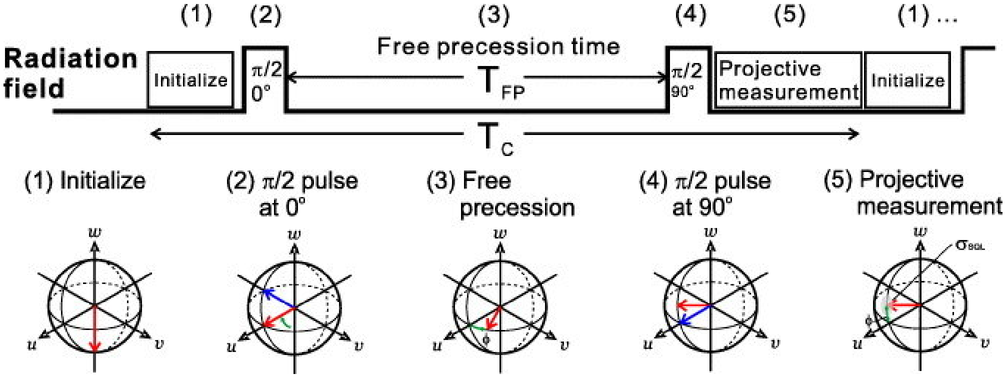

Figure 1.3: **A demonstration of the Ramsey scheme.** The Ramsey sequence is a common technique for measuring the precession frequency of a quantum system. The eEDM measurement is based on the change in precession frequency when the spin direction is reversed relative to the electric field. The red arrow is the spin vector, and the blue arrow is the torque vector that rotates the spin. Adapted from [53].

Figure 1.3 visually demonstrates the process of a classical Ramsey sequence. Our experiment employs a modified version of the classic Ramsey scheme, which will be elaborated in following sections. The steps of state preparation and readout, analogous to steps 1-2 and 4-5 of the Ramsey sequence, are achieved through laser-induced electronic transitions. The interaction region, akin to step 3, contains static electric and magnetic fields, where the signature of an eEDM appears as a change in the precession frequency upon reversing the relative direction of the electron's spin and the electric field.

Electrons are quantum objects. For each individual electron, the measurement of the precession phase, which is converted to the measurement of population for quantum states in step 5, could only have outcomes of 0 or 1 electrons in each state. To obtain a precise measurement of the precession phase, the experiment must be repeated many times to accumulate statistics. One can show that for a measurement of N electrons, the uncertainty (mean-square error) for the measurement outcome to reflect the actual phase in the quantum states, thus the value of eEDM, is [51, 54]:

$$\delta(d_e) = \frac{\hbar}{2E_{\text{eff}}\,\tau\sqrt{N}} \tag{1.4}$$

where $\hbar$ is the reduced Planck constant, and τ is the precession time. This uncertainty, known as the quantum projection noise or quantum shot noise, is the fundamental limit for the measurement of eEDM. In fact, Eq. 1.4 has a close relationship with the energy-time uncertainty principle. An ideal measurement scheme for eEDM maximizes the product $E_{\text{eff}}\tau\sqrt{N}$, given an adequate reduction of systematic errors.

1.2.3 Development of eEDM measurement experiments

The hypothesis that elementary particles might exhibit electric dipole moments was not proposed until 1950 [52]. The initial limits on the electron electric dipole moment (eEDM) were derived from a variety of experimental measurements including the Lamb shift ($2 \times 10^{-13}\,e \cdot$ cm) [55], electron g-factor (3×10^{-15} to $4 \times 10^{-16}\,e \cdot$ cm) [56, 57], and atomic scattering experiments

(1×10^{-15} to $2 \times 10^{-16}\, e \cdot \mathrm{cm}$) [58, 59].

Measuring electron EDMs in atoms resulted in dramatic improvements. The first atomic eEDM measurement was conducted by Sandars *et al.* [60]. This experiment significantly improved the sensitivity, reducing the previous bound by five orders of magnitude to $|d_e| < 2 \times 10^{-21}\, e \cdot \mathrm{cm}$. A principal systematic error in this setup was the motional magnetic field $\vec{B}_{\mathrm{mot}} = \frac{1}{c}\vec{E} \times \vec{v}$, which arises from the interaction between the atom's magnetic dipole moment and the electric field as the atom moves [61]. Ideally, if $\vec{E}$ is aligned perfectly with $\vec{B}$, $\vec{B}_{\mathrm{mot}}$ would be orthogonal to $\vec{B}$ and not influence the measurement. However, any misalignment could mimic an EDM signal, thus becoming a significant source of systematic error in many atomic beam eEDM experiments.

One strategy to mitigate this effect involves constructing an apparatus with two atomic beams propagating in opposite directions, allowing the sign of $\vec{B}_{\mathrm{mot}}$ to be reversed and its impact on the measurement to be nullified [62]. Another approach utilizes atoms with high polarizability, where the quadratic Stark shift significantly outweighs the Zeeman shift, as first demonstrated in a xenon EDM experiment by Player and Sandars [63]. These improvements in experimental design, particularly in Cs experiments throughout the 1960s, led to a further reduction in the eEDM limit by two additional orders of magnitude [64]. Significant advancements resumed in the 1990s with a highly sensitive experiment by Hunter *et al.*, utilizing a Cs atomic beam in a specialized cell designed to negate effects from motional magnetic fields [65]. This setup notably enhanced the previous limit by over an order of magnitude. The most notable systematic issue in these later experiments stemmed from leakage currents in the electric field plates.

The most precise atomic beam measurement of the eEDM to date were conducted by Commins *et al.* using thallium, achieving an effective electric field (E_{eff}) of approximately 70 MV/cm and applied field $E_{\mathrm{lab}} = 122$ kV/cm [66, 67, 68]. These experiments incorporated two sets of counter-propagating atomic beams, with the second set employing sodium atoms as a co-magnetometer.

This configuration allowed for a more effective differentiation between systematic effects and genuine EDM signals. The culmination of these efforts set the most stringent atomic limit on the electron EDM to date, $|d_e| < 1.6 \times 10^{-27}\, e \cdot \mathrm{cm}$. This Tl atom is specifically chosen for its large enhancement factor $R = -585$ (being the ratio of the effective E field and the applied lab field). Although this enhancement factor is quite large among all the atomic species, there is still a significant room for improvement, because the polarizations are based on the parity doublets of two electronic energy levels with $\Delta E \simeq 100\,\mathrm{THz}$ and as a result, the atoms are only polarized at $\sim 10^{-3}$! As we will see next, use of molecules, provides the potential of full polarizability to reach a much larger eEDM sensitivity.

In 1967, Sandars highlighted the potential of molecules as an advantageous system for electric dipole moment (EDM) searches due to their high polarizability [69]. Molecular EDM measurements, especially with heavy paramagnetic polar molecules, offer significantly enhanced sensitivity to the eEDM due to this significantly higher polarizability. In fact, fully-polarized molecules can be reached with effective electric fields of $10 - 100$ GV/cm, which is orders of magnitude higher than the achivable fields in atomic systems. This increase is attributed to the molecules' parity doublets, which have much smaller energy splittings compared to atoms.For instance, in ThO, the splitting is only several hundred kHz, approximately 10^3–10^4 times smaller than typical atomic systems [70]. However, molecular systems pose challenges in large-scale production and require complex state preparation and readout, often involving numerous lasers.

Table 1.1 lists various diatomic molecules used in electron EDM experiments, alongside their effective electric field values and the latest upper bounds on the eEDM.

The Imperial College YbF experiment in 2011 was the first to exceed the precision of atomic eEDM measurements, achieving an effective electric field (E_{eff}) of 14.5 GV/cm with a laboratory field of only 10 kV/cm, which significantly reduced the experimental challenge in generating high

molecule species	E_{eff} (GV/cm)	eEDM bound (e·cm)	reference
YbF	26	1.1×10^{-27}	[71, 72]
ThO	78	1.1×10^{-29}	[70, 48, 73]
HfF^{+}	23	4.1×10^{-30}	[43, 74]
ThF^{+}	35	-	[73, 75]
WC	36	-	[76]
PbO	25	1.7×10^{-26}	[77, 78]
BaF	6.5	-	[79, 80]

Table 1.1: **Diatomic molecules for eEDM searches.** Calculated effective electric field values and the most recent eEDM upper bounds are shown (if available).

electric fields, and suppressed the motional magnetic field effect [71]. The leading systematic effects for this experiment arose from imperfect electric field reversal, yet the experiment improved the eEDM upper bound to $|d_e| < 1.05 \times 10^{-27}\, e \cdot$ cm.

The ACME experiment has utilized the $H\ ^3\Delta_1$ state of ThO, achieving full polarization with an effective field of 78 GV/cm using only a 10 V/cm laboratory field. ThO's dual-state system allows for systematic error identification and rejection using in-built co-magnetometer states [70, 81, 82]. The first generation of the ACME experiment, completed in 2014, improved the eEDM limit by an order of magnitude, and the subsequent ACME II further refined this to $|d_e| < 1.1 \times 10^{-29}\, e \cdot$ cm.

The JILA eEDM experiment used trapped molecular ions for the first time, specifically in the metastable $^3\Delta_1$ state of HfF^{+}, achieving similar advantageous features as ThO [83]. With an increased coherence time and ability to measure an EDM with two co-magnetometer states simultaneously, the JILA results just published improved upon the ACME II bounds by a factor of about 2.5 [43].

New generations of all three of the molecular EDM experiments described above are underway. Significant progress has been made since the 2011 YbF experiment at Imperial College London, which now expects a demonstrated sensitivity of $1.5 \times 10^{-28}\, e \cdot$ cm for each day of data-taking. Recent advancements in transverse laser cooling on the YbF beam are expected to further enhance sensitivity by two orders of magnitude [84]. The ACME III experiment, discussed in this dissertation, has undergone various upgrades and is anticipated to surpass the sensitivity of ACME II by at least an order of magnitude in the coming years. The third generation of the JILA eEDM experiment is in preparation, utilizing the ground state of the ThF^+ molecule, which shares beneficial properties with HfF^+ but allows for even longer coherence times [85], and an innovative bucket-brigade ion trap to maximize the number of trapped ions being measured.

Looking further ahead, a promising avenue for eEDM measurements involves trapping molecules in an optical lattice, which combines extremely long coherence times with large numbers of particles. This method, experimentally feasible given recent successes in creating magneto-optical traps for molecules, a precursor for loading into an optical lattice [86, 87, 88], also finds application in highly precise atomic clocks [89]. It has been proposed specifically for YbF, with projections of $N = 10^6$ per shot, $\tau = 10$ s, and $E_{\text{eff}} = 17.5$ GV/cm, potentially achieving a statistical uncertainty of $2 \times 10^{-32}\, e \cdot \text{cm}$ [90]. Suitable polyatomic molecules, like YbOH, which exhibit similar E_{eff} to YbF but offer easier polarizability and internal co-magnetometer states, are also being considered for this technique [91].

A novel method recently proposed involves embedding EDM-sensitive polar molecules within a solid, transparent matrix of a rare gas such as argon [92, 93]. Utilizing ice-film nanocapacitors, this technique could provide extremely large numbers of molecules, with $N \approx 10^{13}$ for a 1 cm^3 sample. With a polar molecule like BaF and a coherence time of $\tau \approx 100$ ms (limited by the molecule density), a statistical uncertainty of $5\times10^{-34}\, e\cdot$cm could be achieved [94]. This approach is on the verge of reaching the Standard Model prediction of $|d_e| \approx 10^{-35}$ e·cm [36]. However, the maturity of this technique is still in its early stages, and substantial experimental work is required to produce such samples and assess their suitability for EDM experiments, particularly concerning potential systematic effects distinct from those observed in atomic or traditional molecular EDM studies.

The progress of electron EDM searches over the past 60 years is shown in Figure 1.4, the upper bounds on the electron EDM have been improved by several orders of magnitude, with the most recent experiments reaching an incredible $10^{-30}\ e \cdot \mathrm{cm}$ level. The progress in eEDM searches has been driven by the development of new techniques and the use of novel systems, such as diatomic molecules. Newer technologies are emerging, including solid-state systems, laser-cooled molecules, that is keeping the field at the forefront of precision measurements. The work in this disseration, as the third generation of the ACME experiment, is highlighted in the figure, and is expected to further improve the sensitivity by at least an order of magnitude in the near future.

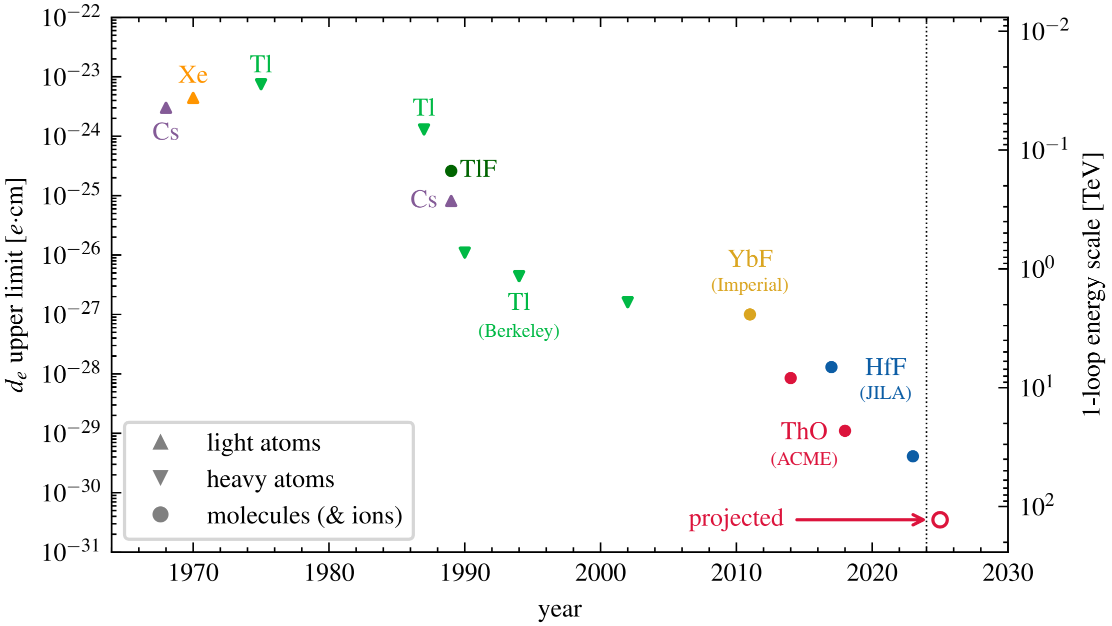

Figure 1.4: **Progress in electron EDM searches.** The search for the electron EDM has progressed significantly over the past 60 years, from the use of atomic Cesium [60, 62, 65], Xenon [63], and with heavier atoms like Thallium [64, 66, 67, 68]. The last decade see impressive improvements of over 3 orders of magnitude due to the use of diatomic molecules like YbF [71], ThO [70], and trapped molecular ions HfF^{+} [43]. The most recent experiments have reached an incredible $10^{-30}\ e \cdot \mathrm{cm}$ level. The ACME III experiment, discussed in this dissertation, is expected to further improve the sensitivity by at least an order of magnitude in the near future.

Since joining the ACME III collaboration in 2018, my initial contributions were focused on the new magnetic shielding system. We started using smaller, prototypical magnetic shields as a proof-of-principle study, with various tests in characterizing the mu-metal and optimizing the annealing procedures. I then started the development of the full-sized magnetic shield for ACME III, including the design, simulation, and construction of the shield, as well as the supporting experiment table, degaussing coils, electronic controls, and current supplies. Some re-modeling of the laboratory space was also involved, and a custom crane was built to facilitate the assembly of the magnetic shield. Additionally, I contributed to the enhancement of the magnetometer system, which monitors the magnetic field both inside and outside the shield. This involved recalibrating the system and adjusting its offsets. These efforts culminated in the creation of a robust magnetic shielding system, detailed in Chapter 4 of this thesis. Building upon this foundation, I engaged in the development of the main field coil in ACME III. My roles included participating in the design and simulation, leading the construction, and performing extensive characterization of the coil both within and outside the magnetic shield. These developments are thoroughly discussed in Chapter 5.

CHAPTER 2

OVERVIEW OF THE ACME EXPERIMENT

Since its inception in 2010 [95], the Advanced Cold Molecule Electron EDM measurement (ACME) strategy, which first proposes using a high-flux cold molecule beam of ThO, has significantly advanced the experimental limits on the electron electric dipole moment (eEDM). Over the past decade, ACME has improved the eEDM limits by two orders of magnitude. The first generation of the experiment concluded in 2014, achieving a new upper limit of $|d_e| < 8.7 \times 10^{-29}\, e \cdot \mathrm{cm}$ [70], which was more than an order of magnitude improvement over the previously best-known limit at that time [71].

Following this success, ACME II featured an improved state preparation through STImulated Raman Adiabatic Process (STIRAP) [96]. ACME II achieved $|d_e| < 1.1 \times 10^{-29}\, e \cdot \mathrm{cm}$ in 2018, which is another order of magnitude improvement compared to the ACME I result. ACME III makes the use of an approximately five times extended precession time that is possible because the lifetime of our science state H is much longer than what had been realized [97]. It also incorportates an electrostatic lens [98] that captures molecules more efficiently, and higher efficiency detectors [99]. The actively-shielded coil that produces the uniform magnetic field over a 1 m long beam path, and the required layers of mu-metal shielding are described in later chapters. ACME III is projected to measure the eEDM with a sensitivity that is 40 times better than that achieved by ACME II. The evolution of these results and the methodologies employed by the ACME experiments have been extensively documented [82, 100, 101]. In this section, I aim to provide a comprehensive overview of the ACME approach to eEDM measurement, highlighting the technological and methodological advancements that have facilitated these significant improvements.

2.1 The ThO molecule

ThO, as a diatomic molecule, exhibits electronic, vibrational, and rotational degrees of freedom. It falls under Hund's case (c) classification, where the orbital angular momentum $\mathbf{L}$ and the spin angular momentum $\mathbf{S}$ couple to form the total electronic angular momentum $\mathbf{J}_e = \mathbf{L}+\mathbf{S}$ [102, 103]. However, J_e itself is not a good quantum number due to these couplings. Instead, a more relevant quantum number is Ω, the projection of $\mathbf{J}_e$ onto the internuclear axis $\hat{n}$:

$$\Omega = \mathbf{J}_e \cdot \hat{n} = \Lambda + \Sigma, \tag{2.1}$$

Where Λ and Σ are the projections of $\mathbf{L}$ and $\mathbf{S}$ onto the internuclear axis, respectively.

Additionally, a diatomic molecule like ThO can rotate around its center of mass along its internuclear axis $\hat{n}$, which introduces rotational angular momentum $\mathbf{R}$. This $\mathbf{R}$ combines with $\Omega\hbar$ to give the total angular momentum $\mathbf{J} = \mathbf{R} + \Omega\hbar$, making J also a well-defined quantum number.

The electronic states of ThO are commonly described using the basis set $|Y, \nu, J, M, \Omega\rangle$, where Y represents the electronic state (expressed by alphabetical letters, e.g., X, C, H, Q), with X indicating the ground state. The vibrational quantum number ν indicates the vibrational state, although in this work nearly all states considered are in the lowest vibrational state ($\nu = 0$), and thus this number is often omitted in state descriptions. J and M denote the total angular momentum and its projection along the laboratory z-axis, respectively. The ACME electron EDM measurements are conducted in the lowest rotational level ($J = 1$) of the $H\ ^3\Delta_1$ state.

ThO, while being a Hund's case (c) molecule, can be described by a summation of Hund's case (a) states, with Λ and Σ as well-defined quantum numbers. The H electronic state predominantly consists of a 98.4% $^3\Delta_1$ state ($S = 1, |\Lambda| = 2, |\Omega| = 1$), which encompasses two valence electrons in σ and δ orbitals. The innovative use of this "Ω-doublets" to measure electron EDM, is a key factor for the evolution of molecular EDM measurements. The advantages of using the H state in EDM measurements are as follows:

- **Large effective electric field:** The σ electron spends considerable time near the heavy Th nucleus, thus experiencing a strong relativistic effect and producing an effective field, $E_{\text{eff}} = 78(2)$ GV/cm[1], which is one of the highest effective electric field known for molecules.
- **High polarizability with small Ω-doubling:** The H state features closely spaced pairs of opposite-parity levels, a characteristic of all $\Omega \neq 0$ states. The modest splitting between the $|H, J = 1, \Omega = \pm 1\rangle$ states, $\Delta_{|\Omega|} = 2\pi \times 360$ kHz, results from the Coriolis effect within the rotating molecule [102]. To exploit the large E_{eff}, we apply an electric field $\mathbf{E}$ that mixes the $M \neq 0$ opposite-parity states through the Stark interaction, $-\mathbf{D}_H \cdot \mathbf{E}$, where $D_H = 2\pi \times 1\,$MHz/(V $\cdot$ cm) is the dipole moment operator. The closely-spaced opposite-parity levels allow us to achieve a near-complete polarization of the states with electric field only on the order of 10 V/cm. Comparing with atoms, this would correspond to a enhancement factor on the order of 10^9, much larger than the 585 enhancement factor

---

[1] This number is obtained by averaging two recent calculations for the effective electric field of ThO H state: Skripnikov (2016) [48] gives 79.9 ± 3.2 GV/cm, and Denis and Fleig (2016) [49] gives 75.2 ± 2.2 GV/cm.

achieved in the Tl atom experiment [68]. In ACME, we typically use higher electric fields of 80 V/cm and 140 V/cm that is easily achievable in practice, to ensure complete mixing the states and achieve near-complete polarization ($P_E > 99\%$) [95].

- **Small magnetic moment:** Given that $\Lambda + \Sigma = \Omega$, in a ${}^3\Delta_1$ state, $\Lambda = -2\Sigma$. This anti-alignment of the spin angular momentum's projection with the orbital angular momentum's projection results in near-cancellation of the mangetic moment for the state, with $g_H \approx g_s\Sigma + g_L\Lambda = 0$. The actual magnetic moment turns out to be $g_H = 0.0088$ [104], resulted from the small anomalous magnetic moment of the electron, is only 0.88% of conventional electronic states that don't possess this cancellation. Thus, the H state is much less sensitive to magnetic fields.

- **Adequate radiative lifetime:** The H-state, being metastable, has a measured lifetime of $\tau_H = 4.2(5)$ ms [97], which allows the spin precession to be measured over a comparable timescale. In constrast, typical excited states in atoms and molecules have lifetimes on the order of nanoseconds.

- **Absence of nuclear spin:** Unlike molecules such as YbF or HfF$^+$, ThO lacks nuclear spin, eliminating the complexities associated with hyperfine structure.

- **High-yield production:** ThO can be generated in high quantities using cryogenic buffer gas beam technology, enabling a cold, dense beam ideal for precision measurements.

- **Well-known spectroscopy and accessible optical transitions:** Since the 1960s, ThO's spectroscopic properties are well-documented, and all necessary energy transitions for the ACME experiments are accessible using standard commercial diode lasers.

The combination of these properties makes ThO an exceptionally ideal candidate for precision measurements of the electron EDM. A brief skecth of the angular momentum in the H state is depicted in Figure 2.1.

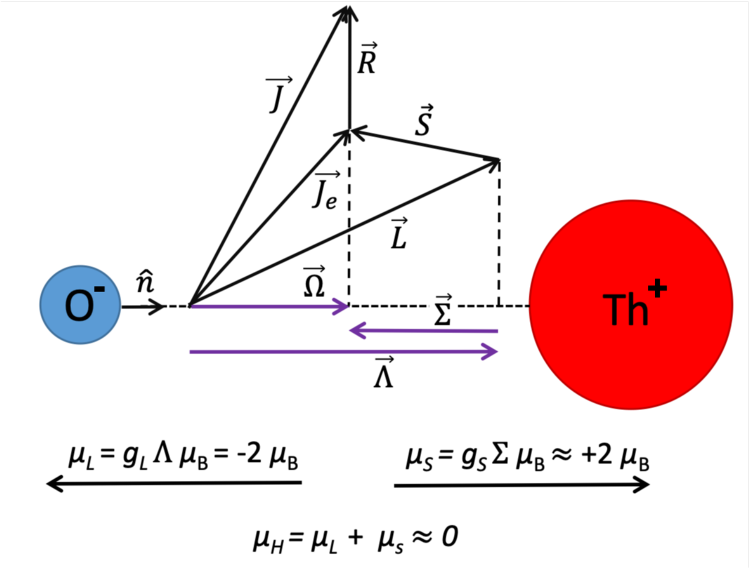

Figure 2.1: **Angular momentum in the H state of ThO.** The modest splitting between the $|H, J = 1, \Omega = \pm 1\rangle$ states makes the H state easy to polarize. Opposite orientation of $\mathbf{\Lambda}$ and Σ results in near-cancellation of the magnetic moment, making the H state ideal for eEDM measurements. Figure adapted from [105].

2.2 The spin precession measurement

The interaction between the effective electric field, $\mathcal{E}_{\text{eff}}$, and the electron EDM, $\mathbf{d}_e$, introduces an energy shift given by $U = -\mathbf{d}_e \cdot \mathcal{E}_{\text{eff}}$. The electron EDM vector $\mathbf{d}_e$ is defined as $d_e \mathbf{s}/(\hbar/2)$, where s represents the spin of the σ electron and $\hbar$ is the reduced Planck constant. The orientation of s aligns with the molecular spin state $\mathbf{S}$. The energy differences measured correspond to states with $M = \pm 1$, indicating $\mathbf{S}$ being aligned or antialigned with $\mathcal{E}_{\text{eff}}$, and includes a term proportional to U. This energy shift is depicted in Figure 2.2. Based on different orientations of the effective electric field, and the electron spin, these energy levels would be shifted towards different directions, in which the shift from the electron EDM interaction can be extracted.

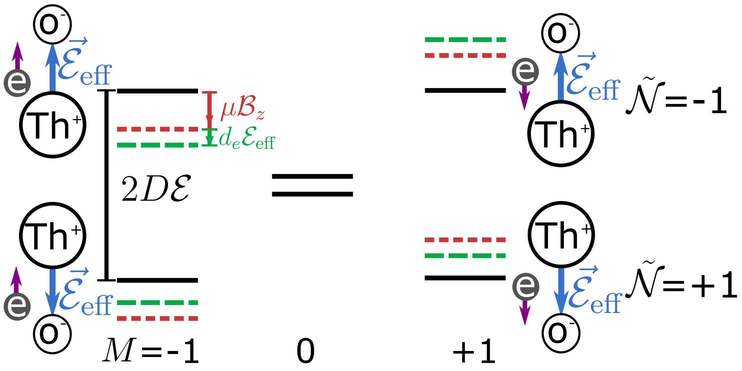

Figure 2.2: **Energy levels of the thorium monoxide H state.** The $|H, J = 1, |\Omega| = 1\rangle$ state manifold in external $\vec{\mathcal{E}}$ and $\vec{\mathcal{B}}$ fields, illustrated with sketches showing the orientation of the effective electric field $\vec{\mathcal{E}}_{\text{eff}}$ (blue arrows) and the spin of the electron $\vec{s}$ (purple arrows). The energy shifts $\mu\mathcal{B}_z$ (red) and $d_e\mathcal{E}_{\text{eff}}$ (green) due to the magnetic moment μ and the EDM d_e, respectively, are also depicted. The energy shifts from the electron EDM can be extracted by differentiating corresponding states.

In this setup, the internuclear axis $\hat{n}$ is aligned or antialigned with the laboratory electric field $\mathcal{E}$. The orientation of $\hat{n}$ determines the direction of the effective field $\mathbf{E}_{\text{eff}}$ acting on the electron dipole moment $\mathbf{d}_e$. States of opposite molecular orientation are defined by the quantum number $\tilde{\mathcal{N}} = \text{sgn}(\mathcal{E} \cdot \hat{n}) = \pm 1$. Reversing the direction of $\mathbf{E}_{\text{eff}}$ can be achieved either by flipping the laboratory field $\mathcal{E}$ or by switching the measurement state $\tilde{N} = \pm 1$, each method helping to eliminate a broad spectrum of systematic errors [68, 106, 107].

To further demonstrate the experiment schemes, we need to clarify about the coordinate systems. We define our coordinate system with $+\hat{z}$ aligned along $+\vec{\mathcal{E}}$, chosen as the positive direction pointing approximately north to south within the laboratory. The $+\hat{x}$ axis is aligned with the molecular beam direction, which travels roughly from west to east, while $+\hat{y}$ is then defined by forming a right-handed coordinate system with the existing two coordinates, and oriented approximately along the direction of gravity. Importantly, when reversing the electric field's direction, the laboratory coordinate system remains unchanged. The orientation of the electric field in either state can be expressed using $\tilde{\mathcal{E}} \equiv \mathrm{sgn}(\hat{z} \cdot \vec{\mathcal{E}}) = \pm 1$. Similarly, the magnetic field direction is alternated between two states, denoted as $\tilde{\mathcal{B}} \equiv \mathrm{sgn}(\hat{z} \cdot \vec{\mathcal{B}}) = \pm 1$. Therefore, the magnitudes of these fields are straightforwardly defined as $\mathcal{B}_0 = |\vec{\mathcal{B}}_z|$ and $\mathcal{E} = |\vec{\mathcal{E}}|$, allowing for precise control and repeatability of the experimental conditions.

An initial coherent superposition of $M = \pm 1$ states is prepared, setting the spin S along a predetermined direction in the xy-plane. The applied magnetic field, $\mathcal{B} = B_0 \hat{z}$, together with $\mathcal{E}_{\text{eff}}$, exert torques on the associated magnetic and electric dipole moments, causing S to precess in the xy plane. The angle of precession ϕ is captured as molecules evolve freely, and is quantified by:

$$\phi \approx \frac{-(\mu \tilde{\mathcal{B}} |\mathcal{B}_0| + \tilde{\mathcal{N}} \tilde{\mathcal{E}} d_e \mathcal{E}_{\text{eff}})\tau}{\hbar}, \tag{2.2}$$

Where $|\mathcal{B}_0| = |\mathcal{B} \cdot \hat{z}|$, $\tilde{\mathcal{B}} = \mathrm{sgn}(\mathcal{B} \cdot \hat{z})$, $\tilde{\mathcal{E}} = \mathrm{sgn}(\mathcal{E} \cdot \hat{z})$, and τ denotes the spin precession time. The parameters μ and $g_{\mathcal{N}}$ represent the Bohr magneton μ_{B} and the g-factor of the $|H, J = 1, \mathcal{N}\rangle$ state, respectively.

The sign of the EDM contribution to ϕ, indicated as $\tilde{\mathcal{N}}\tilde{\mathcal{E}}$, represents the torque's orientation induced by $\mathcal{E}_{\text{eff}}$ on s. The spin precession frequency, $\omega = \phi/\tau$, directly relates to the energy shift between the $M = \pm 1$ states, normalized by $\hbar$. The value of d_e is derived from the variation in ω that correlates with the orientation of $\mathcal{E}_{\text{eff}}$ in the laboratory frame, noted as $\omega^{\mathcal{N}\mathcal{E}}$, hence:

$$d_e = -\frac{\hbar \omega^{\mathcal{N}\mathcal{E}}}{\mathcal{E}_{\text{eff}}}. \tag{2.3}$$

Figure 2.3 shows the schematic of the main ACME III experiment setup. A cold and slow ThO beam is initially generated by ablation within a buffer gas beam source. Rotational cooling is then employed via optical pumping, resulting in the molecules with most of its population in the rotational ground state of X. Subsequently, Stimulated Raman Adiabatic Passage (STIRAP) is utilized to coherently transfer molecules to the $|Q, J = 2, M = 2, \Omega = -2\rangle$ state, which has a large Stark effect and are being electrostatically focused using a lens comprising cylindrical electrodes in a hexapole configuration, charged to approximately ± 14 kV.

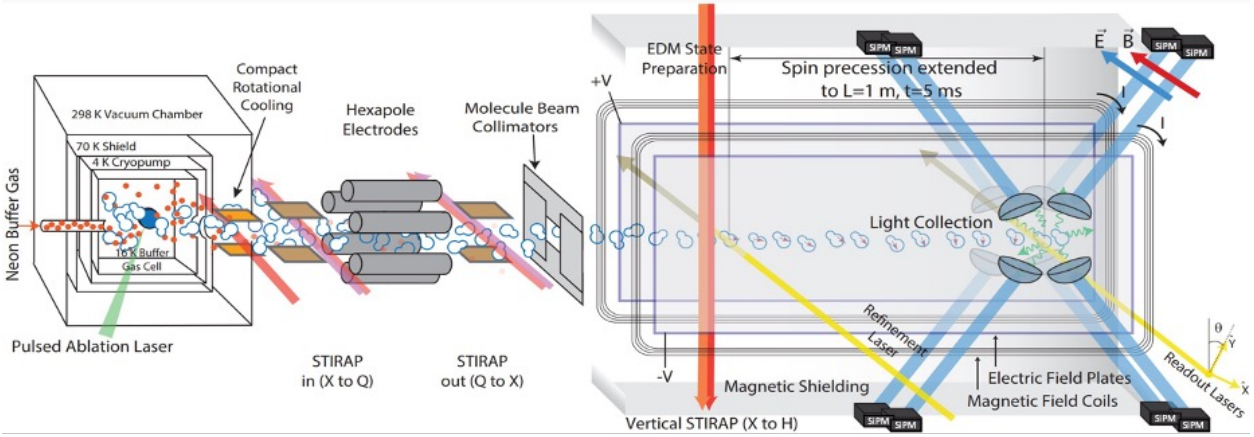

Figure 2.3: **Schematic of the ACME III experiment apparatus.** A cryogenic buffer gas beam source generates ThO molecules, being rotationally cooled to predominantly in the ground state, and collimated using a electrostatic focusing lens. These molecules are subsequently transferred to the EDM-sensitive $H^3\Delta_1$ state using STIRAP. Upon entering the interaction region, the molecules are prepared in an initial superposition of $|M = \pm 1\rangle$ states. They then undergo spin precession influenced by applied electric and magnetic fields. The phase accumulated during this precession is measured via laser-induced fluorescence. The fluoresence photons emitted at 512 nm are captured by a set of collection optics, passed through light pipes and detected with Silicon PhotoMultipliers (SiPM) outside of the main apparatus.

Following lensing, the STIRAP process is reversed to repopulate the ground state X. The beam then traverses fixed collimators, which prevent molecules from reaching the Indium Tin Oxide (ITO) coated field plates. Subsequently, the molecular beam enters a triply magnetically shielded region with rectangular μ-metal shields. Here, the electric ($\vec{E}$) and magnetic ($\vec{B}$) fields are applied using transparent field plates and field coils, respectively. Molecules are coherently transferred from the ground state $|X, J = 0\rangle$ to the $|H, J = 1, \tilde{N}\rangle$ state using $X - C - H$ STIRAP, with lasers oriented vertically through the experimental setup.

A refinement laser corrects any imperfections in the STIRAP-prepared phase by optically pumping out the orthogonal spin state. The molecules are allowed to precess freely in the applied fields over an increased path length of $L = 100$ cm until they encounter the readout laser.

We measure the phase ϕ from exciting the $H - I$ transition with laser light linearly polarized along the direction $\hat{\epsilon}$. The resulting fluorescence signal intensity, S_ϵ, varies according to the angle between $\hat{\epsilon}$ and the spin vector $\vec{S}$. To mitigate the effects of fluctuations in molecule numbers, we employ two alternating orthogonal linear polarizations, $\hat{\epsilon} = \hat{X}$ and $\hat{Y}$, and modulate $\hat{\epsilon}$ rapidly with a period of $5\,\mu$s, ensuring each molecule is addressed by both polarizations as it transits through the laser beam [108]. This is achieved by overlapping two laser beams with orthogonal polarizations $\hat{X}$ and $\hat{Y}$, and switching them on and off rapidly using acousto-optic modulators (AOMs). The pulses of $\hat{X}$ and $\hat{Y}$ each last $1.9\,\mu$s, separated by a $0.6\,\mu$s delay to minimize signal overlap due to the finite lifetime of the I state (115 ns) between successive pulses.

The fluorescence photons, emitted as the I state decays back to the ground state X (wavelength 512 nm), pass through transparent field plates and are collected by one of eight lenses positioned behind each plate. These lenses focus the photons into one of eight bent fused silica lightguides, each directing the light to one of eight silicon photomultipliers (SiPMs) located outside the magnetic shielding. These SiPMs are specifically optimized for detecting fluorescence at 512 nm, with a quantum efficiency of about 30%.

The signals from the SiPM are amplified and recorded by a 14-bit digitizer operating at 16 megasamples per second. This digital signal is then processed by a computer system, which also interfaces with another computer responsible for controlling slower switches (frequency < 10 Hz).

The asymmetry in the fluorescence signals, $\mathcal{A}$, is related to the precession phase as follows:

$$\mathcal{A} \equiv \frac{S_X - S_Y}{S_X + S_Y} = \mathcal{C} \cos\left(2(\phi - \theta)\right), \tag{2.4}$$

Where $\mathcal{C}$ is the contrast factor, representing the experimental sensitivity and is defined by:

$$\mathcal{C} \equiv -\frac{1}{2}\frac{\partial \mathcal{A}}{\partial \theta} \approx \frac{1}{2}\frac{\partial \mathcal{A}}{\partial \phi}, \tag{2.5}$$

And $\hat{X}$ is set at an angle θ relative to $\hat{x}$ in the xy plane (see Figure 2.3). This setup constitutes a projective measurement of the molecular alignment along both $\hat{X}$ and $\hat{Y}$. We optimize $|\mathcal{B}_z|$ and θ such that $\phi - \theta \approx \frac{\pi}{4}(2n+1)$ for integer n, enhancing the linearity and sensitivity to changes in ϕ. The contrast $\mathcal{C}$ is periodically calibrated by dithering θ between two close values, $\tilde{\theta} = \pm 1$, with a 0.2 rad difference, typically yielding $\mathcal{C} \approx 0.95$. This reduction from unity is attributed to several factors, including decay from C back to H, ellipticity in the laser polarization, and dispersion in forward velocity.

Finally, the measured phase, Φ, is extracted by normalizing the measured asymmetry by the contrast:

$$\Phi = \frac{\mathcal{A}}{2\mathcal{C}} + \frac{\pi}{4}(2n+1). \tag{2.6}$$

While ideally, Φ should equal the true phase ϕ, Chapter 3 discusses how experimental imperfections may lead to deviations.

As a summary, Figure 2.4 displays all the electronic states utilized in the ACME III experiments along with their commonly used transitions.

2.2.1 Ablation and buffer-gas beam source

The ACME experiment initiates with the ablation production of a buffer gas cooled beam, detailed further in [109, 110, 111]. A cylindrical pressed powder ceramic target, primarily composed of

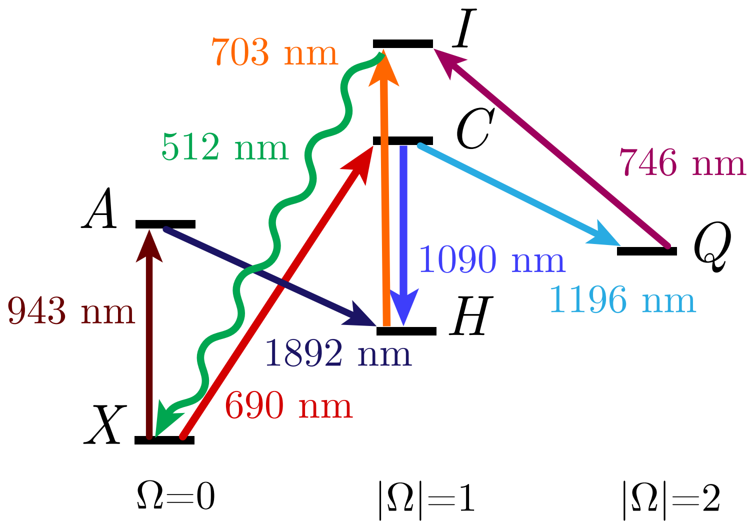

Figure 2.4: **Electronic states of ThO relevant to the ACME experiments.**States are grouped by Ω, the total electronic angular momentum projected on the internuclear axis. Transitions used in the experiments are also shown.

ThO_2 and with a diameter of approximately 0.6 inches, is positioned inside a copper cell cooled to about 16 K. In ACME II, cooling was achieved using a single pulse tube refrigerator, while ACME III employs a pair of pulse tube refrigerators in a configuration that provides enhanced cooling power, tested over multiple years in the past. The target is ablated by a focused Nd:YAG laser pulse, characterized by an energy of approximately 50 mJ, a pulse duration of about 15 ns, and a 50 Hz repetition rate. The ablation process produces ThO molecules which are entrained in a Neon gas flow of 40 sccm, thermalized within the cell, and then exit through a circular aperture, creating a beam consisting of Neon, ThO, and various other neutral and ionic species.

To eliminate ions from the beam, an ’ion sweeper’ consisting of two charged plates producing an electric field of 250 V/cm is used, effectively deflecting any ions. The beam at this point is highly divergent, with an angular full-width-half-maximum (FWHM) of approximately 45° [112], and is collimated by a skimmer aperture with a 6 mm opening. This divergence represents a significant source of loss in the ACME experiment, motivating the use of an electrostatic lens described in Section 2.2.3 and the reduction of the distance between the cell and the lens. After the skimmer, the beam's forward velocity is approximately 200 m/s, though this value has been observed to vary by about 10% from pulse to pulse. This process generates roughly 10×10^{10} molecules per pulse, with a rotational temperature of about 4K, implying that approximately 90% of molecules are in the $J = 0 \sim 3$ rotational states.

With a new ablation target, the beam source can typically produce molecules continuously for 10-20 minutes before the target spot is exhausted and the signal falls below acceptable levels. At this point, data collection is paused while the ablation laser is redirected to a different spot on the target by adjusting a motorized mirror. After about 1-2 weeks of constant operation (18 hr/day), the target must be replaced. The ACME beam source, originally developed for ACME I and essentially unchanged in its basic physics for ACME II and III, now includes a load-locking system developed in ACME III for rapid target changes. During the final data collection of ACME II, target changes were typically performed every 2-3 weeks, The target change process, taking approximately 4 hours, was followed by about 12 hours of cooling to return to operating temperature, which is a significant time-consuming procedure.

Thus, a load-lock apparatus was developed in ACME III to allow daily target changes without the need to warm up and cool down the beam box each time, significantly reducing the amount of radiation work required. This effort, led by Zhen Han, has been developed and experimentally demonstrated. The targets, mounted onto a copper block, are inserted via a rod into a load lock chamber at the top of the beam box, then screwed onto a rotatable vertical translation rod. Once attached, the chamber is sealed, and the rod lowers the target to the correct height for transfer to a horizontal rod connected to a linear bellows and a ferrofluid feedthrough, facilitating rotation. This rod is threaded but also features a ball driver end used to secure and then detach the target block within the cell. Once the experiment concludes for the day, target changes are performed in about

1 hour, aligning with daily deicing routines and potentially increasing the overall duty cycle of the experiment.

2.2.2 Rotational cooling

The molecules exiting the buffer gas cell, maintained at a temperature of approximately 4K, predominantly populate the lowest four rotational levels of the electronic and vibrational ground state, denoted as $|X, J = 0, 1, 2, 3\rangle$. However, the state preparation is optimized to transfer population from the $|X, J = 0\rangle$ state to the H state exclusively. To enhance the signal, optical pumping shifts the population from the $|X, J = 1\rangle$ and $|X, J = 2\rangle$ states into the $|X, J = 0\rangle$ state, achieving approximately a 2.5 times signal gain [81]. Although additional gains could potentially be achieved by also pumping out the $|X, J = 3\rangle$ state, the required additional laser and the minimal gain offset deter this practice in the operational setting.

Briefly speaking, the optical pumping targeted the X-C transition and was executed in two distinct stages, schematically illustrated in Figure 2.5. Here, we introduce the notation $|X, J = 0^+\rangle$ for states, where the superscript denotes the parity, essential for understanding the employed pumping scheme. The first stage targets the 690 nm transition $|X, J = 2^+\rangle \rightarrow |C, J = 1^-\rangle$, where the $|C, J = 1^-\rangle$ state can decay either back to $|X, J = 2^+\rangle$ or to $|X, J = 0^+\rangle$. This stage involves multiple passes (5-7) of the laser with alternating polarization to address all M sub-levels and recapture molecules that decay back to $|X, J = 2^+\rangle$. Parity selection rules preclude the use of this scheme for the $|X, J = 1^-\rangle \rightarrow |C, J = 1^-\rangle$ transition. Instead, a weak electric field of approximately 100 V/cm is applied to mix the parity states $|C, J = 1^\pm\rangle$. A similar multipass laser setup with alternating polarization then drives the transition $|X, J = 1^-\rangle \rightarrow |C, J = 1^\pm\rangle$, facilitating decay to the desired $|X, J = 0^+\rangle$ state. Detailed information can be found in [100].

One major concern of this well-developed rotational cooling scheme used in ACME I and II is that the steps were performed sequentially, requiring separate beamline sections, one with field plates and another without them, along with separate optical setups, occupying approximately 20 cm in the ACME II beamline. The molecular beam prior to the electrostaticlens exhibits significant divergence, thus, any distance between the beam source and the focusing lens aperture results in substantial signal loss. This constraint necessitates the modification to a single spatial stage design. This is done innovatively in ACME III by rapidly switching the driving laser between the two transitions, synchronized with an alternating electric field. This scheme is depicted in Figure 2.5. To optimize space, the two lasers are coupled into a single shared fiber with orthogonal linear polarizations by first combining the beams on a polarizing beam splitter (PBS). The combined beams pass through a polarization electro-optic modulator (EOM) followed by another PBS. The state of the polarization EOM is switched, allowing selection of which pump laser passes through the second PBS. A more detailed description is in [98, 113].

2.2.3 Electrostatic lens

The divergence of the molecule beam significantly limit the number of molecules that can be detected in the spin precession measurement. In ACME II, only 4% of the produced molecules propagate through the interaction volume, and one would expect this number to be even lower in ACME III due to the increased length of spin precession. To address this issue, a method to collimate the molecule beam was developed.

While initial efforts to develop an electrostatic lens utilizing the ground state X result in obstacles like unintended X-ray production [114], new initiatives led by Xing Wu explored the potential of the ThO $Q\ ^3\Delta_2$ state. This state proved advantageous for use with an electrostatic lens for several reasons, as detailed in a recent study [115]:

1. The $|Q, J = 2, M = 2, \Omega = -2\rangle$ state exhibits a large linear Stark shift with a dipole

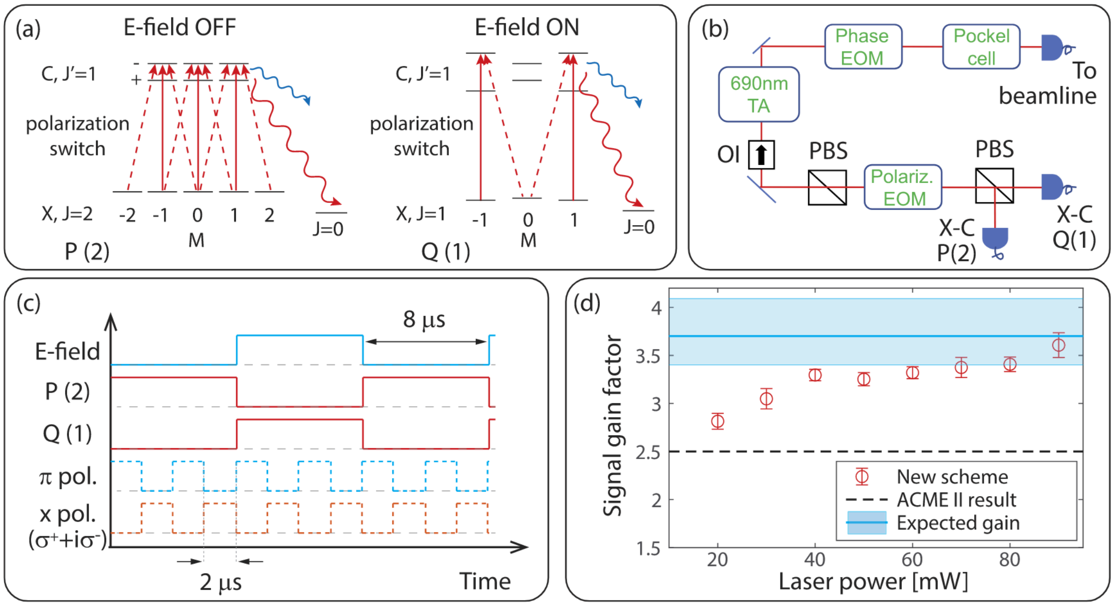

Figure 2.5: **New rotational cooling scheme in ACME III.** (a) The energy levels and laser transitions involved in this rotational cooling scheme. (b) The schematic of the optical setup for combining the two lasers. (c) Timing diagram of the switches used. (d) The demonstrated signal gain for incorporating this compact rotational cooling scheme. Figure adapted from [98].

moment $d_Q = 1.60(2)\, ea_0$, nearly an order of magnitude greater than the $|X, J = 2, M = 0, \Omega = 0\rangle$ state used in earlier lens designs [98]. This significant shift enables greater trap depths with lower applied fields, enhancing lens effectiveness and reducing X-ray risks.

2. The radiative lifetime of the Q state is sufficiently long, with measurements showing $\tau_Q > 62$ ms, ensuring no measurable decay during transit through the 53 cm lens [115].

3. The dipole moment for the $Q - C$ transition is large enough ($d_{Q-C} = 0.397(47)\, ea_0$) to facilitate efficient STIRAP transitions between the X, C, and Q states, achieving transfer efficiencies of 90% for one stage and 80% for two stages [115].

Additionally, the Q state's substantial molecule-frame magnetic dipole moment $\mu_Q = 2.07(11)\mu_B$ also makes it suitable for use in a magnetostatic lens using a Halbach array [115, 100]. However, for ACME III, an electrostatic method was favored due to the tunability offered by electrode voltage adjustments, a feature not available with permanent magnet-based systems.

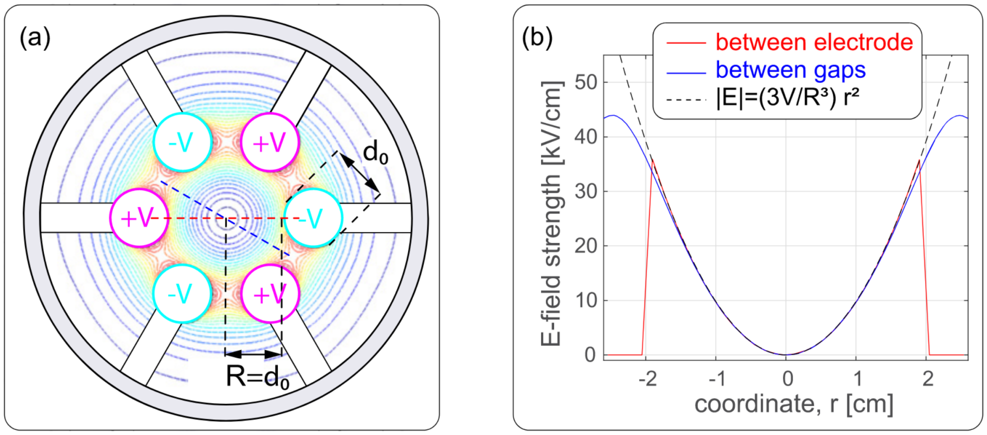

Figure 2.6: **Electrostatic lens schematic and the created potential.** (a) A schematic of the electrostatic lens showing the voltage distributions.The lens uses cylindircal electrodes with $d_0 \approx 2\,\text{cm}$. (b)The corresponding electric potential observed on the blue and red cut lines shown in (a). Potentials show a minimal deviation from a revolving quadratic potential. Figure adapted from [98].

Based on these findings and extensive simulation work, an electrostatic lens apparatus was designed, constructed, and tested [98]. This development was spearheaded by Xing Wu, with substantial assistance from Peiran Hu and Zhen Han. As shown in Figure 2.6, the lens consists of six 53 cm long cylindrical electrodes, each 19 mm in diameter, arranged radially at a distance of 19 mm from the center. A DC voltage $\pm V$ is applied to the electrodes in alternating polarity to generate the desired electric field configuration, described by:

$$\mathcal{E}(r) = \left(\frac{3V}{R^3}\right) r^2 \tag{2.7}$$

Where r is the radial position and R is the distance from the lens center to an electrode surface. The field on the radial direction is close to a revolving quadratic distribution over r. Thus, the resulting linear Stark shift induces a restoring force, given by:

$$\mathbf{F}(r) = -\frac{d}{dr}(-\mathcal{D}\mathcal{E}(r))\hat{r} = \mathcal{D}\left(\frac{6V}{R^3}\right) r\hat{r} \tag{2.8}$$

Where $\mathcal{D} = d_Q \frac{\Omega M}{J(J+1)}$ is the transition diple moment in the Q state. While this force configuration does not inherently provide stability for states with $D \geq 0$, the specific choice of the lensing state $|Q, J = 2, M = 2, \Omega = -2\rangle$ ensures that the force is indeed restoring. The lens acts analogously to a thick optical lens, focusing molecules near the detection region as depicted in Figure 2.7 [115]. The lens design was optimized via numerical simulations to maximize molecular flux in the detection region, with the optimal configuration achieved with $V = 14$ kV applied voltage. The design and assembly were validated using both the ACME II and ACME III setup, confirming simulation predictions [98]. Figure 2.8 shows the comparison of the detected signal with and without the lens, demonstrated on the ACME III setup.

The integration of the lens into ACME III also involved expanding the separation of the elec-

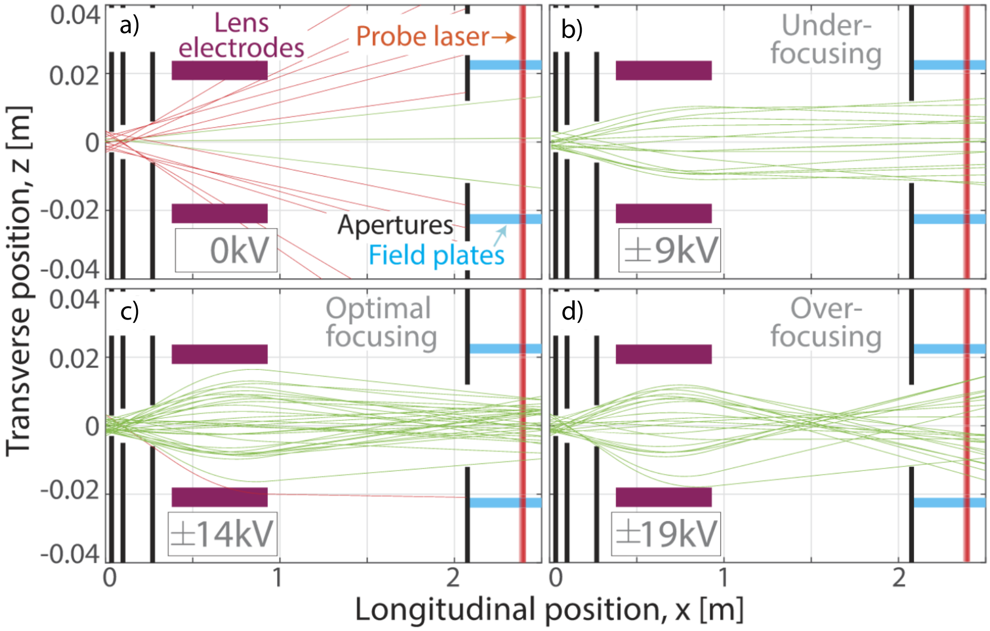

Figure 2.7: **Simulation of the electrostatic lens focusing on ThO beams.** trajectories of the ThO molecules are traced for the cases where (a) no voltage is applied on the lens electrode, and (b), (c), (d) the applied voltage increases. The focusing result with most molecules come through the readout laser (shown in red vertical lines) is achieved at $V = 14\,\text{kV}$. Figure adapted from [98].

tric field plates in the spin-precession volume from 4.5 cm to 6 cm to prevent collisions with the ITO-coated field plates and potential build-up of patch potentials. A fixed collimator was installed between the lens and the field plates to further reduce collision risks. The lens is housed in a dedicated vacuum chamber, with segments for performing STIRAP at either end, in order to transfer $X - C - Q$ for the molecules coming from the beam source, and transferring back as $Q - C - X$ after the beam was collimated. On the upstream end it attaches to the rotational cooling system, while on the downstream end it attaches to the nipple connected to the interaction region that passes through the magnetic shields. Geiger counters have been installed near the lens chamber, but no X-ray production has been observed during operation.

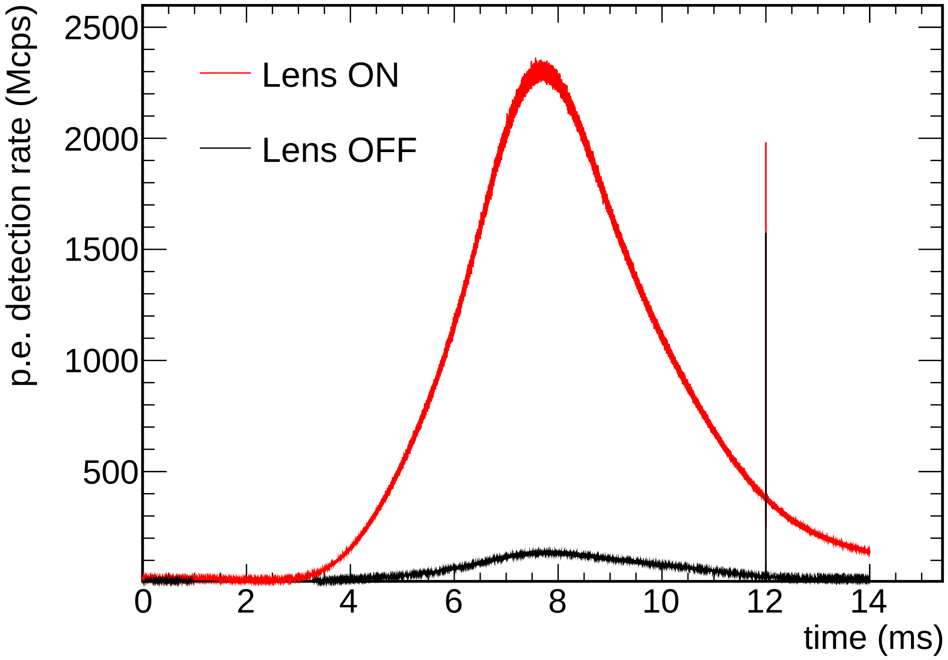

Figure 2.8: **Comparison of the detected signal with and without the lens.** Figure shown here are preliminary result demonstrated on the ACME III setup. Image courtesy of Ayami Hiramoto.

The introduction of the electrostatic focusing lens in the ACME III experiment facilitated the optimization of precession time, leveraging the lifetime of the H state to maximize measurement sensitivity. Following the completion of ACME II, Daniel Ang and Cole Meisenhelder conducted a rigorous study to measure the lifetime of the H state, accurately determining $\tau_H = 4.2 \pm 0.5$ ms [97]. This value was significantly larger than the previously assumed 1 ms, suggesting a potential increase in sensitivity by extending the spin-precession volume.

To achieve the largest possible increase in sensitivity, it was crucial to consider three factors influencing the precession time's contribution to $\delta(d_e)$. First, as described by Eq. 1.4, converting measured phase to frequency implies that the frequency uncertainty scales inversely with τ. The relationship between the photon count rate $\dot{N}$ and τ is less intuitive; $\dot{N}$ is influenced by the exponential decay of the population in the H state, modeled as $\dot{N} \propto e^{-\tau/\tau_H}$. Another contribution to $\dot{N}$, more complex to quantify analytically, arises from non-ideal collimation of the molecular beam, which naturally diverges en route to and within the precession region. Disregarding the minor focusing effects of the electrostatic lens and any modifications to detection optics in ACME III, this contribution introduces a scaling term $\dot{N} \propto 1/(l+\tau)^2$, where l is the distance from the beam source to the refinement laser. This leads to:

$$\delta d_e(\tau) \propto \left(\frac{1}{\tau}\right)\left(\frac{1}{\sqrt{e^{-\tau/\tau_H}}}\right)(l+\tau) \tag{2.9}$$

The effect of electrostatic lens, which alters the sensitivity of eEDM measurement from the beam divergence, is taken into account through numerical simulations. The results are illustrated in Figure 2.9. Based on the new measurement on the H state lifetime [97], the sensitivity gain is calculated for three different beam divergence scenarios: no lens collimation, the optimal collimation shown in Figure 2.7, and an unrealistic case that the beam is perfectly collimated. Shaded region represent uncertainties, which primarily originate from the uncertainty of τ_H measurement. As a consequence, the ACME III experiment choose to operate with a precession length of 100 cm, which is expected to provide a sensitivity gain of 2.6 compared to ACME II.

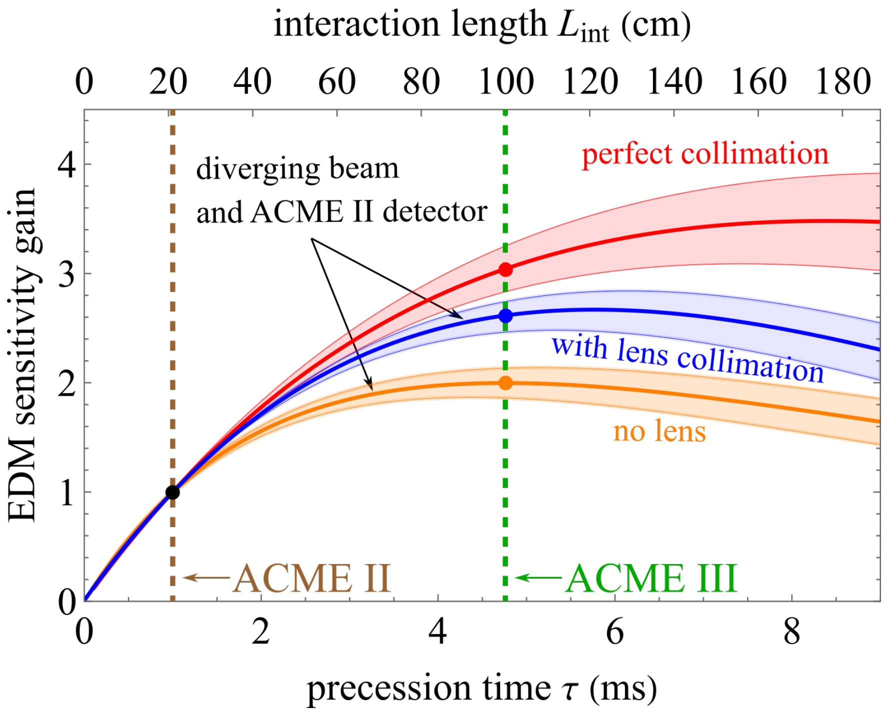

Figure 2.9: **EDM sensitivity gain as a function of precession time.** Based on the new measurement on the H state lifetime, the sensitivity gain is calculated for three different beam divergence scenarios: no lens collimation, the optimal collimation shown in Figure 2.7, and an unrealistic case that the beam is perfectly collimated. Shaded region represent uncertainties, which primarily originate from the uncertainty of τ_H measurement. The dashed lines indicate the precession time used for ACME II and the chosen precession time for ACME III. Figure adapted from [97]

.

2.2.4 State preparation

After transferring the population of the molecular beam to the $|X, J = 0\rangle$ state, achieved via Q-C-X STIRAP in ACME III, the molecules proceed to a magnetically shielded volume, referred to as the spin-precession volume. As mentioned in previous sections, the collimated beam has a width of ± 2.1 cm (3σ), that evolves freely in a length of $L = 100$ cm, thus the spin-precession volume is a 1 m long cylindrical space with 4.2 cm diameter. In this volume, both electric and magnetic fields are applied to induce precession. Upon entry into this region, the molecular beam undergoes further collimation through square fixed collimators ($25\,\mathrm{mm} \times 25\,\mathrm{mm}$), designed to prevent any beam interactions with the electric field plates.

State preparation is executed in two phases. The initial phase involves STIRAP, which coherently transferring population from the $|X, J = 0\rangle$ state to the desired spin state $|\psi(t = 0), \tilde{N}\rangle$ [82]. This STIRAP process utilizes the $|C, J = 1, M = 0\rangle$ state as an intermediate, with the pump laser tuned to the 690 nm $X - C$ transition and the Stokes laser to the 1090 nm $C - H$ transition. Lasers are vertically aligned through the experiment, with a slight overlap to ensure proper temporal interaction with the molecular beam. Due to the $\Delta M = \pm 1$ transition requirement, the pump laser employs z-polarization ($\Delta M = 0$), while the Stokes laser uses x-polarization ($\Delta M = \pm 1$). Further details on this STIRAP process can be found in references [82, 101]. Compared with the traditional optical pumping method, STIRAP increases the state transfer efficiency by a factor of 12, thus has been incorporated since ACME II experiment, as a major upgrade from ACME I [81].

While STIRAP efficiently prepares the desired state $|\psi(t = 0), \tilde{N}\rangle$, imperfections may produce a non-ideal initial spin state, potentially leading to systematic errors discussed in the following chapters. To mitigate these, a refinement step using a "cleanup laser" tuned to the 703 nm transition between $|H, J = 1, \tilde{N}\rangle$ and $|I, J = 1, M = 0^+\rangle$ is implemented. This state has a short lifetime of approximately 115 ns [116, 117]. The cleanup laser, sent through the field plates along the z-axis and polarized along the x-axis, optically pumps out the bright state orthogonal to the desired dark state $|\psi(t = 0), \tilde{N}\rangle$. This setup not only provides a more effective suppression of phase misalignment errors compared to the C state used in ACME I [82, 70] but also simplifies the overall system by using the same laser system for state readout described in Section 2.2.6. Both the STIRAP and refinement lasers allow for the selection and rapid switching between $\tilde{N}$ states, a feature crucial for the measurement of spin-precession phase.

2.2.5 Spin precession in controlled electric and magnetic fields

As the molecular beam progresses towards the state preparation lasers, it starts the spin precession, which extends from just before the cleanup laser to beyond the readout lasers. In this region, the molecules encounter uniform electric ($\vec{E}$) and magnetic ($\vec{B}$) fields, which are aligned such that the z-axis is defined by these field vectors. The electric field is generated by a pair of glass field plates, uniformly spaced and coated with a thin layer of optically transparent and conductive Indium Tin Oxide (ITO). The separation between these plates is 6 cm for ACME III to accommodate improved optical access that comes vertically between these plates. These transparent field plates allow laser beams to be directed along the z-axis and also enable the detection of molecular fluorescence through the plates themselves. The development of the ACME III electric field system was led by Peiran Hu.

The magnetic field within the interaction region is produced by an external coil that is designed to ensure a highly uniform magnetic field. This coil is part of a setup that also includes auxiliary coils aligned along the x and y axes to apply additional fields and gradients. Shielding from external magnetic influences, such as the Earth's magnetic field and stray fields from the surrounding environment, is also important. Precise control of magnetic field in the spin-precession volume is led by me, alongside with significant contributions from Bingjie Hao, Daniel Lascar, Xing Fan, Cole Meisenhelder, Daniel Ang, and extensive support from the whole ACME collaboration. The detailed discussion of the magnetic shielding system can be found in Chapter 4, and the magnetic field coils are described in Chapter 5.

2.2.6 State readout and detection

In the readout region of the ACME experiments, molecules are optically pumped from the $|H, J = 1, \tilde{N}\rangle$ state to the $|I, J = 1, M = 0^{+}\rangle$ state using a 703 nm laser, similar to the refinement process in the state preparation. The short-lived I state decays to the ground state X, emitting a 512 nm photon. To project out the phase ϕ, the polarization is rapidly alternated between two orthogonal linear polarizations, $\hat{X}$ and $\hat{Y}$. This switching occurs at 200 kHz, ensuring that each molecule experiences both polarizations without any overlap in time, given the molecular beam's transit time of approximately 10 μs.

The emitted 512 nm fluorescence light passes through the transparent field plates and is captured by eight pairs of lens doublets, as seen in the experiment schematics (Figure 2.3). These doublets focus the light into fused quartz light pipes, which convey the light via total internal reflection out of the vacuum chamber and magnetic shields to the detectors that is outside of the magnetic shields. In ACME II, these detectors were photomultiplier tubes (PMTs). However, to enhance collection efficiency, ACME III has transitioned to using Silicon Photomultipliers (SiPMs).

ACME II utilized Hamamatsu R7600U-300 PMTs, which had a quantum efficiency of 25% at 512 nm [118]. Although this was an improvement over previous PMTs, the potential for further enhancement led to the consideration of SiPMs. SiPMs offer nearly 50% quantum efficiency at 512 nm but introduce challenges such as higher dark count rates and significant optical crosstalk and afterpulsing, which can result in excess noise [119, 120]. For ACME III, collaborators from Okayama University led the successful development of high-efficiency SiPM detectors [121, 122, 99].

SiPM detectors consist of a chip array of avalanche photodiode sensor pixels operated in Geiger mode, with each pixel connected in parallel. The ACME III SiPM system uses the Hamamatsu S13361-6075NE-04, a 4×4 array of SiPMs within a $25\text{mm} \times 25\text{mm}$ package, where each sensor measures $4\text{mm} \times 4\text{mm}$. Given the significantly larger effective area compared to the ACME II PMTs, the diameter of the fused quartz light pipes has been increased from 16 mm to 20 mm. The operational challenges, such as the high dark count rate and susceptibility to background noise from scattered 703 nm laser light, are mitigated by cooling the SiPMs to -20°C, which reduces the dark count rate to about 3% of the room temperature rate [121].

A brief schematic of the SiPM module and the improved detection efficiency is shown in Figure 2.10. A key strategy to minimize optical crosstalk involves placing absorptive bandpass filters directly on the SiPMs and incorporating additional filters in the optical path. This setup has effectively reduced the optical crosstalk to 4.3% and has brought the excess noise factor down to approximately 1.07, an improvement over the ACME II system [99].

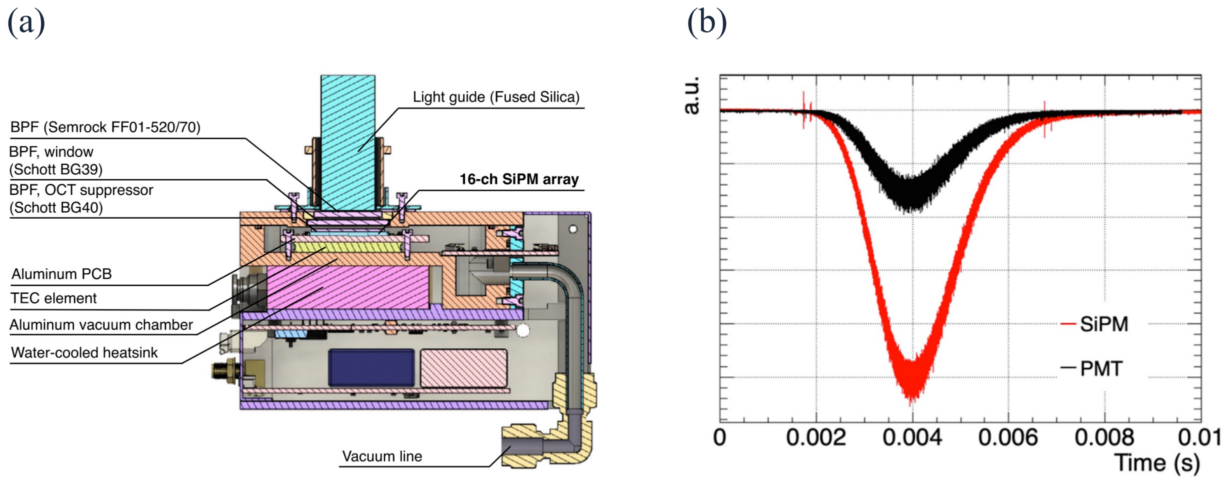

Figure 2.10: **The SiPM module and the demonstrated efficiency improvement in ACME III.** (a) A schematic of the SiPM module. (b) The detection efficiency of the SiPMs compared with PMTs. A factor of 2.3 improvement was demonstrated for 512 nm fluorescence. Figure adapted from [121].

In light of the increased field plate separation to 6 cm and the replacement of PMTs with larger SiPMs, the collection optics for ACME III has also been redesigned. Led by Daniel Ang, the optimization process utilized LightTools simulations, similar to those employed for the ACME II design. The new collection optics consist of eight pairs of larger custom-built lens doublets, designed to accommodate the increased separation and larger sensor size. These optics are expected to capture approximately 30% of the fluorescence, which is a factor of about 1.7 enhancement of the signal collection efficiency compared with ACME II [123].

2.3 Summary

The measurement protocol for detecting the electron EDM, alongside the apparatus detailed in this chapter, indicates an expected fluorescence signal count rate of approximately 7.3×10^6 photons per pulse. This expectation is based on empirical data from the ACME II experiments and the observed signal enhancements attributed to each apparatus upgrade implemented in ACME III. With parameters set at $E_{\text{eff}} = 78\,$GV/cm and $\tau = 5\,$ms, and a total data collection duration of approximately 350 hours mirroring the protocol established in ACME II the sensitivity is projected to improve to $3.5 \times 10^{-31}\, e \cdot$ cm for ACME III. Preliminary results from the newly assembled ACME III apparatus have indeed confirmed the anticipated signal count of 7.3×10^6 photons per pulse, thereby validating the apparatus's potential. Consequently, the primary challenge remaining in achieving the projected sensitivity of ACME III lies in controlling both the statistical and systematic uncertainties, beyond the intrinsic quantum limits outlined by Eq. 1.4.

CHAPTER 3

STATISTICAL AND SYSTEMATIC UNCERTAINTIES

This chapter outlines the data analysis protocol utilized in ACME II, as well as the studies of statistical and systematic uncertainties. The ACME III measurement will follow similar principles of ACME II [81], while an entirely new apparatus has been implemented to increase the sensitivity by about 40 times. Thus, it is imperative to understand the data analysis and error handling protocols in ACME II [81]. This understanding will guide similar approaches in ACME III, albeit with the challenges from significantly enhanced sensitivity that demands stricter suppression of statistical and systematic errors. More detail on the ACME data analysis can be found in the PhD thesis [101, 100, 124]. Particular emphasis is placed on the noise and systematic effects related to magnetic field imperfections in the spin-precession volume, which directly pertain to my PhD work and are detailed further in Sections 3.2.2 and 3.3.1.

3.1 Data analysis protocols in ACME

3.1.1 Review of the ACME II data

In the ACME experiment, the precession phase Φ is determined by probing the $H - I$ transition with linearly polarized light and observing the resulting fluorescence. The electron EDM is subsequently extracted from the asymmetry between the population transitions induced by two orthogonal laser polarizations, as described by Eq. 2.4.

To mitigate fluctuations in molecule number, we employ a rapid alternation technique for the readout laser polarization. This method ensures that each molecule is reliably projected onto one of two orthogonal spin alignment directions, denoted as $\hat{X}$ and $\hat{Y}$, during its approximately 10 μs transit through the laser beam. The probability of projection is determined by the relative angle between the the molecule's spin and the laser polarization. This experimental setup involves two overlapping laser beams with orthogonal $\hat{X}$ and $\hat{Y}$ polarizations, which are rapidly switched on and off at a frequency of 200 kHz using Acousto-Optic Modulators (AOMs). Each polarization pulse ($\hat{X}$ and $\hat{Y}$) has a duration of 1.9 μs, with a 0.6 μs interpulse delay to minimize signal overlap between successive pulses. This delay is necessary due to the finite lifetime (115 ns) of the I state (see Figure 3.1 (a)).

This precise timing structure ensures that approximately one fluorescence photon is emitted by each molecule, effectively projecting the molecule's spin-aligned state onto the two orthogonal spin states corresponding to the $\hat{X}$ and $\hat{Y}$ polarizations of the linearly polarized probe laser beam.

The molecules transitioned to the I state by the alternating laser polarization results in a fluorescence as it decays back to the ground state, detected by the SiPM as a time-varying signal $S(t)$ (Figure 3.1 (a)). The temporal evolution of this signal is governed by the molecular dynamics, which are influenced by the properties of the readout molecular states (H and I) and the spatial and temporal profile of the laser beam intensity. Initially, there is a rapid increase in fluorescence as molecules in the laser beam are excited when $\Omega_r t \ll 1$, where $\Omega_r \sim 2\pi \times 3$ MHz is the Rabi frequency of the $H - I$ readout transition, the fluorescence magnitude increases as $S(t) \propto \Omega_r^2 t^2$. As $\Omega_r t \geq 1$, the population becomes evenly distributed between the H and I states, causing $S(t)$ to decay exponentially with a time constant of $2\tau_I \approx 230$ ns, where $\tau_I \approx 115$ ns is the lifetime of the I state. Concurrently, new molecules continue to enter the laser beam, resulting in the exponential decay approaching a constant fluorescence rate in the steady state. Upon laser deactivation, the signal decays exponentially to zero with a time constant of τ_I.

To analyze this signal, we integrate $F(t)$ over time intervals associated with pairs of orthogonally polarized ($\hat{X}$ and $\hat{Y}$) laser pulses to compute F_X and F_Y. This integration is performed over a specific time window, which we designate as the polarization "integration sub-bin". To ensure the robustness of our results, it has been verified that the mean value of $\omega^{\tilde{\mathcal{N}}\tilde{\mathcal{E}}}$ is independent of the duration of the chosen sub-bin. This approach, drawing inspiration from recent advancements in statistical benchmarking techniques for assessing data concordance [125], was implemented to ensure the integrity and consistency of our experimental data.

Post-binning, the amplitudes of both F_X and F_Y pulses follow the envelope of the molecular pulse (Figure 3.1 (b)). We normalize against this slowly evolving amplitude by computing the asymmetry, A, for each polarization cycle between $\hat{X}$ and $\hat{Y}$ laser pulses.

The spin precession measurement in the ACME experiment is conducted repeatedly under various controlled conditions. These conditions, which we refer to as "switches," serve to isolate the EDM phase from background phases, as well as search for and monitor any potential systematic errors. Each switch is binary, with possible states of $+1$ or -1. This comprehensive set of switches allows for rigorous control of systematic effects, thereby ensuring the reliability of our EDM measurements. To obtain a single, accurate electron EDM measurement, we implement a series of four independent experimental switches, each of which must be reversed (see Figure 3.1 (c)):

- The $\tilde{\mathcal{N}}$ switch reverses the orientation of the molecular beam every 25 molecular pulses (approximately every 0.5 s). This is accomplished by adjusting the frequency detunings of the STIRAP laser. The molecular beam orientation alternates between parallel and antiparallel to the z coordinate in the laboratory frame.

- The $\tilde{\mathcal{E}}$ switch inverts the applied electric field once every four $\tilde{\mathcal{N}}$ state reversals (approximately every 2 s). This is achieved by inverting the voltage on the electric field plates. The electric field is applied along the z coordinate such that $\hat{\mathcal{E}} \cdot \hat{z} = \pm 1$.

- The $\tilde{\theta}$ switch modulates the relative angle between the readout and polarization bases. This switch occurs once every four $\tilde{\mathcal{E}}$ state reversals (about 8 s). The purpose of this switch is to enable us to measure the sensitivity of the asymmetry to small changes in phase, and determine the contrast of the measurement.

- The $\tilde{\mathcal{B}}$ switch reverses the direction of the magnetic field once every four $\tilde{\theta}$ state reversals (approximately every 32 s). This is accomplished by inverting the current in the magnetic field coils. The magnetic field is also applied along the z coordinate such that $\hat{\mathcal{B}} \cdot \hat{z} = \pm 1$.

We define a complete cycle of these four switch reversals as a "block," which typically spans approximately 60 seconds. In addition to the primary experimental switches discussed earlier, we implement a set of 'superblock' binary switches on a slower timescale. Figure 3.1 (d) illustrates the temporal sequence of these superblock switches in relation to the primary switches. They include:

- The $\tilde{\mathcal{P}}$ switch changes the the I state parity addressed by the state readout laser. Under this operation, the population with the $\hat{X}$ and $\hat{Y}$ transitions got interchanged, thus it eliminates

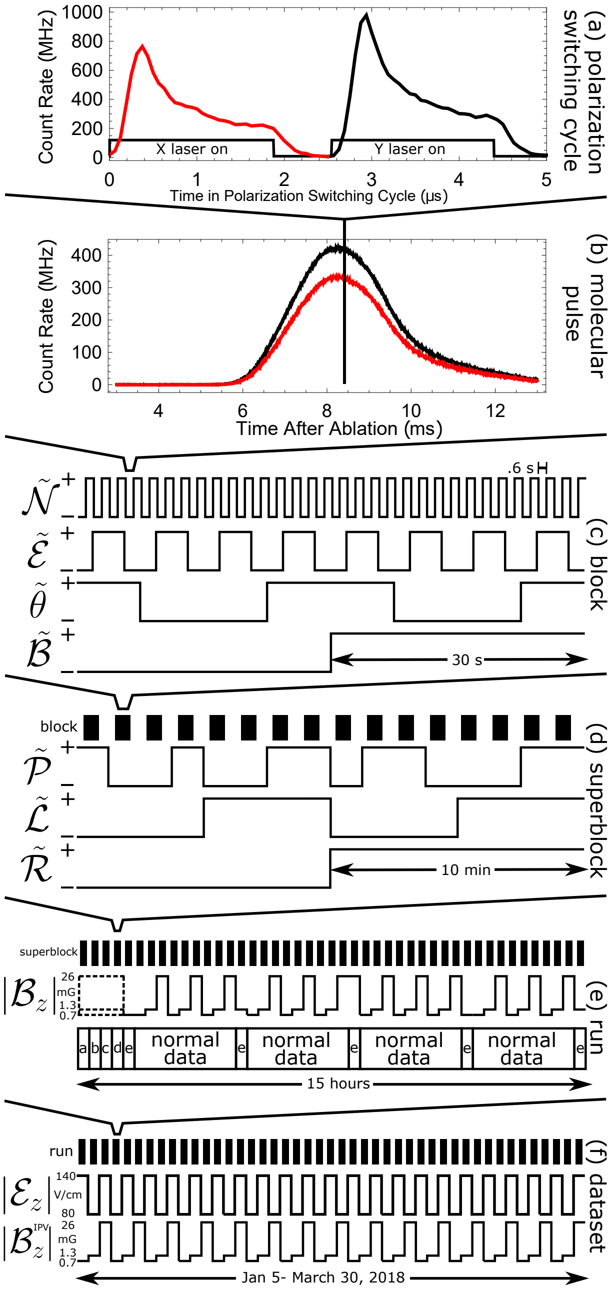

Figure 3.1: **Switching Timescales** **(a)** Fluorescence signal during an $\hat{X}$, $\hat{Y}$ polarization cycle. **(b)** Time-resolved molecular trace (25 averaged pulses) indicating the signal averaged across the entire $\hat{X}$ and $\hat{Y}$ polarization cycles. **(c)** Sequence of switches within a data block. **(d)** Switching configuration within a superblock. **(e)** Alternation between 'normal' EDM data, collected at three $|\mathcal{B}_0|$ values, and monitoring for known systematic effects via intentional parameter variations. **(f)** Composition of the whole EDM dataset. Taken from [81].

any asymmetry effects that manifest in our measurement due to imbalances between the readout beams.

- The $\tilde{\mathcal{L}}$ switch physically interchanges the voltage supplies on the $+V$ and $-V$ side electric field plates, in addition to the $\tilde{\mathcal{E}}$ switch. This is implemented using mercury-wetted relays controlled by TTL pulses, which eliminates the effect from power supply offsets, thus further suppresses the non-reversing $\mathcal{E}$ field, which may contribute to the systematic errors in EDM measurements significantly.

- The $\tilde{\mathcal{R}}$ switch rotates the readout $\hat{X}$-$\hat{Y}$ polarization basis by $\pi/2$, achieved by mechanically rotating a waveplate through which both X and Y laser beams pass. This provides an additional, independent method of interchanging the roles of the X and Y beams, offering a robust way of removing asymmetry effects.

The data acquisition protocol for our experiment employs a dual-pronged approach, alternating between two distinct operational modes (illustrated in Figure 3.1(f)). The primary mode involves collecting electron Electric Dipole Moment (eEDM) data under standard experimental conditions, where all parameters are meticulously calibrated to their optimal values. This is complemented by a secondary mode, wherein we intentionally introduce controlled variations in specific experimental parameters. This latter approach serves as a crucial tool for assessing the sensitivity of our EDM measurements to known systematic errors. We expect that the data-taking schemes employed in ACME III remains consistent with those utilized in ACME I and II, since the robustness and efficacy of these schemes have been demonstrated in previous iterations of the experiment. Our projected dataset for eEDM measurements under standard conditions is expected to encompass approximately 350 hours of data collection, yielding an estimated 20,000 experimental blocks. An additional 150 hours of interleaved data taking will be employed that is dedicated to systematic error checks. The entire data acquisition process is anticipated to span a period of approximately two months.

3.1.2 Statistics of the eEDM dataset

In our experimental setup, we employ a technique known as "switch parity sums" to analyze the measured phases [107]. This method involves summing the measured phases that exhibit odd or even behavior under specific switch operations. We denote the parity of a quantity with a superscript u, which enumerates all switch labels under which the quantity is odd. By convention, the quantity is assumed to be even under all unlabeled switches. The superscript "nr" is used to indicate that the quantity is even under all considered switches. The EDM phase Φ exhibits odd behavior exclusively under $\tilde{\mathcal{N}}$ and $\tilde{\mathcal{E}}$ switches, while remaining even under all other switches. Consequently, we extract the phase in the $\tilde{\mathcal{N}}\tilde{\mathcal{E}}$ channel using the following equation:

$$\Phi^{\mathcal{N}\mathcal{E}} = \frac{1}{2^3} \sum_{\tilde{\mathcal{N}}',\tilde{\mathcal{E}}',\tilde{\mathcal{B}}'=\pm 1} \left(\tilde{\mathcal{N}}'\right)\left(\tilde{\mathcal{E}}'\right) \Phi(\tilde{\mathcal{N}},\tilde{\mathcal{E}},\tilde{\mathcal{B}}) \tag{3.1}$$

To establish a relationship between measured phases and the electron EDM, we consider the equation 2.2 and 2.3:

$$d_e = -\frac{\hbar\Phi^{\mathcal{N}\mathcal{E}}}{\mathcal{E}_{\text{eff}}\tau} \tag{3.2}$$

In which the precise determination of precession time τ becomes crucial. In ACME, this is derived from the $\tilde{\mathcal{B}}$-odd Zeeman precession phases, as

$$\tau = \frac{\Phi^{\mathcal{B}}}{-g_H \mu_B |B|} \tag{3.3}$$

To mitigate potential experimenter bias in our results, we implemented a robust blinding procedure. This involved applying a hidden blind offset to the $\omega^{\mathcal{N}\mathcal{E}}$ frequency channel, effectively concealing the true mean of this channel until the completion of data acquisition and the determination of systematic errors. No alterations to the data analysis procedure or the dataset included in the final result were made subsequent to the removal of the blind. In ACME II, The blind offset was randomly generated from a Gaussian distribution characterized by a mean of zero and a standard deviation of $\sigma = 10^{-28}\, e \cdot \text{cm}$. This chosen distribution width was deliberately set to be twice the uncertainty of the previous best eEDM result. Blinding offset was systematically applied to all quantities directly related to the eEDM value, ensuring that any potential bias in the analysis or interpretation of results was minimized, as the true eEDM value remained unknown until the final stages of the experiment.

The analysis in ACME II progresses through several stages, including the computation of grouped asymmetries, state-by-state asymmetries and contrasts, and ultimately the extraction of phase information. One intricate part in this analysis is that the signal from the SiPM is naturally a Poisson process, which has been approximated as a Gaussian, but has distortion at the tails with large standard deviation. We implement data cuts to ensure that low-signal regions, where this approximation breaks down, do not compromise our results. Throughout this process, we carefully consider the statistical distributions of our derived quantities, accounting for correlations between variables and potential non-linear effects. We pay particular attention to the transition from the state basis to the parity basis, ensuring that our error propagation accurately reflects the statistical properties of our measurements. Finally, we calculate precession frequencies, taking into account the correlations between phases in the parity basis and the dependence of precession time on the measured magnetic field phase. This calculation has been refined based on recent advancements in network percolation theory in quantum systems [126]. Our analysis reveals that while certain higher-order corrections and covariances between measured quantities are theoretically important, their practical impact on our results is minimal given the current level of technical noise in the ACME II dataset [101, 100]. The data analysis protocol for ACME III will adhere to the methodologies previously employed in ACME I and ACME II, as these approaches have demonstrated consistent efficacy and reliability in prior experiments.

3.2 Systematic uncertainties

The ACME experiment was meticulously designed to enhance resilience against systematic errors that historically impacted eEDM measurements. Nontheless, extensive studies have been conducted for identifying potential unforeseen systematic errors and understanding the effects observed. We quantitatively assess systematic contributions to the eEDM measurement by examining the dependency of the eEDM frequency channel, $\omega^{\tilde{\mathcal{N}}\tilde{\mathcal{E}}}$, on deliberately exaggerated experimental imperfections and by conducting auxiliary measurements to gauge the typical magnitudes of these imperfections. Our systems are engineered to introduce imperfections significantly larger than those encountered under normal operational conditions to facilitate these investigations, ensuring that any systematic effects are confined well below our statistical sensitivity threshold.

3.2.1 Review of systematic effects in ACME II

In our quest to identify potential sources of systematic error, we conducted an extensive investigation by varying over 40 distinct experimental parameters beyond their typical operational range (see Figure 3.2). Our primary focus was to measure the impact of these variations on $\omega^{\tilde{\mathcal{N}}\tilde{\mathcal{E}}}$ and other parity components of both precession frequency ω and contrast $\mathcal{C}$.

We classified these parameters into two categories: Category I encompasses parameters with an ideal experimental value under normal conditions, where deviations represent experimental im-

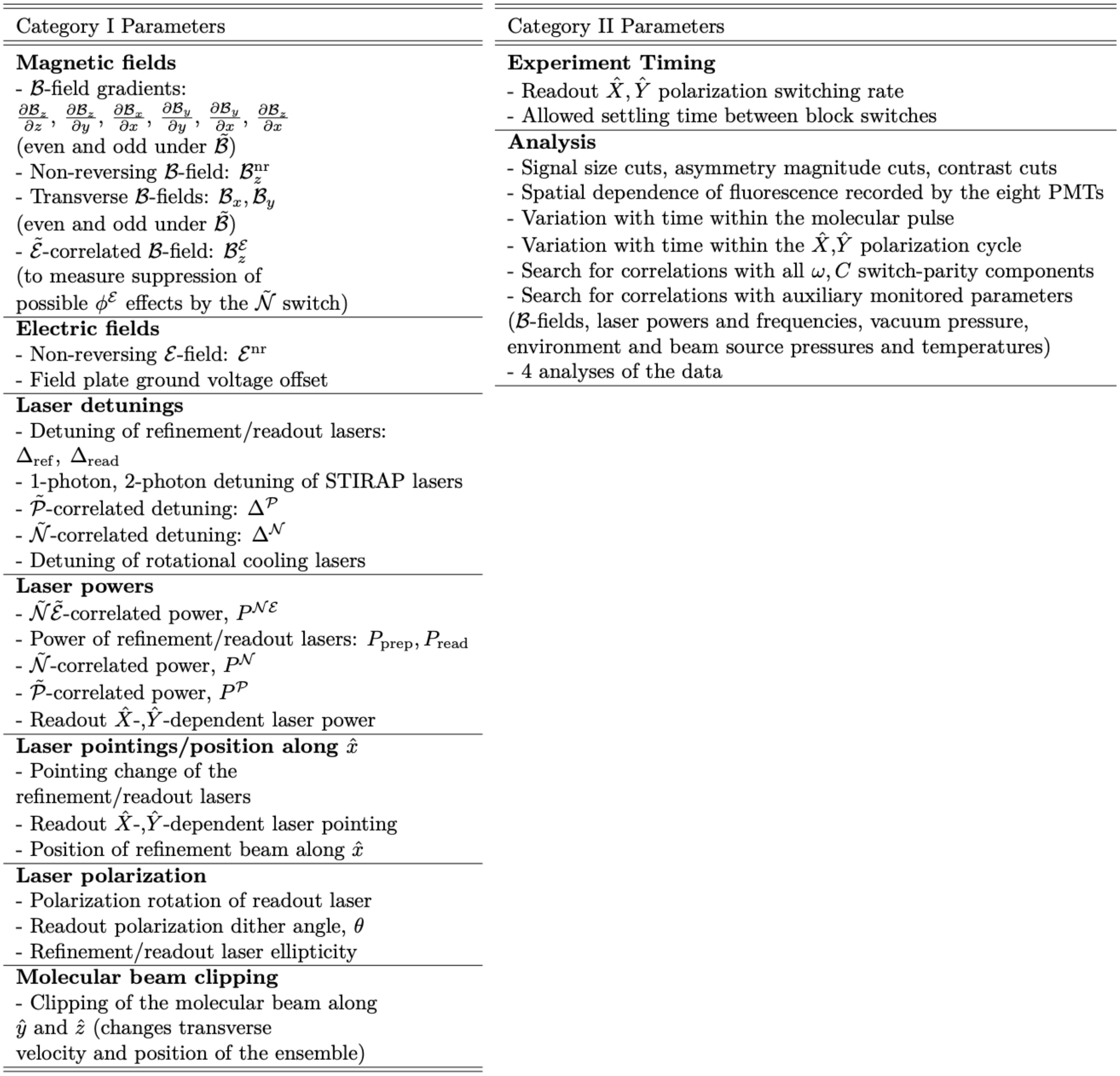

Category I Parameters
Magnetic fields - $\mathcal{B}$-field gradients: $\frac{\partial \mathcal{B}_z}{\partial z}, \frac{\partial \mathcal{B}_z}{\partial y}, \frac{\partial \mathcal{B}_x}{\partial x}, \frac{\partial \mathcal{B}_y}{\partial y}, \frac{\partial \mathcal{B}_y}{\partial x}, \frac{\partial \mathcal{B}_z}{\partial x}$ (even and odd under $\tilde{\mathcal{B}}$) - Non-reversing $\mathcal{B}$-field: $\mathcal{B}_z^{\mathrm{nr}}$ - Transverse $\mathcal{B}$-fields: $\mathcal{B}_x, \mathcal{B}_y$ (even and odd under $\tilde{\mathcal{B}}$) - $\tilde{\mathcal{E}}$-correlated $\mathcal{B}$-field: $\mathcal{B}_z^{\mathcal{E}}$ (to measure suppression of possible $\phi^{\mathcal{E}}$ effects by the $\tilde{\mathcal{N}}$ switch)
Electric fields - Non-reversing $\mathcal{E}$-field: $\mathcal{E}^{\mathrm{nr}}$ - Field plate ground voltage offset
Laser detunings - Detuning of refinement/readout lasers: Δ_{ref}, Δ_{read} - 1-photon, 2-photon detuning of STIRAP lasers - $\tilde{\mathcal{P}}$-correlated detuning: $\Delta^{\mathcal{P}}$ - $\tilde{\mathcal{N}}$-correlated detuning: $\Delta^{\mathcal{N}}$ - Detuning of rotational cooling lasers
Laser powers - $\tilde{\mathcal{N}}\tilde{\mathcal{E}}$-correlated power, $P^{\mathcal{N}\mathcal{E}}$ - Power of refinement/readout lasers: $P_{\mathrm{prep}}, P_{\mathrm{read}}$ - $\tilde{\mathcal{N}}$-correlated power, $P^{\mathcal{N}}$ - $\tilde{\mathcal{P}}$-correlated power, $P^{\mathcal{P}}$ - Readout $\hat{X}$-,$\hat{Y}$-dependent laser power
Laser pointings/position along $\hat{x}$ - Pointing change of the refinement/readout lasers - Readout $\hat{X}$-,$\hat{Y}$-dependent laser pointing - Position of refinement beam along $\hat{x}$
Laser polarization - Polarization rotation of readout laser - Readout polarization dither angle, θ - Refinement/readout laser ellipticity
Molecular beam clipping - Clipping of the molecular beam along $\hat{y}$ and $\hat{z}$ (changes transverse velocity and position of the ensemble)

Category II Parameters
Experiment Timing - Readout $\hat{X}, \hat{Y}$ polarization switching rate - Allowed settling time between block switches
Analysis - Signal size cuts, asymmetry magnitude cuts, contrast cuts - Spatial dependence of fluorescence recorded by the eight PMTs - Variation with time within the molecular pulse - Variation with time within the $\hat{X}$,$\hat{Y}$ polarization cycle - Search for correlations with all ω, C switch-parity components - Search for correlations with auxiliary monitored parameters ($\mathcal{B}$-fields, laser powers and frequencies, vacuum pressure, environment and beam source pressures and temperatures) - 4 analyses of the data

Figure 3.2: **Parameters varied in ACME II for systematic checks.** Category I parameters are the parameters with a certain desired value in an ideal EDM measurement, and were varied far from their values under normal conditions of the experiment. Category II parameters are the parameters that do not have a clear optimum value, and were varied to check for unanticipated systematic errors. Adapted from [81]

perfections. Category II includes parameters without a clear optimum value, to which the spin precession measurement is nominally insensitive. For each Category I parameter P, we deliberately exaggerated the magnitude of the imperfection, typically by a factor exceeding 10 relative to the maximum imperfection size under standard operating conditions ($\bar{P}$), as determined through auxiliary measurements. Assuming a linear relationship between $\omega^{\tilde{\mathcal{N}}\tilde{\mathcal{E}}}$ and P [82], we derived the sensitivity of $\omega^{\tilde{\mathcal{N}}\tilde{\mathcal{E}}}$ to P by calculating the slope:

$$S_P = \frac{\partial \omega^{\tilde{\mathcal{N}}\tilde{\mathcal{E}}}}{\partial P} \tag{3.4}$$

Data collected under these intentionally applied parameter imperfections were used exclusively for determining systematic shifts and uncertainties, and were not incorporated into the EDM dataset. We utilized these measured slopes to compute systematic shifts and uncertainties. In cases where S_P was either expected or observed to be non-zero, we calculated the associated systematic shift based on the the maximum size of the imperfection under typical running conditions $\bar{P}$:

$$\omega_P^{\tilde{\mathcal{N}}\tilde{\mathcal{E}}} = S_P \bar{P} \tag{3.5}$$

The uncertainty in $\omega^{\tilde{\mathcal{N}}\tilde{\mathcal{E}}}$ was determined using standard error propagation for uncorrelated variables:

$$\delta\omega_P^{\tilde{\mathcal{N}}\tilde{\mathcal{E}}} = \sqrt{(S_P \delta \bar{P})^2 + (\bar{P} \delta S_P)^2} \tag{3.6}$$

These systematic means and uncertainties were incorporated into the final systematic error budget (See Figure 3.2 for ACME II). All shifts of this nature were subtracted to compute a systematic-free eEDM frequency:

$$\omega^{\tilde{\mathcal{N}}\tilde{\mathcal{E}}}_{\text{corrected}} = \omega^{\tilde{\mathcal{N}}\tilde{\mathcal{E}}} - \sum_{P} \omega^{\tilde{\mathcal{N}}\tilde{\mathcal{E}}}_{P} \tag{3.7}$$

For the majority of Category I parameters that did not exhibit significant systematic slopes, we refrained from applying systematic corrections. However, we still computed upper limits on the associated uncertainties:

$$\delta\omega^{\tilde{\mathcal{N}}\tilde{\mathcal{E}}}_{P} = \bar{P}\sqrt{(S_P)^2 + (\delta S_P)^2} \tag{3.8}$$

where we estimated $\delta P \approx \bar{P}$. These uncertainties were included in the final systematic error budget as of ACME II shown in Figure 3.3.

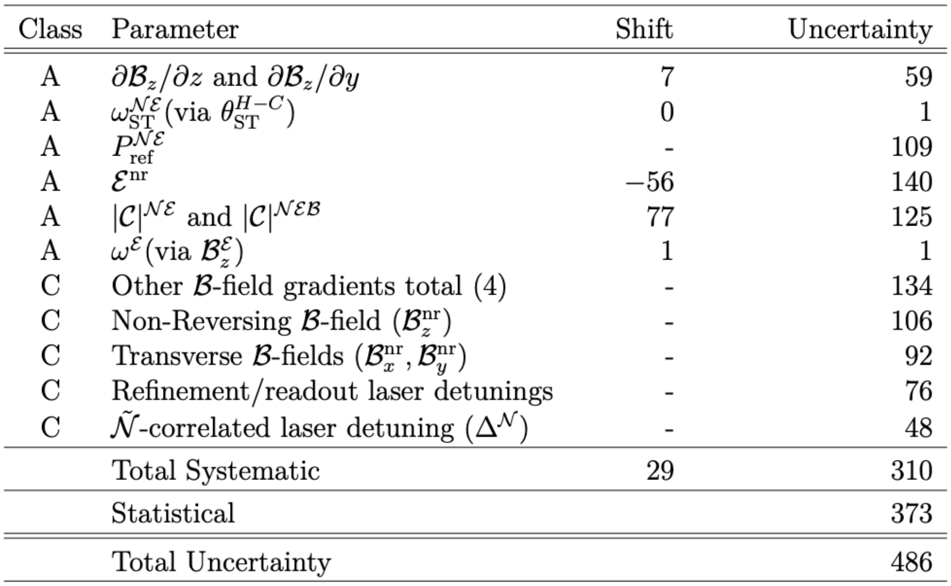

Class	Parameter	Shift	Uncertainty
A	$\partial\mathcal{B}_z/\partial z$ and $\partial\mathcal{B}_z/\partial y$	7	59
A	$\omega^{\mathcal{N}\mathcal{E}}_{\text{ST}}$(via θ^{H-C}_{ST})	0	1
A	$P^{\mathcal{N}\mathcal{E}}_{\text{ref}}$	-	109
A	$\mathcal{E}^{\text{nr}}$	-56	140
A	$\lvert\mathcal{C}\rvert^{\mathcal{N}\mathcal{E}}$ and $\lvert\mathcal{C}\rvert^{\mathcal{N}\mathcal{E}\mathcal{B}}$	77	125
A	$\omega^{\mathcal{E}}$(via $\mathcal{B}^{\mathcal{E}}_z$)	1	1
C	Other $\mathcal{B}$-field gradients total (4)	-	134
C	Non-Reversing $\mathcal{B}$-field ($\mathcal{B}^{\text{nr}}_z$)	-	106
C	Transverse $\mathcal{B}$-fields ($\mathcal{B}^{\text{nr}}_x, \mathcal{B}^{\text{nr}}_y$)	-	92
C	Refinement/readout laser detunings	-	76
C	$\tilde{\mathcal{N}}$-correlated laser detuning ($\Delta^{\mathcal{N}}$)	-	48
	Total Systematic	29	310
	Statistical		373
	Total Uncertainty		486

Figure 3.3: **Systematic shifts and their uncertainties in ACME II.** Units are in μrad/s. The total systematic uncertainty correspond to $\delta_{\text{sys}} = 2.6 \times 10^{-30}\, e \cdot \text{cm}$. Adapted from [81].

Given that the primary focus of this doctoral research lies in the precise control and manipulation of magnetic fields, their associated gradients, and the mitigation of magnetic noise, encompassing the design and implementation of magnetic shielding systems and self-shielding magnetic field coils, Section 3.2.2 will provide a discussion of the systematic effects specifically related to magnetic fields and their spatial gradients.

3.2.2 Systematic effects associated with magnetic field gradients

In the ACME II measurement, a particular set of systematic errors was identified that arose from magnetic field gradients, which is directly relevant to the work presented in this thesis. Panda [101] and Lasner [100] have developed a comprehensive understanding of these systematic errors, which are anticipated to persist in ACME III. These errors originate from a center-of-mass shift in the $\tilde{\mathcal{N}}\tilde{\mathcal{E}}$ channel in the molecular distribution along the z coordinate, induced by a non-reversing E field in the spin-precession volume, coupled with the magnetic field gradient in the same region. The mechanism can be described as follows:

1. **Position-Velocity Correlation:** The molecules' ballistic trajectories in the interaction region a strong position-velocity correlation, approximated by $z \approx v_z L$, with correlation coefficient found to be 0.98 in ACME II.

2. **Velocity-Dependent Detuning:** For a specific transverse-velocity class, the detuning Δ is proportional to its transverse velocity v_z, due to the Doppler shift $\Delta_{\text{Dop}} = v_z/\lambda$, where $\lambda = 703$ nm is the transition wavelength.

3. **Velocity-Selective Detection:** The readout beams, not being fully saturated, preferentially detect a particular velocity class where the total detuning is zero. The resonant velocity class for a given detuning value Δ is $v_{\text{res}} = -\Delta_0\lambda$.

4. **Position-Selective Detection:** Due to the position-velocity correlation, a preferred position class (value of z) is most efficiently detected: $z_{\text{res}} \approx -\Delta_0\lambda L/v_x$.

5. **Center-of-Mass Shift:** Given $\mathcal{E}_{\text{nr}} \sim 5$ mV/cm, this effect results in $\Delta^{\tilde{\mathcal{N}}\tilde{\mathcal{E}}} \sim 2\pi \times 5$ kHz in the cleanup and readout beams due to the Ω-doublet structure of the H state. This leads to a shift in the center of mass of the detected molecular population, $z_{\text{res}}^{\tilde{\mathcal{N}}\tilde{\mathcal{E}}} \sim -100\ \mu$m. In the presence of a magnetic field gradient $\partial B/\partial z$, a phase shift $\phi^{\tilde{\mathcal{N}}\tilde{\mathcal{E}}}$ is expected due to this effect, particularly in the limit of poor laser saturation.

This model applies to the limiting case of poor readout laser saturation. In the opposite case of perfect readout laser saturation, no systematic effect occurs because the readout efficiency becomes independent of $\Delta^{\tilde{\mathcal{N}}\tilde{\mathcal{E}}}$ (induced by $\mathcal{E}_{\text{nr}}$) and Δ. In reality, the saturation scenario lies between the two limiting cases in ACME II. A slope of $\frac{\partial \omega^{\tilde{\mathcal{N}}\tilde{\mathcal{E}}}}{\partial(\partial \mathcal{B}/\partial z)} \sim 100,\mu$rad/($\mu$G/cm) was observed prior to the suppression of this systematic error [100].

In consideration of the systematic slope elimination, the effect of this gradient on the STIRAP state transfer is contemplated. At any given location, the value of $\mathcal{E}_{\text{nr}}(z)$ induced by the gradient $\partial\mathcal{E}_{\text{nr}}/\partial z$ results in a correlated two-photon STIRAP detuning $\delta^{\tilde{\mathcal{N}}\tilde{\mathcal{E}}} = D(\partial\mathcal{E}_{\text{nr}}/\partial z)z$. The efficiency η of the STIRAP state transfer, dependent on the two-photon detuning $\delta \equiv (\Delta_{690} - \Delta_{1090})/2$, is then linearly dependent on z. Assuming a uniform population density of molecules entering the STIRAP beams along z with a half-width a, this would result in a shift in the transition center-of-mass along z. Here, a simple Gaussian 2-photon lineshape model is assumed [100]. In the limit of perfect STIRAP laser saturation, the transfer efficiency becomes independent of detuning, leading to the absence of any systematic effect. For a finite STIRAP two-photon linewidth and small two-photon detunings $\delta \ll \sigma_{\text{ST}}$, the center-of-mass shift is approximated by:

$$z_{\text{CM}}^{\tilde{\mathcal{N}}\tilde{\mathcal{E}}} \approx \frac{a^2}{3}\frac{\delta}{\sigma_{\text{ST}}^2} D \frac{\partial\mathcal{E}_{\text{nr}}}{\partial z}. \tag{3.9}$$

Thus, the effect of the two-photon detuning would behave the same way as the $\tilde{\mathcal{N}}\tilde{\mathcal{E}}$-correlated systematic effect with non-reversing $\mathcal{E}$ field and magnetic field gradients. We can adjust this parameter to compensate the systematic slope $\partial\omega^{\tilde{\mathcal{N}}\tilde{\mathcal{E}}}/\partial(\partial B/\partial z)$, to approximately zero. During ACME II, this slope was reduced to $\frac{\partial\omega^{\tilde{\mathcal{N}}\tilde{\mathcal{E}}}}{\partial(\partial\mathcal{B}/\partial z)} = -5.9(31)$ μrad/(μG/cm), much smaller than without the compensation case, and is consistent with zero. Furthermore, the compensating field gradients are applied during the EDM data-taking in ACME II, achieving an ambient magnetic field gradient after compensation, $(\partial B/\partial z)_{\text{comp}} = -0.5(60)$ μG/cm. The combination of the two measures result in the systematic error being reduced below the shot-noise limit of ACME II. However, In ACME III, the systematic error must to be reduced by a factor of 40 alognside with the improvements on experiment sensitivy. Thus, the magnetic field gradient requirements are expected to be more stringent, as will be discussed in Section 4.1.

It is worth mentioning that using δ to minimize the systematic slope is analogous to using the $\partial E_{\text{nr}}/\partial z$ contribution to counteract the E_{nr} contribution, thus the minimization of the systematic slope is not achieved independently [101]. Similar models applies to another observed systematic effect $\frac{\partial\omega^{\tilde{\mathcal{N}}\tilde{\mathcal{E}}}}{\partial(\partial\mathcal{B}/\partial y)}$, which has a magnitude similar to the $\frac{\partial\omega^{\tilde{\mathcal{N}}\tilde{\mathcal{E}}}}{\partial(\partial\mathcal{B}/\partial z)}$ systematic slope. The same compensation method is applied to this systematic effect, with the resulting systematic error being summarized in Table 4.1.

3.3 Statistical uncertainties

The analysis of superblock data in the ACME II measurement revealed an unexpected level of scatter exceeding the anticipated shot-noise from group-level uncertainties. This excess noise was uniformly distributed across all switch parity components of the frequency and showed no temporal variation post-ablation. Further investigation uncovered two distinct components contributing to this excess noise in the precession frequency: one proportional to the applied magnetic field magnitude, $\mathcal{B}_0$, and another independent of it.

The $\mathcal{B}$-independent noise component introduced an uncertainty approximately 1.7 times above the shot-noise limit, corresponding to a reduced chi-squared value of $\chi_r^2 \sim 3$. This noise component was particularly notable because our fastest switch, $\tilde{\mathcal{N}}$, was unable to mitigate it, resulting in its manifestation in measurements at timescales shorter than 0.6 seconds. The origin of this frequency noise is inherent to the ACME experiment's fast polarization switching scheme. The internal clock of the DAQ digitizer, responsible for sampling and digitization timing, introduced variable trigger delays when not synchronized with an external clock [101]. This resulted in time axis offsets of up to $\sim$ 100 ns for subsequent molecular pulses, accumulating at about 10 ns per pulse and resetting every 10 pulses in a sawtooth pattern. The inconsistency in acquisition timing led to noise in the asymmetry calculations when fluorescence signal magnitude varied between adjacent acquisition points. It persists regardless of the switch operations, affecting neither the $\omega^{\mathcal{N}\mathcal{E}}$ channel nor other odd measurement channels.

To mitigate this, ACME II implemented several strategies [113, 123], including using an external Rubidium reference clock for synchronization, adjusting acquisition settings, and integrating over larger sub-bins in the polarization switching process. These measures effectively reduced the timing-related noise below the projected shot-noise level in the original ACME II setup, as confirmed by subsequent data acquisition showing statistical consistency with an ideal distribution [127].

In addition to the noise associated with timing, the other noise source, which was found to be proportional to the magnitude of the applied magnetic field $\mathcal{B}_0$, introduces unique challenges and implications for the experiment's precision. The following section will provide an in-depth examination of this magnetic field-dependent noise, its characteristics, and its implications in the development of ACME III.

3.3.1 Noise in precession time coupled with magnetic fields

The magnetic-field-induced noise in ACME II substantially increased the scatter in our data, elevating the reduced chi-squared value, χ_r^2, to approximately 7. Notably, this effect was only observed at higher applied magnetic fields, specifically at $|\mathcal{B}_0| = 26$ mG in ACME II. Further diagnostic measurements at $|\mathcal{B}_0| = 52$ mG, corresponding to a Zeeman precession phase of π, corroborated this field-dependent noise increase. Simulations and direct measurements [101] indicated that this noise is consistent with approximately 0.05% shot-to-shot fluctuations in the mean longitudinal molecular velocity ($\langle v \rangle \approx 200$ m/s). The mechanism underlying this noise can be understood as follows: given that the refinement and readout laser beams are spatially fixed, variations in $\langle v \rangle$ alter the precession time τ, inducing phase variations ϕ that scale with $|\mathcal{B}_0|$, as detailed in Section 2.2.

To quantify these fluctuations, we implemented a novel measurement technique involving a notch in the STIRAP 690 nm pump beam. This method allowed us to directly measure the transit times of molecules and, consequently, the variations in precession time τ. The procedure involved adding an AOM in the STIRAP pump beam path to modulate laser power, and using a fast RF switch to turn off the pump beam for $100\,\mu$ s, quenching state preparation. This technique produced a dip in the molecule fluorescence signal, which, due to the local velocity dispersion of the molecular beam, resembled a Gaussian rather than a square shape. The observed broadening was consistent with the known 10% velocity dispersion of the ThO molecule beam [112]. By fitting a Gaussian function to this dip and tracking the peak's position over time, we quantified fluctuations in τ, which typically amounted to about 0.1% rms. These fluctuations largely account for the observed excess noise that is proportional to $\mathcal{B}_0$. The velocity variation is linked to shifts in the ablation laser's impact point on the ceramic ThO target, although a detailed investigation of each ablation parameter has not been conducted.

The phase noise associated with applied magnetic fields can be expressed quantitatively. Considering the standard deviation of the forward velocity among distinct traces as σ_v, the associated phase noise can be expressed as:

$$\sigma_\phi \approx |g|\mu_B \mathcal{B}\frac{L}{v}\frac{\sigma_v}{v} = |\phi_{\text{Zeeman}}|\,\frac{\sigma_v}{v} \tag{3.10}$$

Where, if $\sigma_v \sim 0.1\%$, this would correspond to a Zeeman phase noise that is 10^{-3} of the Zeeman phase, consistent with the observed noise levels at $\mathcal{B}_0 = 26$ mG in ACME II.

The observation that the $\mathcal{B}_0$-dependent noise scales with magnetic field magnitude suggests that careful control and potential reduction of the applied magnetic field is necessary for noise reduction. While the noise in the precession time τ is expected to remain similar in ACME III, the projected sensitivity of the experiment is anticipated to improve by a factor of 40. Consequently, more stringent magnetic field requirements will be necessary, as will be discussed in Section 4.1.

CHAPTER 4

MAGNETIC SHIELDING SYSTEM

One central challenge for various types of EDM measurements is the phase noise induced by magnetic field variations [128, 129]. The H state of the ThO molecules used in ACME experiment is much less sensitive to magnetic fields than many other EDM measurement systems, primarily due to the small g factor $g_H = 0.0088$ [104]. However, the magnetic-field-related noises and systematic errors are still a major concern. In Sections 3.2.2 and 3.3.1, we discussed the physical mechanism of the noise introduced by magnetic fields and the systematic errors caused by the magnetic field gradients. In this chapter and in a manuscript soon to be published [130], we will discuss the requirements on the magnetic field to suppress these effects, as well as the design and construction of the magnetic shielding system for reaching the field requirements.

4.1 Magnetic field requirements

In the ACME experiment, the measured electron EDM is proportional to the spin-precession frequency in the EDM channel, $\omega_{\tilde{\mathcal{N}}\tilde{\mathcal{E}}}$, as $d_e = -\frac{\hbar\omega^{\tilde{\mathcal{N}}\tilde{\mathcal{E}}}}{\mathcal{E}_{\text{eff}}}$. The ACME II shot-noise limit was

$220\,\mu$rad/s, which corresponds to $1.8 \times 10^{-30}\,e \cdot$ cm. However, the actual achieved sensitivity is $373\,\mu$rad/s, which is about 1.7 times as large as the shot-noise limit [81]. The excess statistical error came from timing imperfections. The timing imperfections have since been eliminated to reach the shot-noise limit for the same experiment configuration as ACME II [127].

Considering that we're still using the same ThO molecules with the same state preparation and detection protocols, we expect the shot-noise limit of the ACME III measurement to scale to [113]:

$$\sigma_{\omega_{\tilde{\mathcal{N}}\tilde{\mathcal{E}}}} \sim 5.5\,\mu\text{rad/s} \tag{4.1}$$

The requirement on the magnetic field is two fold: first, the magnetic field should not introduce statistical phase noise uncertainty that exceeds the shot-noise limit; second, the magnetic field should not introduce any systematic errors larger than the statistical noise, meaning that both the value and the uncertainty of the systematic error should be small. Assuming uncertainties from different source add up quadratically, based upon empirical experience in ACME I and ACME II, we think that suppressing the statistical and systematic errors associated with magnetic fields below $2\,\mu$rad/s will permit a shot-noise limited eEDM measurement.

The magnetic field in the spin-precession volume is a superposition of an applied bias field $\mathbf{B} = B_z\hat{z}$ produced by a magnetic field coil, and a unwanted residual field $\mathbf{B}_{\text{res}}$ that is from the shielded ambient magnetic field environment and the residual magnetization of our apparatus, primarily the magnetic shields. The applied bias field that is necessary to drive the spin-precession of the ThO molecules also converts ThO velocity fluctuations into measured phase fluctuations. This limits the magnitude of the applied bias field and the residual field allowed in the spin-precession volume. Since we're using a similar laser-ablation buffer gas beam of ThO as in ACME II, we expect its velocity characteristics remain at $\left(\frac{\sigma_v}{v}\right)_{\text{trace}} \sim 10^{-3}$ for each trace (25 pulses) of molecules. It averaged down to $\left(\frac{\sigma_v}{v}\right)_{\text{total}} \sim 6 \times 10^{-7}$ for the the 2.5×10^{6} traces of data taken in ACME II. This averaging assumes purely stochastic velocity fluctuations between traces, with uncertainty scaling as $\frac{1}{\sqrt{N}}$. Although ACME II exhibited some correlated velocity drift between traces, careful analysis demonstrated that this effect was minimal, and the total Zeeman phase uncertainty remained consistent with the random velocity drift model [100].

If we require $\sigma_{\omega_{\text{Zeeman}}} \leq 2\,\mu$rad/s, the Zeeman angular precession frequency must not exceed 3.2 rad/s, corresponding to a total magnetic field of $|\mathbf{B}| \sim 100\,\mu G$. It is noteworthy that while 2.5×10^6 traces were used to estimate the effect of magnetic fields coupled with velocity dispersions, the magnetic field requirements for a shot-noise limited measurement are independent with the number of traces. This is because both the Zeeman phase noise and the shot noise scale with $\frac{1}{\sqrt{N}}$, maintaining their relative significance regardless of the number of traces. Thus, we choose to apply the bias field with $B_z = 100\,\mu G$. We aim to control $|\mathbf{B}_{\text{res}}| < 10\,\mu G$ so that the residual field does not distort the applied uniform field significantly and create large asymmetry effect for the applied field in one direction or the other.

The residual magnetic field in the spin-precession volume does not contribute directly to the systematic errors in eEDM measurements, because the Zeeman phase will be averaged out through switching in $\tilde{\mathcal{N}}$ and $\tilde{\mathcal{E}}$. However, a non-reversing field gradient can shift the spin-precession phase in a way that is $\tilde{\mathcal{N}}\tilde{\mathcal{E}}$-correlated. As described in section 3.2.2, the slopes associated with this effect, $\frac{\partial \omega^{\tilde{\mathcal{N}}\tilde{\mathcal{E}}}}{\partial(\partial \mathcal{B}/\partial z)}$ and $\frac{\partial \omega^{\tilde{\mathcal{N}}\tilde{\mathcal{E}}}}{\partial(\partial \mathcal{B}/\partial y)}$, can be tuned out by adjusting the two-photon detuning δ of the STIRAP. In ACME II, these slope was found initially to be around $100\,(\mu$rad/s$)/(\mu$G/cm$)$, while a careful adjustment of δ resulted in a much improved value of $-5.9 \pm 3.1\,(\mu$rad/s$)/(\mu$G/cm$)$ [100], in which the slope value and its uncertainty is on the same order of magnitude. The determination of magnetic field gradient in the spin-precession volume, however, is limited by the magnetometer setup in the apparatus and the large residual field in ACME II. Zack Lasner summarized the systematic effect of magnetic field gradients in Table 4.1. Systematic effects associated with uniform fields are also shown in the same table, while $B_{\text{nr}} = \mathbf{B}_{\text{res}} \cdot \hat{z}$ is denoted as the residual magnetic field along $\hat{z}$ direction, which is non-reversing when the applied magnetic field changes to opposite direction.

gradients (fine-tuned)	slope $[(\mu\text{rad/s})/(\mu\text{G/cm})]$	values $[\mu\text{G/cm}]$	limit $[\mu\text{rad/s}]$
$\partial B_z/\partial z$	-5.9 ± 3.1	1 ± 6	40
$\partial B_z/\partial y$	-6.5 ± 3.4	1 ± 6	44
gradients (no influence)	slope $[(\mu\text{rad/s})/(\mu\text{G/cm})]$	values $[\mu\text{G/cm}]$	limit $[\mu\text{rad/s}]$
$\partial B_x/\partial x$	-7.2 ± 5.2	1 ± 6	55
$\partial B_y/\partial y$	0.1 ± 6.5	1 ± 5	51
$\partial B_x/\partial y$	-5.0 ± 4.2	1 ± 10	66
$\partial B_z/\partial x$	2.5 ± 16.8	1 ± 5	86
fields	slope $[(\mu\text{rad/s})/\mu\text{G}]$	values $[\mu\text{G}]$	limit $[\mu\text{rad/s}]$
B_x	$(5.8 \pm 23.4) \times 10^{-3}$	300	73
B_y	$(-59 \pm 31.6) \times 10^{-3}$	150	50
B_{nr}	$(-201 \pm 1136) \times 10^{-3}$	80	106

Table 4.1: **Magnetic field gradients and their effects in ACME II.** Systematic effects associated with uniform fields are also shown. The dependence of $\omega^{\tilde{\mathcal{N}}\tilde{\mathcal{E}}}$ with corresponding gradients or fields (slope) are all consistent with zero, although uncertainty remains. Together with the typical values of unintended fields and gradients (see column 3), this determines the upper limit of systematic effects (column 4). Typical parameter values were obtained by placing conservative limits on the ambient magnetic fields or gradients in the spin-precession volume monitored throughout the experiment. Taken from [100].

As we can see, after tuning the magnetic field gradient systematics, the dependence of $\omega^{\tilde{\mathcal{N}}\tilde{\mathcal{E}}}$ with corresponding gradients or fields (the slope) are all consistent with zero. However, the large uncertainties of the gradients in the spin-precession volume, together with the uncertainties of the slope, creates a systematic uncertainty of the eEDM value. We choose to use a conservative estimation that the precision for the systematic checks will remain the same in ACME III. As the precession time was increased by 5 times in ACME III, we expect the sensitivity in frequency measurements to be improved by the same factor as well, i.e. $3.4\,(\mu\text{rad}/s)/(\mu\text{G/cm})$. As a general design goal, if we can accurately determine that the field gradients are less than $1\,\mu$G/cm, The related systematic errors will remain small comparing with the shot-noise limit in ACME III.

Following the discussion on static electric and magnetic field influences in the previous sections, it is crucial to address the effects of oscillatory fields, specifically how they contribute to time-average energy shifts in quantum systems. Similar to the static Stark and Zeeman effects, oscillatory fields lead to phenomena known as AC Stark and AC Zeeman shifts. These shifts can be understood analogously to their static counterparts within a rotating reference frame and are integral in understanding systematic errors in precision measurements. These effects, also known as geometric phases, have been extensively documented in literature [131, 132]. Although geometric phases are of a major concern in many types of the eEDM measurements, the Ω-doubling structure of the ThO H state provides significant suppression to these effects [133, 124]. Thus, the main concern for the magnetic fields in ACME III are the static fields and gradients.

The extremely small slope for uniform fields shown in Table 4.1 also agree with our previous estimation that the unintended field alone does not affect the eEDM measurement. The largest slope and the uncertainty here comes from the B_{nr} field. A conservative estimation, given that the slope remains the same and the uncertainty of slope reduce by $5\times$ due to the improved precession time, the systematic limit for a $10\,\mu$G residual field is about $3\,\mu$rad/s, lying below the shot-noise limit. Thus, the goal for ACME III is:

$$|\mathbf{B}_{\text{res}}| \leq 10\,\mu\text{G}, \quad \frac{\partial|\mathbf{B}|}{\partial x_i} \leq 1\,\mu\text{G/cm} \tag{4.2}$$

The field that we are fighting against, the ambient magnetic field in the lab, is characterized in Figure 4.1. The data shown is measured roughly 2 m above the designated space of ACME III spin-precession volume. The measured average in this example is 522 ± 2 mG variations. This field is primarily the earth's field, as its directions and amplitudes agree with the geomagnetic data at Chicago area. However, fields averaging between 0.4 and 0.6 G are measured at nearby locations in the lab, depending upon the proximity of magnetized equipment and apparatus. The fluctuations

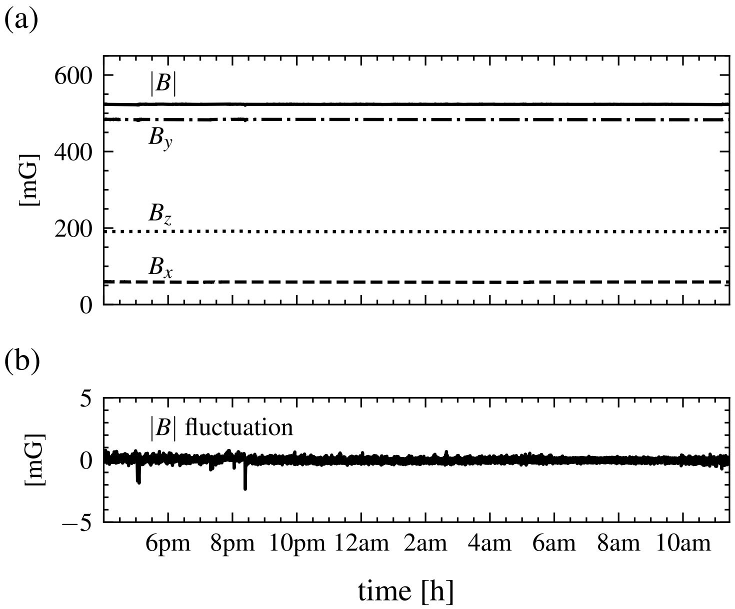

Figure 4.1: **The ambient magnetic field in the ACME lab.** (a) for each field component and the amplitude and (b) the amplitude change relative to its mean values.

are more than two orders of magnitude smaller than the average field values, so the lab field could be essentially regarded as stable in time. This requires reducing the DC component of the field by about a factor of 10^5, and the reduction of the smaller field temporal fluctuations by a factor of 10^3.

4.2 Principles of magnetic shielding

4.2.1 Ferromagnetic flux-shunting

The most common magnetic shielding utilizes high-permeability materials [134]. The magnetic flux in the space tends to pass through the domain with higher permeability rather than the air. Thus, an enclosed cage with a thin layer of high-permeability material would shunt the external magnetic flux and results in a much smaller field in the shielded volume.

In general, the permeability of ferromagnetic alloys, such as iron, nickel and cobalt alloys, could have a relative permeability of $10^3 \sim 10^5$. This is due to their unique magnetic domain structure that makes them easy to be magnetized. In contrast, the paramagnetic or diamagnetic materials are having relative permeability close to 1. This makes the ferromagnetic materials ideal for magnetic shielding. However, their domain structure also causes saturation and hysteresis that are challenges to effective magnetic shielding. We will discuss these effects in section 4.4.

Depending on the frequency of the external magnetic fields, ferromagnetic shielding occurs through different physical mechanisms. For static and low-frequency fields, the most important mechanism is the described flux shunting. At higher frequencies, the eddy-current effect starts to play an essential role, which cancels the change of external field and thus provides additional shielding. Practically, a ferromagnetic shield optimized for shielding static fields automatically provides efficient shielding of oscillating fields within the frequency range below a few kHz [134].

The shielding performance of a magnetic shield is characterized by the shielding factor, defined simply as the ratio of the external field to the internal field:

$$\mathrm{SF} = \frac{B_e}{B_i} \tag{4.3}$$

This definition is based on an over-simplified model that the external field is uniform. In this case, the internal field would also be largely uniform for most shield geometries. Nevertheless, it provides an efficient way to estimate the field-reduction capability of a shield. The accurate determination of the shielding factor of a certain shield requires solving the Maxwell's equations with the proper boundary conditions set up on the shield surface, which is usually implemented by the finite-element method (FEM) or other numerical methods. Here I introduce another intuitive yet accurate model to estimate the shielding factor of a shield, incorporating the theory of magnetic circuits [135]. For an static magnetic field, the Maxwell's equations, together with constitutive relations, governs the field:

$$\nabla \cdot \mathbf{B} = 0, \quad \nabla \times \mathbf{H} = 0, \quad \mathbf{B} = \mu\mathbf{H} \tag{4.4}$$

We notice that these equations are in the identical form to the equations for static electric circuits:

$$\nabla \cdot \mathbf{j} = 0, \quad \nabla \times \mathbf{E} = 0, \quad \mathbf{j} = \sigma\mathbf{E} \tag{4.5}$$

The analogy $\mathbf{B} \leftrightarrow \mathbf{j}$, $\mathbf{H} \leftrightarrow \mathbf{E}$ and $\mu \leftrightarrow \sigma$ suggests that the distribution of magnetic field would be identical for a electric current distribution given the same geometry boundary conditions. The resistance of an imperfect conductor of length l and cross-sectional area A is $R = \frac{l}{\sigma A}$. The analogous "magnetic resistance" of a magnetic path is:

$$R_m = \frac{l}{\mu A} \tag{4.6}$$

Where l is the length of the magnetic path, A is the cross-sectional area of the path, and μ is the permeability of the material. As shown in Figure 4.2 from [134], the scenario of magnetic shielding can be regarded as a distribution of magnetic flux over two magnetic resistors, corresponding to the shield domain and the internal air domain, respectively. The shielding factor can be calculated as:

$$\text{SF} = \frac{B_o}{B_i} = \frac{\Phi_o}{\Phi_{in}} = 1 + \frac{R_s}{R_f} = 1 + \frac{\mu_r l_s A_f}{l_f A_s} \tag{4.7}$$

Where μ_r is the relative permeability of the shielding layer, l_s and l_f are the average flux path length in the internal sheilded domain and the ferromagnetic domain, A_s and A_f are the average cross-sectional area of the two domains. If the shield is in a simple geometry with characteristic length D and the shield thickness t, the shielding factor reduces to

$$\text{SF} \sim 1 + \frac{\mu_r t}{D} \tag{4.8}$$

For most of high-permeability materials with $\mu_r \sim 10^3 \sim 10^5$, the second term dominates, even with a thin shield of only $1 \sim 10\,\text{mm}$. The shielding factor is linearly proportional to the relative permeability of the shield, as well as the thickness of the shield. This agrees with the situation demonstrated in Figure 4.2 (b), where stacking multiple layers of shields is equivalent to increasing the thickness of a single-layer shield, and the shielding factor is increased linearly as effectively parallelizing the shunt resistors for external magnetic flux.

The multi-layer shield with air gap between layers, as shown in Figure 4.2 (c), is a completely different situation. It turns out that the introduction of the air gap resistance R_{s2} makes it much more efficient to reduce the internal flux $\Phi_{\text{in}1}$. Taking a simplified case where the two layers of shield are of similar size, $D_2 \approx D_1 = D$, but their spacing $d = D_2 - D_1$ is significant compared with t, The shielding factor would become:

$$\text{SF} = \frac{B_o}{B_{\text{in}1}} \approx \left(2 + \frac{\mu_r d t}{D^2}\right)\left(1 + \frac{\mu_r t}{D}\right) \tag{4.9}$$

With the presence of d, a term proportional to μ_r^2 is introduced, and obviously will dominate if μ_r is large enough. Thus, compared with multi-layer closely-stacked shields in which their shielding factor are added up linearly, the multi-layer shield with air gap gets multiplicative shielding factor, which is the key to achieve a high shielding factor of $10^5 \sim 10^6$ in practice.

The magnetic circuit model provides a way to estimate the magnetic field inside the ferromagnetic shielding layers. This is basically

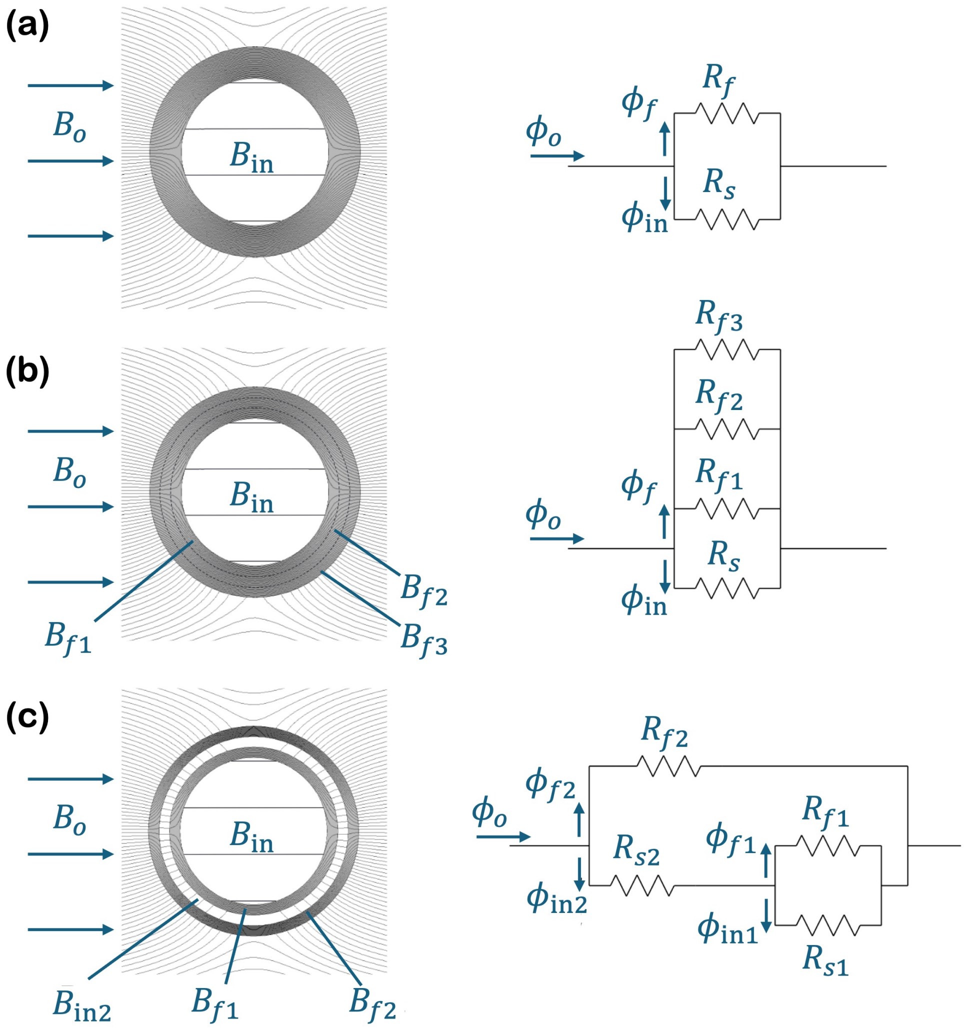

Figure 4.2: **The magnetic circuit model for magnetic shielding.** (a) The shielding of magnetic field is equivalent to shunt the air resistance R_s by a small shunt of shield R_f. (b) Stacking multiple layers of shields can further reduce the magnetic field as parallelizing the shunt resistors. (c) Muiltiple layers with air gap between layers. The introduction of air gap resistance R_{s2} makes it much more efficient to reduce the internal flux Φ_{in1}. Adapted from [134].

$$B_f = \frac{\Phi_f}{A_f} \approx \frac{B_o D}{t + \frac{D}{\mu_r t}} \tag{4.10}$$

For $\mu_r \gg 1$, the denominator is approximately t, and depends purely on the dimensions of the shield. This equation is useful in estimating if the ferromagnetic layer has been saturated. For a typical material with $B_{\text{sat}} \sim 0.5\,\text{T}$, a shield with $D \sim 1\,\text{m}$ and $t \sim 1\,\text{mm}$ would saturate at $B_o \sim 500\,\mu\text{T}$. This is about 10 times as the magnitude of the $\sim 50\mu\text{T}$ geomagnetic field. For lab environments with larger ambient fields, or for shields using thinner ferromagnetic layers, the saturation effect must be more carefully considered.

Computing the shielding factor explicitly is possible for simple geometries. The two explicitly-solvable cases, the spherical and inifite-long cylindrical shield, are calculated by A. Mager as early as in 1970s [136]. We briefly discuss the results here in order to provide insights for the design and estimation of magnetic shields.

4.2.2 Spherical shields

A spherical shield is isotropic in all directions, its shielding factor is independent of the direction of the external field. For a single-layer spherical shield with $D \ll t$,

$$\text{SF} = 1 + \frac{4}{3}\frac{\mu_r t}{D} \tag{4.11}$$

The form of the equation is very similar to Eq. 4.8, with only difference being the shape factor $4/3$ in front of the shielding term. Spherical shields have the largest shape factor among all geometries and thus provide the best shielding factor for a given thickness. For an uniform ambient field, spherical shields also provide the uniform internal field.

A concentric double layer spherical shield with air gap between the two layers has a shielding factor of:

$$\mathrm{SF}_{\text{total}} = 1 + \mathrm{SF}_1 + \mathrm{SF}_2 + \mathrm{SF}_1 \cdot \mathrm{SF}_2 \left(1 - \frac{D_1^3}{D_2^3}\right) \tag{4.12}$$

Where SF_1 and SF_2 are the shielding factors of the two individual layers assuming no other ferromagnetic objects nearby, and D_1 and D_2 are the radii of the two layers. When $D_1 \sim D_2$, this reduces to Eq. 4.9. As we can see, to get the significant amount of multiplicative shielding term, the two radii should be as different as possible. The total shielding factor for three or more layers can be calculated with compositing the shielding factors of each pair of layers.

If we plug Eq. 4.11 into Eq. 4.12, it can be noticed that there is a optimal ratio between the shield radius that maximizes the total shielding factor. For concentric spherical shields with equal thicknesses, $D_2/D_1 = \sqrt[3]{4} \approx 1.59$ [137]. In practice, a shield is built that needs to be large enough to enclose the entire experimental apparatus, i.e. D_1 is fixed. The optimal D_2 would be too large that requires a large amount of extra space for the shield, which could be improved by inserting more layers of shields to increase the total shielding factor with slightly reduced optimum. Paperno *et, al.* [138] showed that by choosing $D_2/D_1 = 1.32$, a 90% performance could be reached. In most of the application cases, the optimal ratio is way too large that increasing the the air gap between layers would always increase the total shielding factor. Thus, the actual design of the shield is a trade-off between the shielding performance and the space consumption.

4.2.3 Cylindrical shields

For the cylindrical shield, the shielding factor is dependent on the direction of the external field. For a infinite-long cylindrical shield, the transverse shielding factor (external field perpendicular to the cylinder axis) is:

$$\mathrm{SF}_t = 1 + \frac{\mu_r t}{D} \tag{4.13}$$

The shape factor of the cylindrical shield is 1, smaller than the spherical shield. The cylindrical shield also possesses the property of producing a uniform internal field for an uniform external transverse field.

The longitudinal shielding factor of a cylindrical ferromagnetic shield (where the external field is parallel to the cylinder axis) is unexpectedly 1. This phenomenon can be understood from two key factors:

- Translational symmetry: The field and geometry along the cylinder axis prevent any distortion of the ambient field by the ferromagnetic layer.
- Scaling of shield dimensions: As the shield's length (L) increases, the magnetic flux it must absorb grows proportionally to L^2, while its cross-sectional area ($\pi D t$, where D is diameter and t is thickness) remains constant. Consequently, the shield's ability to absorb flux diminishes with increasing length.

Thus, longitudinal shielding factor decreases rapidly as the shield's length increases. Numerical solutions show that for a cylindrical shield with $L = D$, $\mathrm{SF}_l \approx 0.9\mathrm{SF}_t$ [134]. A more accuate model of how the longitudinal shielding factor decreases with the aspect ratio L/D can be found in [139].

For multi-layer cylindrical shields, the total shielding factor has a similar form:

$$\mathrm{SF}_{t,\text{total}} = 1 + \mathrm{SF}_{t1} + \mathrm{SF}_{t2} + \mathrm{SF}_{t1} \cdot \mathrm{SF}_{t2} \left(1 - \frac{D_1^2}{D_2^2}\right) \tag{4.14}$$

$$\mathrm{SF}_{l,\text{total}} = 1 + \mathrm{SF}_{l1} + \mathrm{SF}_{l2} + \mathrm{SF}_{l1} \cdot \mathrm{SF}_{l2} \left(1 - \frac{L_1}{L_2}\right) \tag{4.15}$$

Where SF_{t1}, SF_{l1} are the individual transverse and longitudinal shielding factors, respectively. Although these equations have very similar forms, note that Eq. 4.14 is the exact solution for transverse shielding [136], while Eq. 4.15 is a numerical approximation [140].

4.3 Design of ACME III magnetic shielding system

4.3.1 Design concepts

Based on our understanding of the magnetic shielding principles and the requirements on the magnetic field for ACME III, we set up the following design objectives for the magnetic shielding system:

- The inner dimension of the magnetic shield needs to be large enough to enclose the entire apparatus, including the electric field plates, fluoresence collection optics, vacuum chamber, magnetic field coils, and the support structures, The outer dimension of the shield needs to be fit into the designated lab space. This limits the total air spacings between the innermost and outermost layer of the shield. Given the available air gaps and the goals for magnetic shielding, we also attempted to reduce the cost and the weight of the shield as much as possible. We calculated the placement of different number of layers of shield within this space and found that a three-layer shield would be most efficient for our particular case. The details of this decision are discussed in the upcoming sections.
- The shielding layer must be mounted under as little stress as possible, both during the assembly and disassembly of the system and in the assembled configuration. This is crucial

as mu-metal, the high-permeability alloy we chose for the shielding layers, is very sensitive to stress. Stress significantly decreases the permeability of the mu-metal by destroying its grain structure. Given the size of the shield, the weight of the mu-metal sheets itself is large enough to cause irreversible decrease in permeability. Thus, the support structure of the shield is carefully designed to distribute the stress evenly on the mu-metal. As the mu-metal were initially produced in flat sheets, we chose to use a rectangular geometry for the shield, which is easier to assemble and handle the stress, despite that the spherical or cylindrical geometry would provide better theoretical shielding factor. This is a crucial lesson from the ACME I and II shields, which were initially designed in cylindrical geometry and were found to be degraded due to the stress on the cylindrical mu-metal sheets.

- The attachment of mu-metal using bolts was designed to avoid metal stress. Unlike previous designs where bolts were integrated into stainless steel parts within the mu-metal, this setup attached bolts directly to support frames, with deliberately oversized mu-metal holes to minimize contact. This arrangement required precise positioning during assembly to prevent metal contact with bolts, especially since hole tolerances varied due to some being hand-drilled.

- The shield was designed to be as readily assembled and disassembled as possible. This is critical for accessing the shielded apparatus, the maintenance of the shield, as well as the potential need to change the configuration of the shield. This is achieved by separating the shield into two independent, modular parts, one being the bottom face and the other being the upper "U" structure that encloses the apparatus. The whole shield can be easily separated into these two parts, and the internal apparatus can be accessed by removing the upper part. During this process, most of the mu-metal plates are not moved, which reduces the stress damage during the handling. In addition, All mu-metal sheets are designed to be fully removable. Under rare circumstances that any of the mu-metal sheets are damaged by stress, they could be annealed in a hydrogen furnace to recover their permeability.

- Access to the shield's interior was essential, requiring strategically placed holes to minimize magnetic field leakage while allowing necessary access. The placement and size of these holes were refined through design and simulation. An overview of the holes for the final design can be seen on Figure 4.6. The list of holes we designed for included the following which are roughly ordered by size:
  - Holes for the refinement and readout lasers on the North and South sides of the shields. These four holes are the largest holes in our shields, and are of largest concern in reducing shielding performance. After extensive study for the effect of holes on shield described in Section 4.6, we ended up with a height of $14.5\,\mathrm{cm}$ and the width about one third of its height, with the shape close to a chamfered rectangle. The vertical expansion of these holes allow us to fully cover the molecular beam with our readout and refinement lasers. While we can clip the lasers closer to the molecular beam size, this may cause Airy patterns to appear in the laser intensity profile [127]. This height was chosen based on early estimates of the molecular beam size after the electrostatic focusing, but as we develop the apparatus, we demonstrated that a collimated beam with $4.2\,\mathrm{cm}$ width ($\pm 3\sigma$) could be reliably produced, with its size smaller than we initially thought.
  - Holes on the upstream and downstream faces of the shields to allow ISO100 nipples for the ThO beam to enter and exit the shielded region. These are the second larges sets of holes, with a diameter of 10.8 cm. We later decided to use custom ISO100 nipples

with a smaller diameter pipe to increase the clearance with these holes.

- Circular holes for the STIRAP windows on the top and bottom of the chamber near the readout region, as well as the 14 equally sized 3 in. diameter auxiliary windows on the chamber that provide optical access to the beamline if needed.
- Holes to allow the light pipes to connect the collection optics to the SiPMs just outside the shields. ACME III use eight straight light pipes that each exit the chamber at a $45°$ angle. These holes are oval shaped in clearance of a tilted cylindrical light pipe with 1 inch diameter.
- Holes on the bottoms of the shields for the six support posts that the each of the shield layer frames rest on (for 1 in. diameter posts), as well as the six support posts for the magnetic field coil frame and the six support posts for the interaction region vacuum chamber (2 in. diameter posts). Because of the large numbers of the holes on the bottom surface, their collective influence on the shielding performance has been carefully studied in Section 4.6.
- Holes to insert magnetometers into the magnetometer pockets in the interaction region from the top surface and the North and South surfaces of the shields, as well as additional holes that would allow us to insert magnetometers between the shield layers. We ended up with 8 1-inch holes near the central region for on each face for the two side faces and the top face.
- Holes in the corners and in the edge covers that allow us to wind degaussing coils around the faces of the shields.
- Holes in the μ-metal so that we could attach the plates to the frames with $5/16"-18$ bolts.

  - Small holes that can be used to secure degaussing coils on the faces of the shields, located along the side of the designated degaussing coil paths. these are the smallest holes in the shields with a diameter of 0.2 in..

- The molecular path on the upstream side of the shield has been minimized, namely the distance between the electrostatic focusing lens and the location of the cleanup laser. This was a paired design constraint with the interaction region vacuum chamber. We engineered the system so that the maximum fraction of molecules being collected by the electrostatic focusing lens would enter the spin-precession volume and being used for the eEDM measurement.

- The project aimed to keep the design as symmetric as possible to simplify construction, reduce potential shield gradients, and avoid future operational confusion. However, some asymmetries were necessary due to design decisions, such as the position of the precession region and the integration of straight light pipes, which dictated the shield's length and introduced minor asymmetries in the placement of features like rotary window holes.

4.3.2 Shield design

In determining the optimal design for our magnetic shield, the primary consideration was the number of layers. The proposed shield has approximate dimensions of $1\,\mathrm{m}$, with individual layer thickness of $1.6\,\mathrm{mm}$. Based on the material properties, specifically a relative permeability of approximately 8×10^4 [141], we calculated a shielding factor (SF) of approximately 130 for a single-layer configuration. Given our stringent requirement of a $10\,\mu$G residual field, a two-layer shield was deemed insufficient. Even under ideal conditions with infinite air gaps between layers, the maximum achievable shielding factor would be in the order of $130^2 \sim 10^4$. Conversely, excessive layering was constrained by the necessity to maintain adequate air gaps between layers for effec-

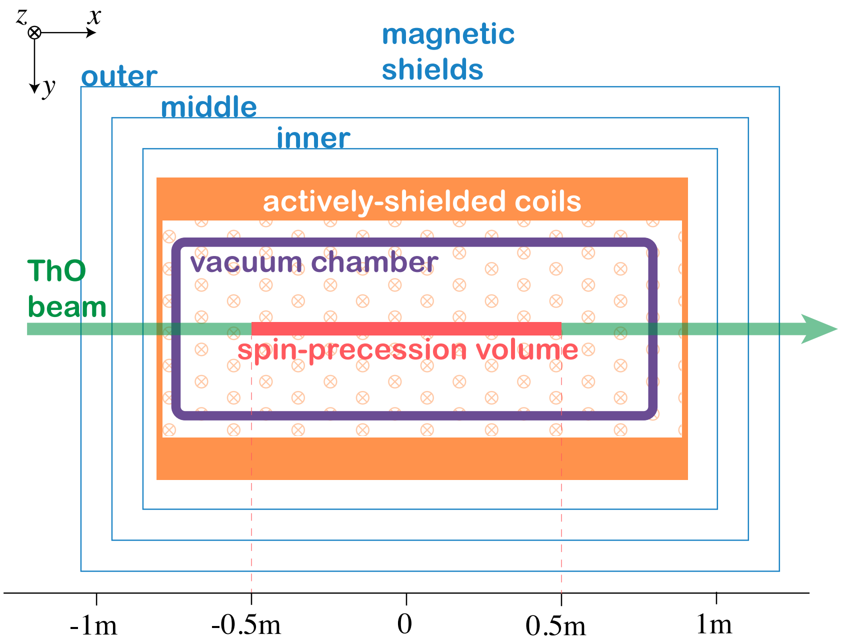

Figure 4.3: **An overview of the ACME III shield, coil, and vacuum system.** A beam of ThO molecules (green) travels though a spin-precession volume (red) inside a vacuum chamber (purple) within the actively-shielded coil (orange). Three layers of mu-metal shielding (blue) enclose all.

tive multi-layer shielding, given the fixed inner and outer dimensional constraints. Consequently, our analysis focused primarily on three- and four-layer configurations. For context, it is worth noting that the ACME I and II experiments utilized a five-layer magnetic shield design.

Figure 4.3 shows an overview of the ACME III shield and other equipments that sets the dimension limitations. Here a three-layer shield is shown, which is the final design we chose. The inner layer dimension of the shield is limited by its immediate neighbor, the coil system. To accomodate the coil and the inner layer supporting frame, the inner layer dimensions has to be at least $110\,\mathrm{cm}$ in width and $180\,\mathrm{cm}$ in length. The outer layer dimension is limited by the lab space, in which the primary concern is to have enough clearance for crane to lift the shield. This sets about $160\,\mathrm{cm}$ in height and width. Thus, the air gap between layers would at most be $12.5\,\mathrm{cm}$

for a three-layer shield, or $8.3\,\mathrm{cm}$ for a four-layer shield. Using Eq. 4.15 (because we think the longitudinal shielding would be a larger concern), we found that the four-layer shield would only have a factor of ~ 5 improvement compared with the three-layer shield, which is inefficient due to the insufficient air gap between layers.

The viability of the three-layer shield was determined by the simulation of the magnetic field inside the shield. We used finite-element method (FEM)[1] to simulate the magnetic field inside the shield, with the external field set to be the actual ambient field measured in the lab, shown in Figure 4.1. The shield was assumed to be perfectly degaussed so that its static residual field distribution was governed by the anhysteretic magnetization curve of the mu-metal, specified in [141]. This is a simplified model. In real world, the residual magnetization would be dominated by the remanence of the mu-metal [142, 143, 144], which is addressed by degaussing described in Section 4.5 in detail.

To ensure the accuracy of our simulation model, we implemented custom mesh settings tailored to the unique characteristics of our system. The combination of thin geometry and large magnetic permeability in the mu-metal domains resulted in extremely high aspect ratios, presenting a significant challenge for reliable meshing and subsequent simulation. To address this, we developed a rigorous meshing strategy optimized for these non-linear material domains.

Our approach involved a comprehensive mesh quality assurance process. We established a minimum threshold of eight mesh points across each small edge within the model. This parameter was determined through a sensitivity analysis, which demonstrated that simulation results became mesh-independent when the number of points exceeded five. This conservative approach of using eight points ensured robust and reliable results across all simulated scenarios.

For the mu-metal domains, we employed a swept meshing technique. This method originated

---

[1] COMSOL Multiphysics is used.

from the internal faces of each shielding layer and progressed continuously toward the external faces. This approach allowed for a controlled and uniform mesh distribution throughout the critical mu-metal regions, essential for capturing the complex electromagnetic behavior accurately.

The remaining air domains, which exhibited less complex geometry and material properties, were meshed using a free tetrahedral method. This approach provided an optimal balance between computational efficiency and accuracy for these less critical regions of the simulation domain.

The simulation results can be seen in Figure 4.4. With three layers of shield, this result suggests that a suppression of the DC ambient field by over 10^5 is achievable, which is sufficient for our requirement.

In the final design, ACME III magnetic shields are comprised of three nested rectangular prisms constructed from high permeability mu-metal sheets[2], each 1.6 mm thick. These structures are shaped into flat panels, allowing for a stress-minimized assembly and echoing designs used in magnetically shielded rooms. The choice of flat sheet metal offers practical benefits: these panels can be annealed in a commercial hydrogen furnace without the need for shape-maintaining jigs, and they can be transported flat to and from the annealing facility. Panels are precision-cut using a commercial waterjet, with the edges subsequently bent to a 90-degree angle for assembly. Figure 4.5 shows a clipped view of the final design of the three-layer shield.

The outermost layer of the shield measures $226.7\,\mathrm{cm} \times 157.7\,\mathrm{cm} \times 1.57.7\,\mathrm{cm}$, aligning its longest dimension with the molecular beam axis. The innermost layer is slightly smaller, at $185.7\,\mathrm{cm} \times 1.167\,\mathrm{cm} \times 1.167\,\mathrm{cm}$, with each layer spaced 10 cm apart at each direction. This configuration ensures that the edges of the panels overlap significantly, typically by about $3 \rightarrow 6\,\mathrm{cm}$, enhancing the shield's integrity and effectiveness. These overlaps are critical, especially where the shield's seams are covered with patch plates for additional security and where modifications might

---

[2] Co-Netic AA Perfection-Annealed, supplied by Magneitc Shield Corp.

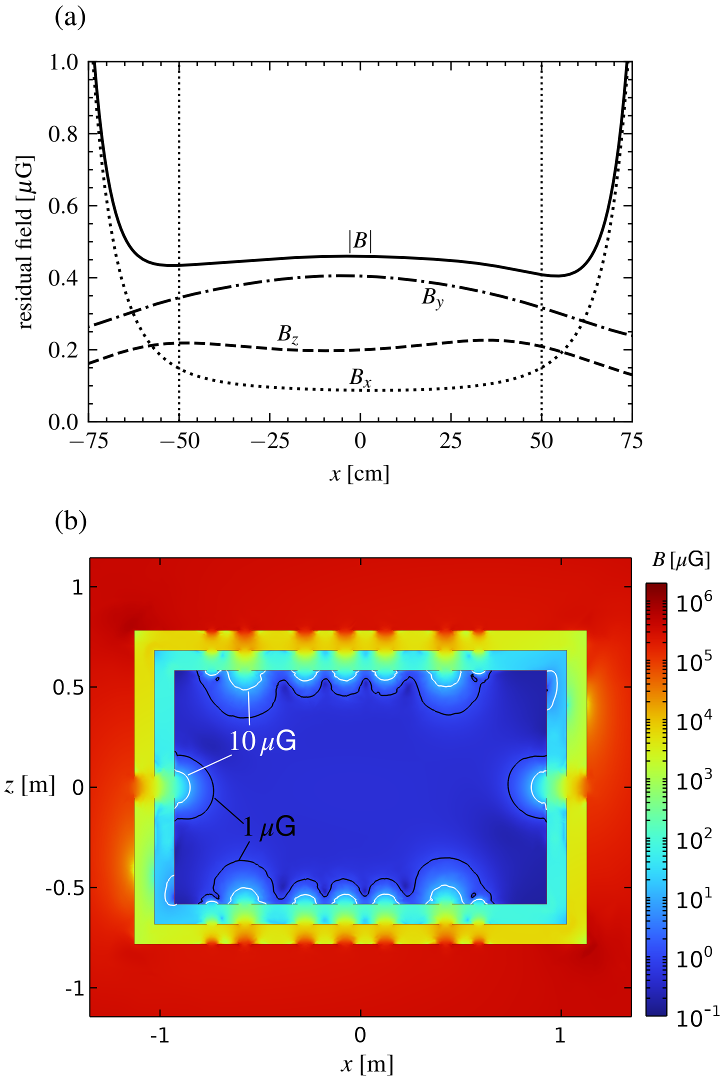

Figure 4.4: **The simulated static residual field for three-layer shields.** (a) the field components on the central axis of the shield, and (b) the field amplitude on xz plane. The mu-metal sheets are assumed to be perfectly degaussed and the external field is set to be the ambient field in the lab.

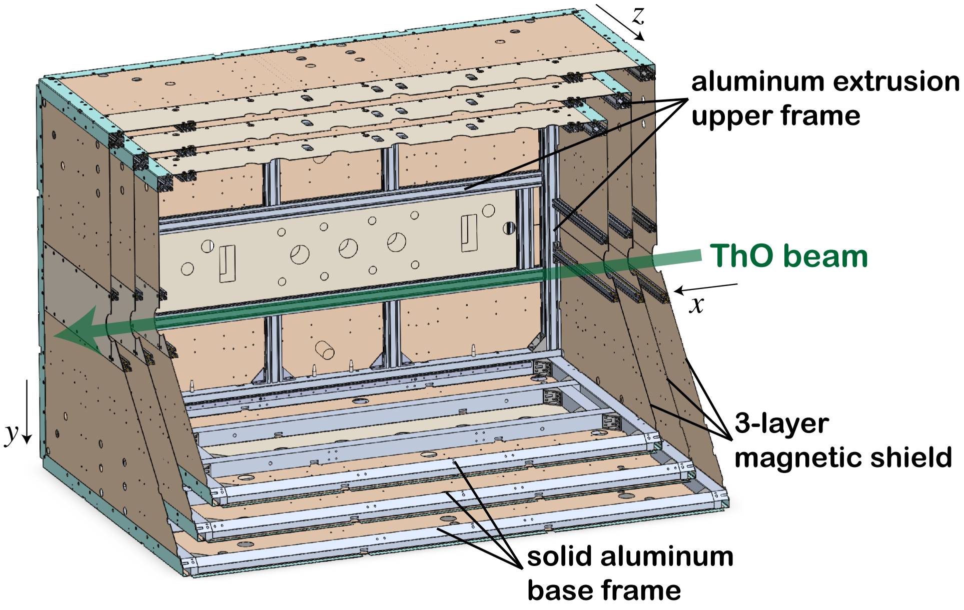

Figure 4.5: **Clipped view of the three-layer shield, to scale.** The inner layer dimension is $185.7\,\mathrm{cm} \times 1.167\,\mathrm{cm} \times 1.167\,\mathrm{cm}$, with its longer dimension oriented to align with the molecular beam pathway of the ACME experiment.

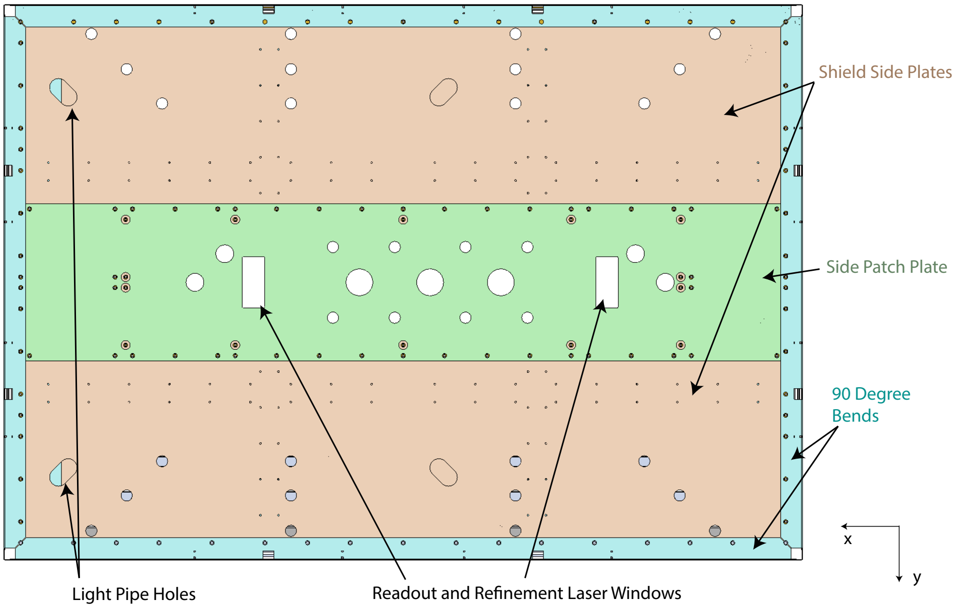

Figure 4.6: **Panels on one face of ACME III magnetic shield.** Side faces are shown. The side plates (beige) are first mounted to the frame, then the seam between the two plates is covered by the patch plate (green). Each of the edge is covered by a 90° bent edge cover (cyan). The holes for various purposes are also shown.

be necessary, allowing for easier re-annealing and machining.

The mu-metal panels are mounted onto an innovative aluminum frame design, consisting of an upper "U"-shaped frame connected to a flat base, shown in Figure 4.7. The frames are constructed from $60\,\mathrm{mm}$ Minitec T-slotted aluminum profiles, optimized for rigidity and incorporating an "L"-shaped profile. This configuration facilitates the routing of degaussing cables around the frame's edges. The base frame, composed of solid aluminum bars, provides stability and is supported by six 1-inch aluminum posts secured to the ACME table. Each layer's frame is independently mounted, allowing for straightforward disassembly and maintenance.

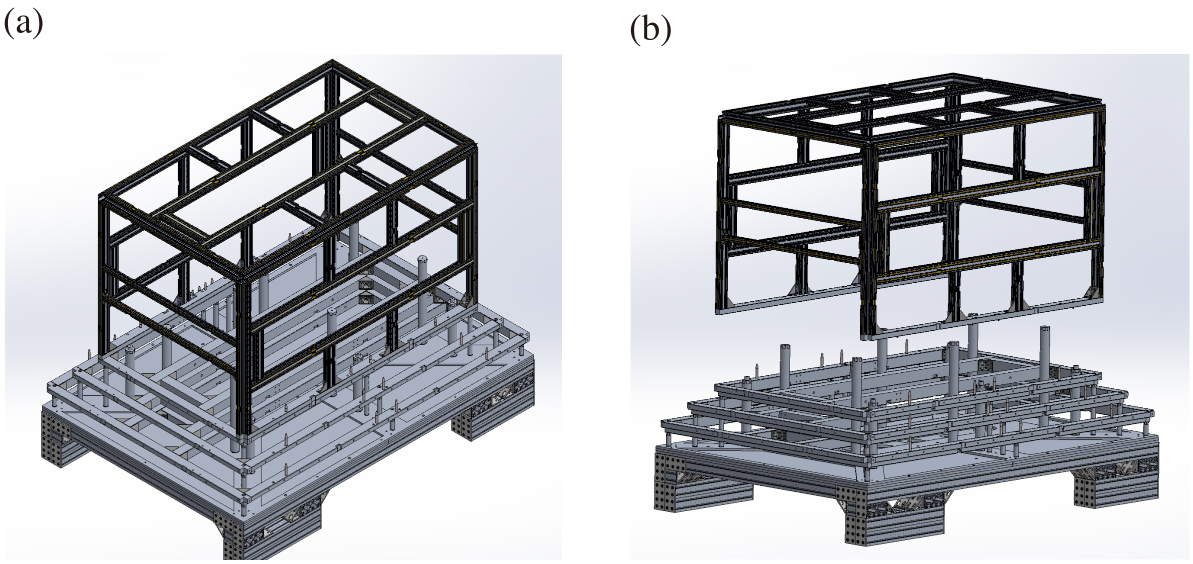

Figure 4.7: **Magnetic shield frames.** The upper "U" frame is constructed from Minitec T-slotted aluminum profiles, while the base frame is made from solid aluminum bars. The frames are designed to split easily (b), enabling quick access to the interior for installation or maintenance.

The frames are designed to split as easily as possible, enabling quick access to the interior for installation or maintenance. This modular design allows the upper frames to be lifted off by a crane, minimizing the disturbance to the mu-metal panels. We built a crane to handle these frames without contacting the mu-metal, ensuring the integrity of the shielding.

Assembly of the mu-metal sheets involves clamping them between the aluminum frame and external washers, with overlapping regions double-layered to ensure a secure and smooth joint. These connections are reinforced with brass or titanium bolts, depending on the layer, to maintain non-magnetic properties, especially in the innermost layers. Bolts are torqued to an optimal level to prevent over-tightening and potential stress on the panels. The design and dimensioning of the shields by our research group were supported by extensive simulations to optimize the hole configurations and overall geometry for maximum shielding effectiveness.

4.3.3 Shield construction

The design and construction of the ACME III magnetic shields were significant undertakings that spanned approximately one year. This project involved collaborative efforts from Gabrielse Group including Bingjie Hao, Cole Meisenhelder, Daniel Lascar, and contributions from other group members. This section provides a detailed account of the methodologies employed, challenges encountered, and solutions implemented during the construction of these complex magnetic shields.

The initial phase of construction involved the precision cutting of mu-metal sheets by Chicago Waterjet Inc. These sheets were tailored to our specifications, with all the designed mounting holes and access ports precisely cut. The edge cover pieces were cut and bent at 90 degrees with a 1.6 mm radius by Ultratech Inc., facilitating smooth contact between the flat pieces on each surface and the 90-degree bridge pieces. Concurrently, frames to support the mu-metal sheets were constructed using solid aluminum for the base and mini-tec extrusions for the upper "U" frame. This robust design was critical to support the weight of the large mu-metal sheets, each weighing between 50-60 kg and 3 pieces on each surface on average. Two personnel carefully handled these sheets to avoid any stress that could compromise their structural integrity. The mu-metal sheets were attached to the frames using screws, with torque controlled to approximately 3.3 N-m using torque wrenches. This specific torque setting was chosen to replicate hand press pressure, reducing the risk of stress induction through overtightening. Screw holes were designed with loose clearances to prevent direct contact with the mu-metal, therby ensuring the elimination of any localized stress.

During the assembly process, it became evident that distributing the weight of the mu-metal sheets over a larger number of screws was crucial to prevent localized stress. Consequently, additional mounting holes were drilled by hand to accommodate more bolts, resulting in a more uniform distribution of the sheets on the frame. This modification involved drilling approximately 1500 holes across all three layers of the shield, creating a pattern of holes spaced 6-8 inches apart. This labor-intensive process involved the collaborative effort of all group members. This phase also addressed misalignment issues between assembled parts and provided valuable experience in sheet handling for the team.

Following the initial assembly and modifications, a re-annealing process was planned to restore the grain structure of the mu-metal that may have been compromised during drilling, machining, and handling, with the aim of improving its magnetic properties. Initial attempts to anneal prototypical pieces in the laboratory furnace yielded promising results with high permeabilities. However, the design requirements favored larger continuous pieces to enhance magnetic flux continuity across the shield. This led to the decision to engage a professional metal treating company with large furnace capacities and established annealing protocols for magnetic alloys. Exotic Metal Treating in Indianapolis, IN, was selected to perform the annealing using their proprietary heat-treatment process. The mu-metal sheets were removed from the initial assembly, cleaned, packed, and we transported them in a rented truck for professional re-annealing. This process extended over several months, culminating in the reinstallation of the annealed sheets. The final assembly of the magnetic shields was completed in October 2021.

4.4 Characterization of mu-metals

The permeability of mu-metal is critical for magnetic shielding. For a three-layer shield, Eq. 4.12 suggest a rough dependence of SF $\propto \mu_r^3$, which is crucial to the shield performance. Rather than being a linear material whose relative permeability is constant, mu-metal are ferromagnetic materials that exhibit a strong dependence of permeability on the magnetic field strength and the magnetization history. The Magnetic Shield Corp. provided the hysteresis specification of Co-Netic AA, with the saturation magnetization of roughly 0.7 T, coercivity of 0.6 A/m, remanence of 0.38 T, initial permeability of roughly 80000, and the maximum permeability of about 500000. Similar parameters for are reported by an independent research group at CERN [145] for annealed Co-Netic AA, while they found that an unannealed Co-Netic AA has a much lower initial permeability of 6000 and a peak permeability of 14000. Thus, the annealing process is crucial to the performance of the mu-metal.

4.4.1 Annealing

The physical reason for the remarkable high permeability of ferromagnetic materials are their unique magnetic domain structure, which allows the material to be magnetized with minuscale magnetic fields. Magnetic domains are small regions of a material in which the magnetic moments of the atoms are aligned in a common direction, a effect that is favorable for the material to have lower energy due to the exchange interaction between the magnetic moments between the atoms. On the other hand, magnetic domains have their own magnetostatic energy which is proportional with its volume, so the formation of magnetic domains is a competition between the exchange interaction and magnetostatic energy, resulting in typical domain sizes of $1-100\,\mu$m. For the bulk material, the magnetic domains are randomly oriented, leaving the material unmagnetized.

The interfaces between regions in which the magnetization has different directions are called domain walls, which also have finite width of typically $100\,\mathrm{nm}$. The visualization and resolution of these magnetic domain structures can be achieved through Magneto-Optical Kerr Microscopy [146] or some modern anisotropic imaging techniques [147]. For a metal alloy, the inner structure of a metal is made up of individual crystalline areas known as 'grains'. The structure, size and orientation of these grains result from the material composition (alloy) and the way the material is made (e.g. forging, casting or additive manufacturing). The grains are formed within the molten material when it solidifies, interact with one another and with other ingredients, like phases and contaminations. Typically, the grain size ranges from $1 - 100\,\mu\mathrm{m}$ as well. They are important for various properties of the material, including the mechanical strength, surface smoothness, corrosion resistance, etc. Its formation is an independent process with magnetic domains, but the interplay between the size of grains and magnetic domains plays a crucial role in the magnetic properties of the material.

The magnetic behavior of ferrimagnetic materials can be classified based on grain size into four distinct categories [148]:

- Superparamagnetic (SPM): At extremely small grain sizes, particles display superparamagnetism where thermal fluctuations dominate, causing the magnetization to randomly flip, resulting in zero net magnetization without an external magnetic field.
- Single Domain (SD): Below a critical grain size, grains contain just a single magnetic domain. These grains are uniformly magnetized and exhibit high coercivity because changing their magnetization requires overcoming significant anisotropic energy barriers.
- Pseudo-Single Domain (PSD): Slightly larger grains may exhibit characteristics of both single and multidomain structures, showing higher remanence like SD grains but lower coer-

civity typical of MD grains.

- Multidomain (MD): Larger grains generally contain multiple domains. The presence of multiple domains allows for easier domain wall movements, which reduce the material's coercivity.

These categories are not strict, but rather a continuum of magnetic behavior that depends on the grain size and the material composition. In a MD material, the magnetization process corresponds to the movement domain walls - the magnetic domains that aligns with the external field expands until the entire material's magnetization aligns with the external field, which is the saturation magnetization. This process requires little energy, thus the material exhibits a high permeability because low field is required to achieve a high magnetization. The irreversible magnetization that causes hysteresis in this case is primarily due to the pinning of the domain walls at the defect sites in the material, which is also relatively small, and can be further reduced by reducing the impurities in the material, resulting in low coercivity. Thus, mu-metal in MD state is favorable for magnetic shielding applications, both for its high permeability and low coercivity.

However, the grain structure may be broken through many processes including cold work, improper heat treatment, and mechanical stress, leading the material to the SD state. In this case, each grain contains exactly one magnetic domain, and the magnetization process could only be achieved by rotating the magnetization of each domain to the direction of external field, a much more energy-consuming process. This results in a low permeability and high coercivity. As can be seen in Figure 4.8 [148], the MD magnetization curve is steeper than SD curves and have smaller coercivity.

The annealing process is known for its ability to recover the grain structure of the material, reverting to MD state, and remove the impurities that cause the pinning of the domain walls, which

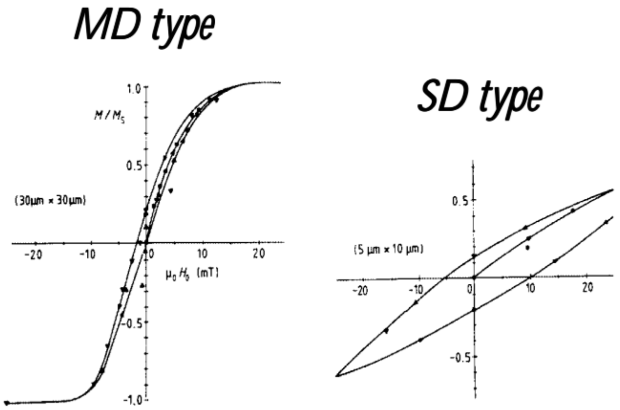

after Dunlop (1990)

Figure 4.8: **Comparison of typical B-H curves of MD and SD materials.** Taken from [148].

becomes an essential step in the production of mu-metal, as well as a recovery method if any stress, cold work, or improper heating is applied to the mu-metal.

Annealing mu-metal involves a series of carefully controlled heating and cooling steps to optimize its magnetic properties by realigning its crystal structure and reducing internal stresses. This procedure typically includes ramping temperatures, soaking times, and controlled cooling phases. While Magnetic Shield Corp. has a proprietary annealing process that has fine-tuned parameters, we followed their general guideline for this process and studied extensively in our lab at Northwestern.

The atmosphere for annealing mu-metal was chosen to be hydrogen, as the pure reducing environment optimizes the efficiency for removal of impurities and oxides from the material. The mu-metal sheets were annealed at Exotic Metal Treating in coorporation with Magnetic Shield Corp, using their proprietary annealing process. The rebuild of the grain structure can be easily seen in the comparison in Figure 4.9 [149]. The details of this process is not disclosed but roughly follows the publicly available guideline [150] discussed above. After receiving the annealed mu-metal sheets and sample toroidals in the same run of annealing, we measured the magnetic properties in our lab to confirm the performance. In the annealing furnace, the mu-metal undergoes the following procedure:

- The furnace was ramped up to 1100°C in 90 minutes and soaked for about 5 minutes, then further ramped up to 1180°C at a rate of 5 °C per minute. This slow increase in temperature is important to avoid thermal shock and uneven expansion. 1180°C is significant because it is above the recrystallization temperature but below the melting point of the alloy. At this temperature, the mobility of the atoms in the crystal lattice is sufficient to facilitate a transformation in the grain structure.
- The mu-metal was held at 1180°C for an extended period of 3.5 hours, allowing for thorough recrystallization across the entire material.
- Cool down to 500°C at a rate of 2 °C per minute, then further cool down to room temperature at a rate of 4°C per minute. Slow cooling to 500°C defines the effectiveness of the annealing because it is in the active period to form grain structures, this gradual reduction in temperature helps in locking the grains in their ideal orientation and size, which are aligned for optimal magnetic permeability. Once the temperature reaches 500°C, the cooling rate is increased to 4°C per minute. The reason for accelerating the cooling at this stage is that the most critical transformations and realignments within the alloy have already taken place. The structure becomes more robust and less sensitive to changes due to temperature variations.

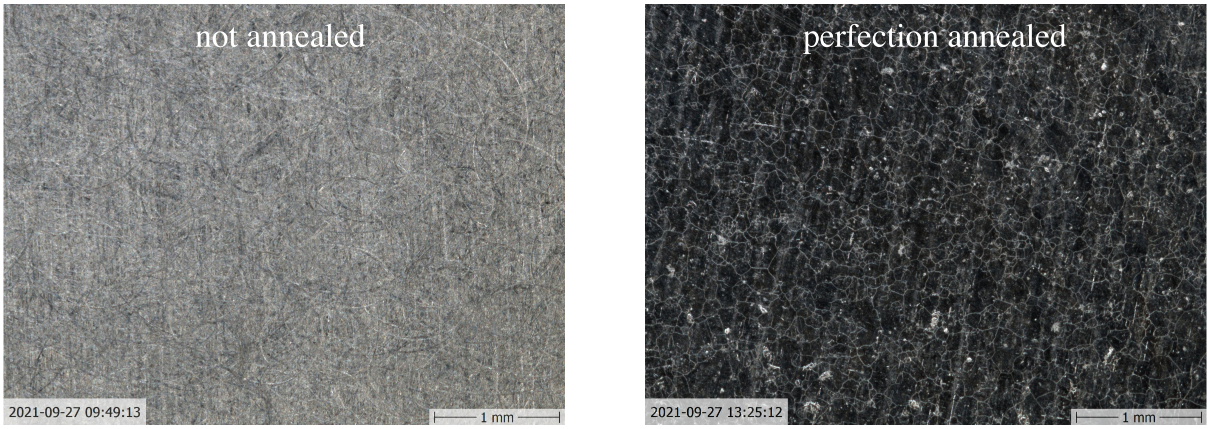

Figure 4.9: **Comparison of the Co-Netic AA mu-metal sheets before (left) and after annealing (right).** The grain boundaries on the annealed piece can be barely seen, with the size of $\sim 100\mu$m.referenced from [149].

4.4.2 Measurement of magnetic properties

We measured the magnetic properties of the mu-metal in two configurations: the standard toroidal samples and the in-situ measurement on the shield. The toroidal sample measurements provides accurate understanding of the magnetization and hysteresis characteristics of the mu-metal with a specific annealing run, while the in-situ measurement is targeted to have monitor the permeability change of the mu-metal that is on the shield, which is less accurate due to the complex shield structure, but more relevant to the actual application.

The toroidal measurement comprised a toroidal sample, an excitation coil, and a pickup coil. The sample was precision-cut from a 1.6mm thick mu-metal sheet with a waterjet. It has an outer diameter of 6 cm and an inner diameter of 5 cm, dimensions that were selected to minimize the variation in flux path lengths across the sample. This geometric configuration ensures that the magnetic field inside the sample is uniform during the measurement, and the average diameter of the toroid effectively represents the length of the magnetic flux paths.

The measurement technique involved generating a magnetic field (H field) within the sample by applying a current to the excitation coil. The strength of the H field is directly proportional to the current applied, as suggested by the Ampere's law:

$$\oint_{\partial\Sigma} \mathbf{H} \cdot \mathrm{d}\boldsymbol{\ell} = \iint_{\Sigma} \mathbf{J} \cdot \mathrm{d}\mathbf{S} \tag{4.16}$$

The response of the material to the applied magnetic field was detected using a pickup coil. The voltage induced in this coil is proportional to the time derivative of the total magnetic flux threading the sample, as suggested by

$$\oint_{\partial\Sigma} \mathbf{E} \cdot \mathrm{d}\boldsymbol{\ell} = -\frac{\mathrm{d}}{\mathrm{d}t} \iint_{\Sigma} \mathbf{B} \cdot \mathrm{d}\mathbf{S} \tag{4.17}$$

By integrating this voltage signal, the magnetic flux density (B field) was determined. This integral was performed numerically, allowing further analysis and processing of the data. Prior to measurements, the toroidal sample was subjected to a careful degaussing process using the excitation coil to remove residual magnetism.

For the actual measurement, a linear ramp of current was applied to the excitation coil and increased for 10 minutes, from $H = 0$ to approximately $H = 30$ A/m. The induced voltage in the pickup coil was continuously monitored, passed through a 160 Hz low-pass filter to eliminate high-frequency noise, and then read using an Analog-to-Digital Converter (ADC). The filtered voltage signal was then numerically integrated to compute the corresponding B field.

In analyzing the magnetization curves presented in Figure 4.10, we observe a distinct variation in magnetic properties across different samples, specifically focusing on their permeability and saturation magnetization. The permeability of these samples are B/H, just the slope of the curve. The specifications from Magnetic Shield Corp, depicted in dark red on the graph, exhibits permeability higher than all the tested samples. Its initial permeability is approximately 80,000, peak permeability near 500,000 at an H field of about 1 A/m, and a saturation magnetization reaching around 0.7 T.

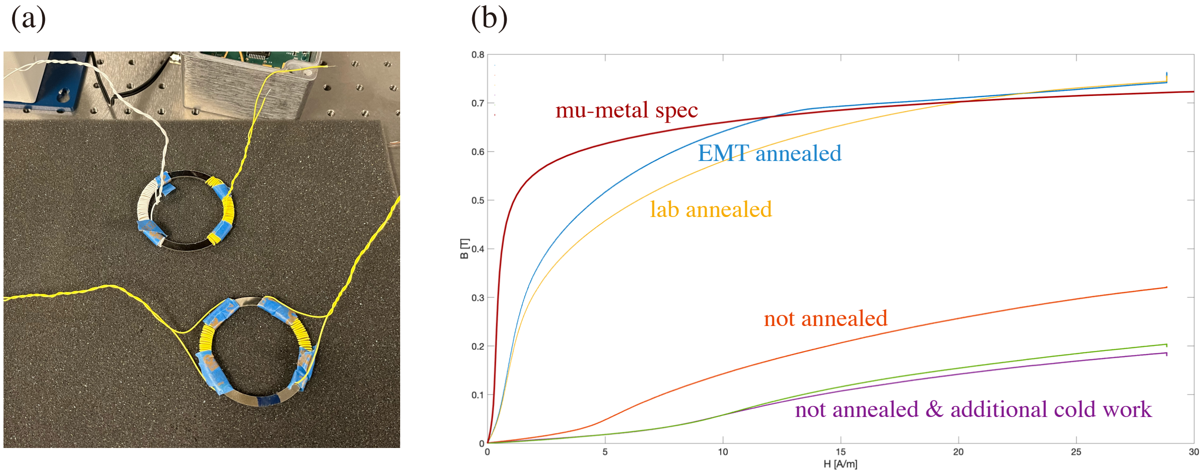

Figure 4.10: **Measured magnetization on toroidal mu-metal samples.** (a) The measurement setup of the samples, with the excitation coil and the pickup coil. (b) The magnetization curve B vs. H for various samples.

Conversely, the annealed samples, represented in yellow (lab annealed) and blue (annealed by Exotic Metal Treating), display magnetization behavior that, while similar to each other, is markedly inferior to the company-provided specs. Both samples exhibit an initial permeability of about 30,000 and a peak permeability of approximately 150,000, approximately one-third of the values recorded for the Magnetic Shield Corp spec. This discrepancy could be due to a variety of factors, including potential deviations in the annealing process, such as temperature inconsistencies, duration of annealing, or the cooling rate, which may not have been optimally aligned with the requirements for achieving higher permeability. Additionally, improper handling or the introduction of unnoticed stresses during the measurement process could also contribute to these lower permeability values. Notably, the sample treated by Exotic Metal Treating shows slightly higher permeability than the lab-annealed sample, suggesting a more effective annealing procedure that is proprietary from the company.

Moreover, samples that have not undergone annealing exhibit significantly reduced permeability, which aligns with measurements conducted in [145] and theoretical expectations. This reduction is anticipated as the lack of annealing leaves the material with residual stresses and disordered grain structures, which are detrimental to magnetic performance. Furthermore, samples subjected to additional cold working processes demonstrate even lower permeability, a result that is consistent with the introduction of further mechanical stresses and increased dislocation density, which disrupt the grain structure and reduce the overall magnetic permeability.

For the in-situ measurement of magnetic properties on shield, the fundamental approach remains consistent with traditional methods: applying an H field via an excitation coil and monitoring the B field with a pickup coil. However, the complexity of the shield's geometry and the presence of multiple layers necessitated a more sophisticated measurement setup. We tried several methods to conduct the measurement, and ended up utilizing the degaussing system, which will be described in Section 4.5.

A rectangular shield consists of 6 faces. If one spacial coordinate is depicted, there are 4 faces that are parallel to the coordinate. These four faces effectively forms a loop for magnetic flux. Briefly, the degaussing system incorporates 12 degaussing coils per loop. In our setup, these coils are configured as excitation coils to uniformly distribute the magnetic field throughout the loop. A separate pickup coil was wrapped around the mu-metal sheet with the same orientation as excitation coils, through two spare holes on the shield, tasked with detecting the resultant magnetic field. This configuration mitigates the risk of flux leakage a concern given the complex structure of the shield.

Figure 4.11 shows the B-H curves measured in-situ on the shield. This data was collected on

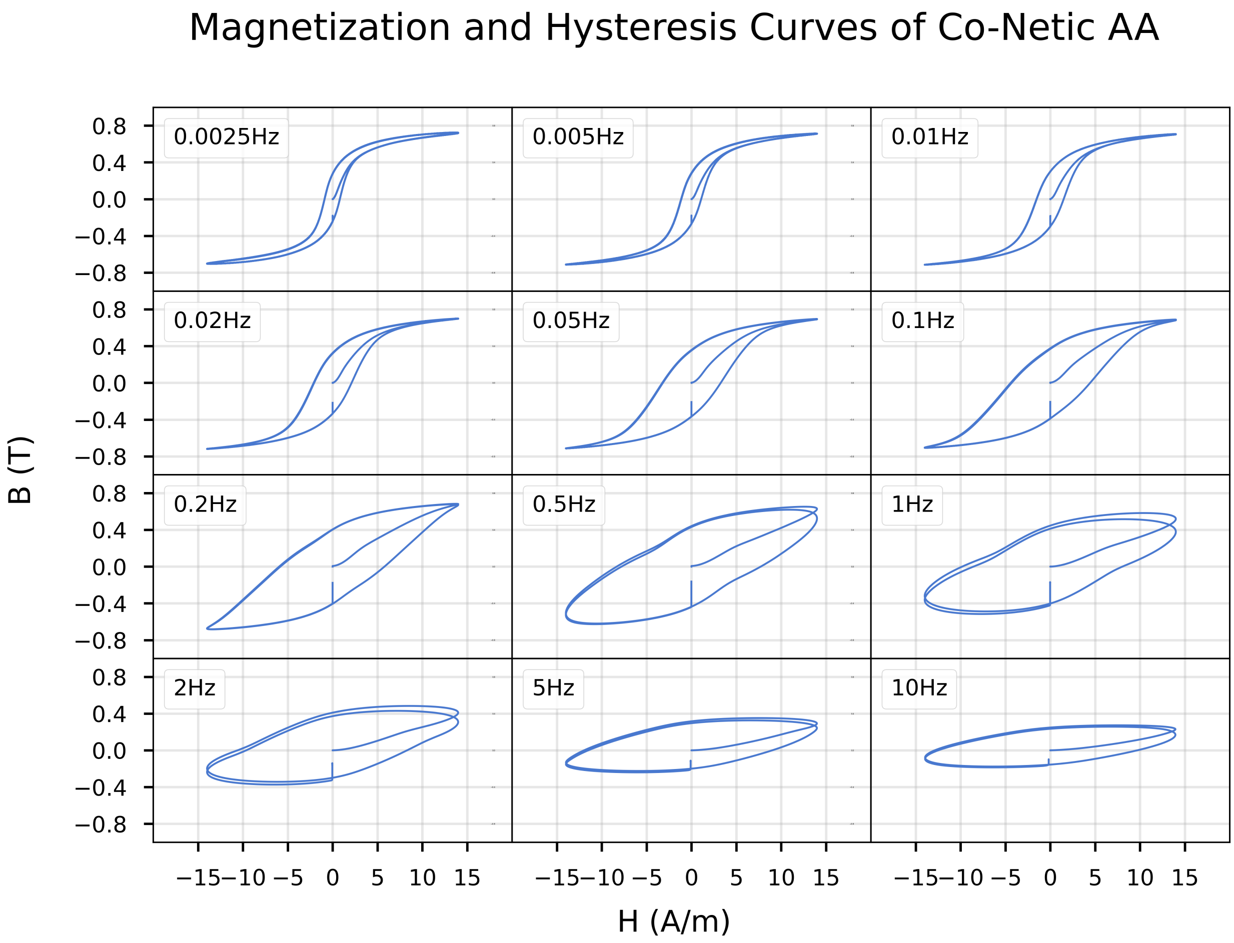

Figure 4.11: **In-situ measurements of B-H curves on the shield.** Inner layer x direction is shown.

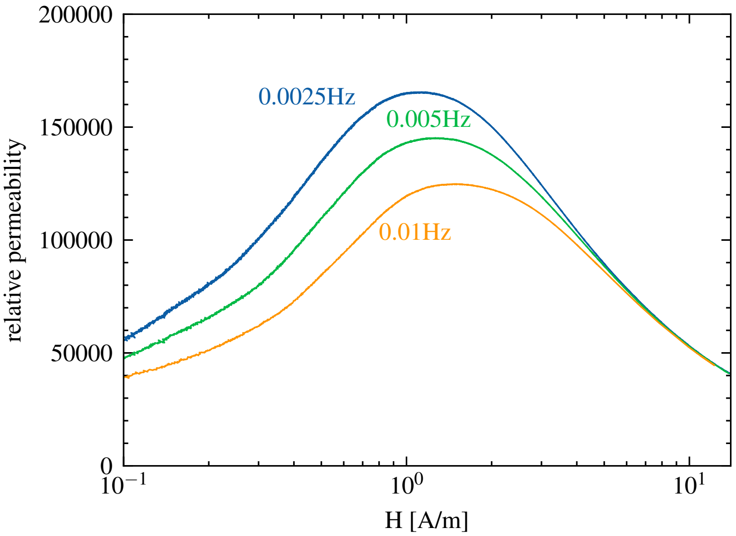

Figure 4.12: **The permeability of the in-situ measurement.** Data shown are the magnetization part of three lowest frequencies in Figure 4.11.

the inner layer of constructed shield, with x flux loop direction. The excitation coil was driven by a sinusoidal wave that is exactly two cycles long at the specified frequency, after the flux loop has been degaussed completely. The first quarter of a cycle could be regarded as the magnetization process. A strong dependence on over frequencies can be seen. As the frequency goes higher, mu-metal tends to have lower permeability, larger coercivity, and lower saturation magnetization. This is partly explained by the eddy current effect, in which current is induced in the conductive mu-metal and in turn generates a magnetic field that opposes the external field. Another reason is that increasing the frequency reduces the time available for the magnetic domains to align with the external field, which is effectively the same as reducing the size of the grain structure, leading to a transition to single-domain states. During the initial magnetization, the relative permeability of the mu-metal for the three lowest frequency can be seen in Figure 4.12. An initial permeability of about 60000 and a peak permeability of about 170000 is observed, which decreases with frequency.

Figure 4.12 illustrates a fundamental characteristic of ferromagnetic magnetizations: permeability in these materials is not constant but varies with the magnitude of the applied external magnetic field. Initially, as the external field is small, the permeability of the material increases. Under low field conditions, the predominant mechanism of magnetization is due to the motion of domain walls. As the external magnetic field intensifies, the behavior of the material evolves; the rotation of magnetic domain orientations becomes increasingly significant in the magnetization process.

The initial stages of magnetization are characterized by their reversibility this phase shows no hysteresis, indicating that the domain wall movements are mostly elastic and can return to their original state without energy loss. However, as the magnetic field continues to increase, the permeability reaches a peak and then saturates [151]. This saturation marks a transition to predominantly irreversible magnetization processes, such as the rotation of domains and the overcoming of domain wall pinning at material defects. These actions require energy to move the domain walls past obstacles within the crystal structure, which manifests as hysteresis in the magnetization curve.

For a more comprehensive understanding of these phenomena, D. C. Jiles and D. L. Atherton developed a phenomenological theory of the magnetization process in ferromagnetic materials [152, 153, 154]. From this theoretical framework, it is elucidated that the ratio of maximum permeability to initial permeability serves as an indicator of the degree of magnetization reversibility within the material. This ratio highlights the extent to which the magnetization process can occur without energy loss, reflecting the efficiency of domain wall movements and domain rotations under varying magnetic field strengths.

Typically, the peak permeability of such materials can be 4-5 times greater than their initial permeability. In the application of magnetic shielding, the initial permeability is applied in most cases, with the only exception of the outermost layer in the shielding system in a strong ambient field environment. We can utilize the larger permeability of mu-metal at stronger fields through a technique called "magnetic shaking" to enhance shielding effectiveness, particularly in environments with low magnetic fields. This method involves the application of a periodic, small-amplitude H field to the shielding material. The applied field lets the mu-metal to experience an effectively higher field, thereby exhibiting increased permeability. Crucially, the amplitude of the applied field is sufficiently small such that it does not significantly leak out from the mu-metal, ensuring that the internal magnetic environment remains unaffected. Several studies have demonstrated that magnetic shaking can amplify the shielding factor by a factor of 3-5 [155, 156]. In the ACME III shield, the degaussing system are capable of performing magnetic shaking. However, during the optimization process, we discovered that our degaussing technique achieved the design goals of $10\,\mu$G for residual fields and $1\,\mu$G/cm for field gradients without active magnetization shaking. Given this satisfactory performance, we made the strategic decision to forgo the implementation of the magnetic shaking technique. This choice was influenced by concerns about potential disruptions to the EDM data acquisition from the shaking signal, as we wanted to avoid investing significant time in rigorously testing a system that appeared unnecessary for meeting our current specifications. Nevertheless, the shield hardware retains the capability for magnetic shaking, preserving the option to implement this technique in future iterations or experiments if the need arises.

4.5 Degaussing

4.5.1 The degaussing system

High-permeability ferromagnetic alloys, such as the mu-metal used in the ACME II and III experiments, retain a degree of remanence after exposure to an external magnetic field. This remanence would be significant even if the external field is as small as earth's field. This remanence will propagate into the interior region of the shield and introduce signifiacnt additional residual fields.

Thus, degaussing serves as a critical technique to minimize this remnant field [151, 142, 143]. It achieves this by randomizing the magnetic domains within the mu-metal, effectively reducing the residual magnetic footprint of previous field exposures.

In ACME II, a 2-second degaussing pulse was applied each time the magnetic field was reversed every 30 s [100]. This consumed about 6% of the possible measurement time. After repeated field reversals, unfortunately, a significant remnant field of approximately $300\,\mu$G accumulated, substantially higher than the $10\,\mu$G threshold we set for ACME III operations. Even with extended degaussing efforts, a residual non-reversing field of about $200\,\mu$G persisted, highlighting the need for an improved degaussing strategy in subsequent experiments.

For the large rectangular shield of ACME III, 108 degaussing coils were employed. For each of the four face 'flux loop' that is parallel to a certain axis, as described in 4.4.2, the degaussing system incorporates 12 degaussing coils that wrapped closely on the mu-metal sheets and are distributed evenly around the loop. This setup is repeated on all 3 flux loops for each layer, and for all 3 layers of the shield. Figure 4.13 (a) shows the degaussing system layout for one face of the shield. On each direction, there are two degaussing coils on each face and one degaussing coil on every edge of the shield. They fit into the slots on the shield that allows the easy install and removal of these degaussing coils. This configuration ensures the uniformity of the applied degaussing field across the shield's surfaces, and is expected to be effective for removing the remanence of the mu-metal on every spot of the mu-metal layers [144].

The 108 degaussing coils are crafted from a 10-conductor ribbon cable (AWG24, 2.54 mm pitch) and connected via JST S20B-PUDSS-1 connectors. The ribbon cable is wrapped around the mu-metal sheet, and its end is connected to a non-magnetic custom-designed PCB that connects back to itself, but with 1 displacement of the conductors, thus each individual conductors are connected in series and form a 10-turn loop. The 12 degaussing coils on each direction are

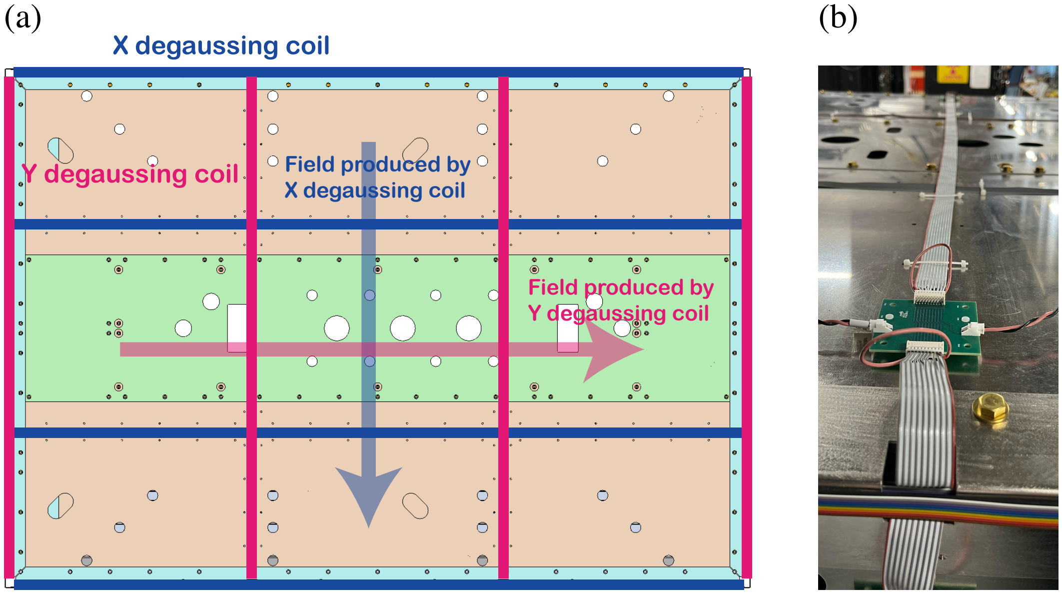

Figure 4.13: **The degaussing system for one face of the shield.** (a) On each direction, there are two degaussing coils on each face and one degaussing coil on every edge of the shield. The designated degaussing field generated by these coils are also depicted. (b) The actual design of individual degaussing coils. A 10-turn ribbon cable is wrapped around the mu-metal sheet and connect back to it self through a custom PCB that forms a 10-turn loop.

connected in series, and the series of 12 coils are connected to three current sources (Kepco BOP 100-1M) to supply degaussing current on x, y and z direction loops. A relay board (Numato Lab 32ETHRL001) is used to switch different layers of shield the degaussing current is supplied to, thus controlling the degaussing sequence.

4.5.2 Waveforms for degaussing

The effectiveness of the degaussing process heavily relies on the waveform of the current pulse applied through the coils. The chosen waveform,

$$I(t) = I_0 \frac{t}{T} \exp\left(-\frac{t-T}{T}\right) \sin\left(2\pi f t\right). \tag{4.18}$$

Is a combination of a sinusoidal wave at frequency f, an exponential decay with the time constant T, and a linear ramp to avoid abrupt changes on the supplied current, given the large inductance of the degaussing coils. The current sources are controlled by voltage from a 16-bit DAC (NI 9264) at time steps of 0.05 ms and send its output to the degaussing coils through a 300 Hz low-pass filter. Figure 4.14 (a) shows the 4 second pulse we used most often, deduced from the voltage drop measured across a $1.0044\,\Omega$ shunt resistor. This shape is realized using $f = 4$ Hz and $T = 0.4$ s for the first 3.95 s, after which the supply current is set to zero. The amplitude at $t = 3.95$ s corresponds to a current amplitude of 0.5 mA, or $H \approx 0.01$ A/m, which is much less than the threshould to create any hysteresis effect. Thus, the "abrupt change" of setting the waveform to zero at this amplitude does not creat residual magnetism. The peak current, $I_0 = 1$A, would produces a magnetic field of about $H \approx 20$ A/m that is much larger than the saturation value $H \approx 10$ A/m [145].

The B-H curve of the degaussing process was monitored using the in-situ measurement system shown in Figure 4.14 (b). The area within the B vs. H contours reduces as H is slowly reduced.

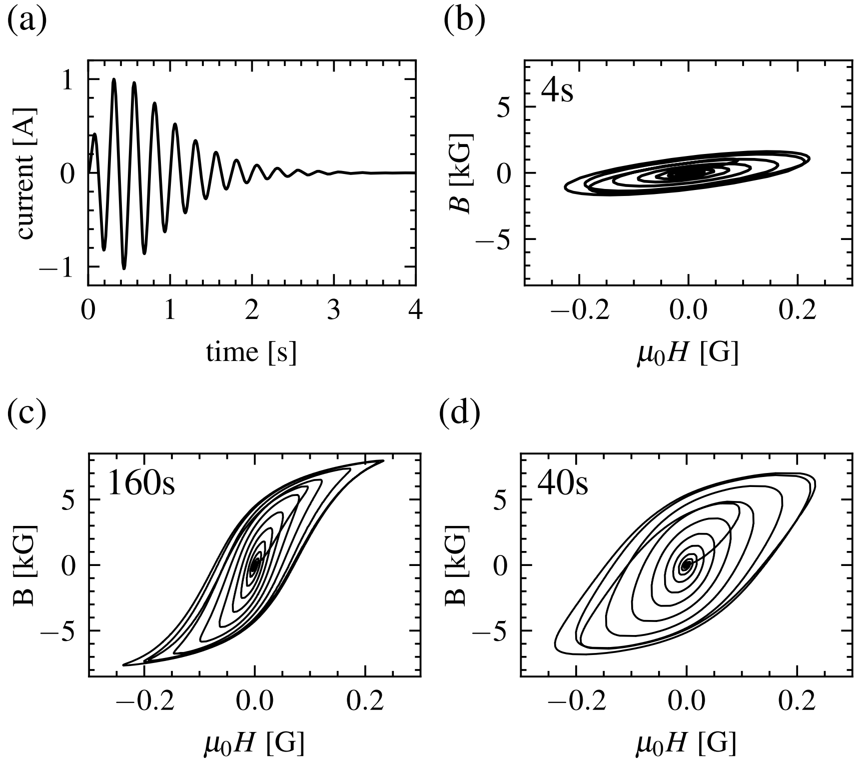

Figure 4.14: **The degaussing waveform.** The most-often used 4 second degaussing current pulse (a) and the resulting magnetic field within the mu-metal measured in-situ (b). Expanding the pulse time scale to 160 s (c) and 40 s (d) produce B vs. H curves that show more clearly the onset of saturation within the shields.

Although the saturation is not observed at this frequency, we observed a similar degaussing outcome compared with longer degaussing pulses where saturation is more clearly observed, shown in 4.14 (c) and (d). The longer pulses have exactly same shape as the 4 second pulse, but the time scale was expanded to 160 s and 40 s, respectively. These degaussing pluses result in residual field in the spin-precession volume of less than $10\,\mu$G, while decreasing the waveform duration further to 2 s would produce larger residual fields of above $20\,\mu$G. We chose to operate the degaussing system with the 4 second pulse, as it provides the best eEDM measurement duty cycle without compromising the residual field. The supply current offset must be carefully zeroed. Figure 4.15 shows the measured residual magnetism after degaussing. We observed a distinct "cubic" shaped residual field along the B_z component after degaussing with an offset in the inner layer Y direction. This effect was larger for B_z compared to B_y, while the influence on B_x was minimal due to the elongation of the shields in the x coordinate. Similarly, degaussing with an offset in the inner layer z direction revealed a prominent residual field in B_y, with a lesser effect on B_z.

A critical observation from our studies is that the magnetization offsets introduced during the degaussing process produces a much larger effect on residual fields compared to offsets applied after degaussing, as shown in Figure 4.15. The reversibility of these offset-induced residual fields are also distinctly different. We found that the induced field from a standalone DC offset current is reversible - it vanishes if the applied offset is removed. In contrast, similar offsets during degaussing led to mostly irreversible residual fields (see difference between red and purple curves in Figure 4.15), and is in the opposite direction. This suggests that these residual fields stem from the remanence in the mu-metal sheets rather than from the degaussing coils themselves, supporting the insights from [151]. The critical phase appears to be during the irreversible magnetization region of degaussing, where the field strength is about 0.3-0.7 times the saturation magnetization. Imperfections during this phase can lead to significant remnant magnetizations that are not mitigatable

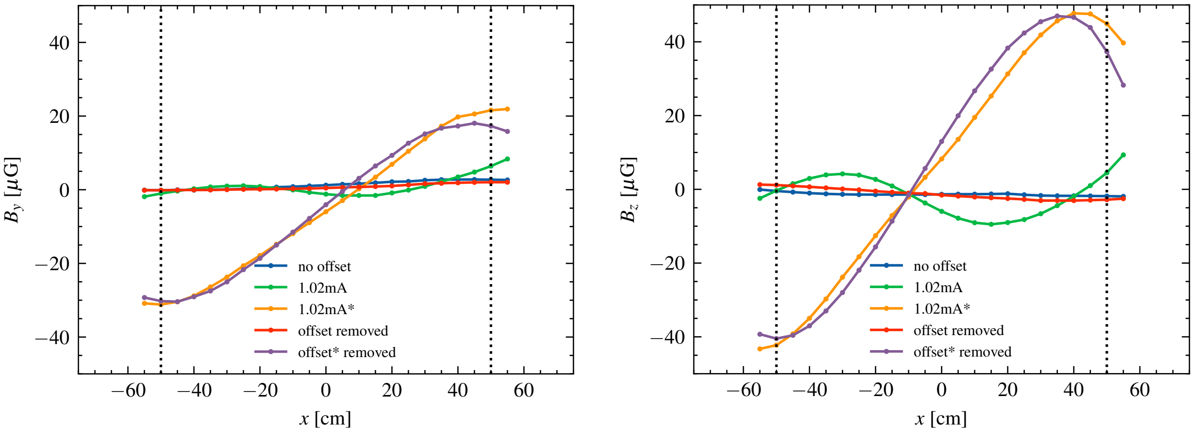

Figure 4.15: **The effect of offsets in the degaussing system.** Degaussing are performed on inner layer Y direction, and the measured residual field B_y (left) and B_z (right) are shown. The curves without "*" are the offset that is applied at the end of the degaussing sequence, which is equivalent with a finite DC field through the degaussing coils. The curves with "*" are the offset that is applied during the degaussing waveform, which leads to much larger residual fields and is not reversible.

by merely adjusting offsets.

To further elucidate these observations, comprehensive numerical simulations were conducted (Figure 4.16). The left panel of Figure 4.16 illustrates the effects of applying a minor offset current during a degaussing process utilizing the actual 4 s waveform. In this simulation, the mu-metal was modeled using the hysteric Jiles-Atherton approach [152, 153] to accurately represent its hysteric properties. Conversely, the right panel depicts the field generated by the degaussing coils under the assumption of an identical DC offset current applied to these coils, with the mu-metal modeled as a linear material possessing high permeability but devoid of hysteric effects. These simulations corroborated our experimental findings, confirming that the residual field distribution along the central axis of the spin-precession region indeed exhibits a "cubic" profile. Furthermore, the simulations revealed that the residual field induced by the magnetization is oriented in the opposite direction to the original applied field, a crucial insight into the further analysis of actual residual fields.

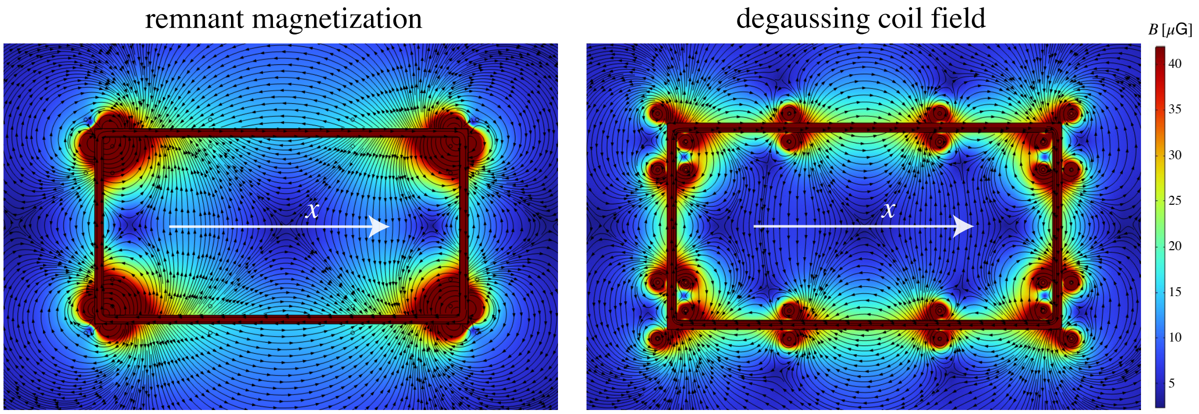
remnant magnetization

degaussing coil field

Figure 4.16: **Simulated field of the degaussing fields.** (left) The field from remnant magnetization in the mu-metal sheets due to an imperfect degaussing process, modeled as Jiles-Atherton hysteresis. (right) The field from a static offset current the degaussing coils, mu-metals are modeled as linear materials.

Results in Figure 4.15 suggest a $0.75\,\mu$G/cm gradient in B_y and $1.5\,\mu$G/cm gradient in B_z along the central line of the spin-precession volume, per 1 mA offset current applied during the degaussing process. This corresponds to maximum field of $B_y = 37.5\mu$G and $B_z = 75\mu$G, which was the largest contribution of the residual field in the spin-precession volume before we carefully studied its effect. In the ACME III degauassing system, the offset currents from the current amplifier is constantly monitored by a 0.47 Ω precision shunt resistor and read out by a 24-bit NI-DAQ device. Prior to each degaussing pulse, the offset current was measured and electronically compensated to below 50 μA, which, at the maximum, lead to about $4.2\,\mu$G residual field and $0.09\,\mu$G/cm field gradient in the spin-precession volume, below the ACME III design goal of $10\,\mu$G and $1\,\mu$G/cm. The residual field can vary by as much as $2\,\mu$G from one identical degaussing cycle to another, possibly due to the limited capability to monitor and cancel the offset smaller than 50 μA level. The residual field also varies by up to $5\,\mu$G depending upon which set of inner shields is degaussed last. These variations suggest that further optimization of the degaussing may be possible.

A complete degaussing process uses nine of the 4 s current pulses and takes 36 s. The first is sent to 12 degaussing coils wired in series to produce a field in one shield layer that circulates about the x axis. The second and third pulses make magnetic fields that circulate about the y and z axes. The outer shield layer is degaussed first, then the middle and inner layers. This layered approach to degaussing is strategic; it ensures that any magnetic fields penetrating from the exterior are systematically neutralized before addressing the innermost regions.

Not surprisingly, the degaussing of the inner layer is the most important. Because our ambient magnetic field typically remains relatively stable, degaussing the inner layer alone is most often sufficient to meet the stringent field requirements set for ACME III. When only the magnetic field within the internal volume of the shield is altered in most cases due to the reversal of applied bias field in ACME III degaussing just the inner layer also proves to be adequate, as we shall see, this maximizes measurement time.

For optimizing magnetic shielding, the process traditionally referred to as "degaussing" might more accurately be described as "magnetic equilibration" [128, 143]. This terminology reflects the process by which an alternating magnetic field effectively randomizes the magnetic domains within mu-metal, eliminating energy barriers that impede domain alignment. This equilibration leads to a state where the magnetization of the mu-metal balances with the external magnetic field, thereby removing hysteretic effects and enabling anhysteretic magnetization when an external bias field is present. Such conditions are typical when degaussing a shield in a non-zero ambient field. Notably, during this equilibration, the anhysteretic permeability of the shield often registers 2-3 times greater than its initial permeability, as governed by the dynamic behavior of the magnetic domains [152]. As a result, the residual magnetic field following the equilibration process is significantly smaller than one would expect based on the ambient field divided by the shielding factor. Although "degaussing" remains the conventional term used for familiarity, the concept of magnetic equilibration provides a more precise description of the process and its effects on the material's magnetic properties.

4.6 Effect of holes in the shield

The presence of holes in magnetic shields is a critical factor because the external magnetic fields obviously will leak into the interior volume of the shield through these holes. We studied these effects through finite-element simulations using the COMSOL Multiphysics software package.

To establish a baseline for understanding the effects of holes on magnetic shielding, initial simulations were conducted using a three-layered rectangular shield sized as the ACME III shields but with only one opening. These simulations assumed ideal conditions where the mu-metal's magnetization followed the anhysteretic magnetization path, implying perfect degaussing without residual magnetization. The studies were for a single opening on the side face of the shields. The inner shield is approximately 55 cm from the spin-precession volume as in ACME III shields. Two configurations were examined: one featuring a circular hole with diameter d, and another with a rectangular slot having a height of d and a width of $d/3$. The latter geometry was then adopted to give access for state preparation and readout lasers.

The largest field amplitude in the spin-precession volume was plotted versus d in Figure 4.17. The residual field is a constant value that is independent of the d while d is small enough. As d gets larger, the effect of holes start to play a role. When the ambient field is perpendicular to the face of the holes (solid lines in Figure 4.17), the hole effect is over 1000 times larger than when the field is parallel to the hole faces (dashed lines). The ACME III shield choices of a largest hole size of $d = 7.62\,\text{cm}$ and a largest slot size of $d = 14.5\,\text{cm}$ are indicated on Figure 4.17, as the requirement

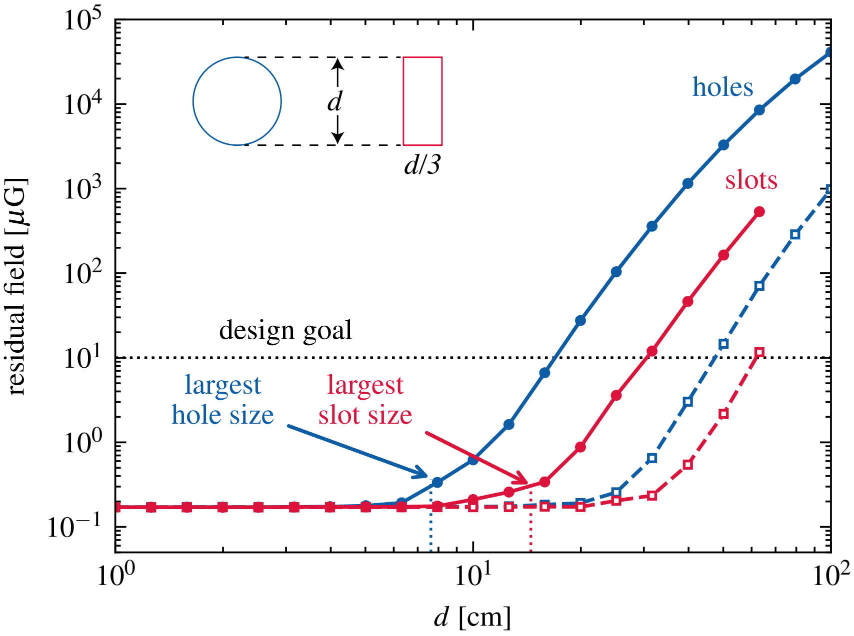

Figure 4.17: **The effect of holes in the shield** for an uniform ambient of $522\,\mathrm{mG}$ (see Figure 4.1). The ambient field perpendicular to the face of the holes (solid lines) was found to have a much larger effect than when the field was parallel to the hole faces (dashed lines). The largest d of the slots and holes in the actual ACME III shield design are indicated.

by a safety margin that is below the $10\,\mu$G goal.

The leakage field from the slots is observed to be significantly smaller than that from the circular holes, as one of its dimensions is reduced as $d/3$. For both cases, the leakage field seems to have a power-law relationship with d. The power-law index is about 6 with d, or about 3 with the area of the opening, for both cases.

Further simulations were conducted to include all relevant apertures present on the actual ACME III shield, as mentioned in section 4.3.2, though holes smaller than 0.5 inches in diameter were excluded to simplify the model and reduce computational demands. This comprehensive simulation aimed to assess the collective effect of all apertures under the assumption of perfect degaussing. The results, shown in previous sections as Figure 4.4 suggested that even with all considered holes, the residual magnetic field within the shield could be maintained well below the stringent $10\,\mu$G design goal, with enough margin for imperfect degaussing.

4.7 Measuring magnetic field

4.7.1 Magnetometers

In order to characterize the shielding performance of the ACME III shield as well as understanding the residual field, we employed three types of 3-axis magnetometers were employed to measure various magnetic field components: ambient fields, fields produced by coils, and remnant magnetism within the precession volume. Each magnetometer type was chosen based on its sensitivity, operational range, and suitability for specific magnetic environments, as summarized in Table 4.2. This table presents the specifications from the datasheets of these magnetometers, providing an initial understanding of each device's capabilities.

The datasheet sensitivities of these magnetometers were validated through experimental mea-

magnetometer	sensitivity (μG/$\sqrt{\text{Hz}}$)	range	absolute accuracy	typical offsets
fluxgate	0.06	1 G	0.5%	0.5 mG
magnetoresistive	3	1 G	N.A.	3 mG
optical-pumped	1.5×10^{-4}	0.5mG	N.A.	40 μG

Table 4.2: **The specs of used magnetometers.** Fluxgate: Bartington Mag-13MSL100. Manetoresistive: Twinleaf VMR. Optical-pumped: QZFM-Gen3 with Rb atom vapor cell [157], operated in zero-field mode. Sensitivity are expressed in noise power spectrum densitiy (PSD). Two types of magnetometer don't have absolute accuracy specifications.

surement of the magnetic field noise, which is quantified as the square root of the power spectral density (PSD) computed from the time-dependent magnetic field signal. While all magnetometers demonstrated magnetic field noise slightly above the datasheet specifications, they performed satisfactorily under the requirement of less than $10\,\mu$G for our experiments.

On the other hand, all three types of sensors have inevitable offsets. The fluxgate and magnetoresistive sensors exhibited significant and unstable offsets, sometimes as large as a few mG, which posed challenges in measuring absolute magnetic fields at the μG level. Additionally, the $\sim 5mG$ magnetism of ethernet connectors used with the magnetoresistive sensors complicated their use to measure extremely small fields. Both the fluxgate and magnetoresistive magnetometers operate in the Earth's ~ 0.5 G magnetic field. The optical-pumped magnetometers only could operate below $500\,\mu$G.

Based on their different characteristics, these sensors were strategically deployed to monitor various magnetic field conditions. Magnetoresistive magnetometers were used to monitor the ambient magnetic fields in the laboratory, to measure the fields between shielding layers, and to measure the fields produced by coils outside the magnetic shields. Optical-pumped Rb magnetometers were tasked with measuring the magnetic fields within the precession volume, especially when the magnetic shields were in place. Fluxgate magnetometers were used to calibrate the main coil system and any other equipment that produces or controls magnetic fields, as it has the absolute scale calibration to 0.5% and offers a good balance between sensitivity and operation range. It is also used as a reference to calibrate the other magnetometers.

Significant efforts were made to measure and correct for sensor offsets, which involved rotating or reversing the direction of the sensors in a stable field environment provided within a standard three-layer magnetic shield (Bartington TLMS) that is known to reduce the interior field to a few μG. By rotating the sensor 180 degrees along its x axis before the field has changed, for example, isolated the offsets for the y and z directions. Such rotation is performed for all three axes thus the offset of all sensor axes can be determined. Although these offsets are claimed to be stable over time according to their manufacturers, frequent recalibration was performed. Throughout the magnetic field measurements, the largest offset corrections observed were for the magnetoresistance magnetometers (up to ± 3.5mG), with variations of about 0.1 mG over a month. In contrast, the Rb magnetometers showed the smallest offset corrections (up to ± 61 μG) and exhibited minimal changes over two months.

We performed a in-house calibration of the fluxgate magnetometers before relying upon its absolute accuracy claim. Figure 4.18 shows the calibration of the fluxgate magnetometers using a simple solenoid, whose field can be precisely calculated using $B = \frac{\mu_0 N I}{L}$. Uncertainties are primarily due to the uncertainty in the length measurement of the solenoid windings and the current measurement. The calibration shows verified the accuracy of the fluxgate readings against expected values, achieving an uncertainty significantly better than the specified 0.5% accuracy. These calibrated fluxgate measurements were then used to adjust the readings from the magnetoresistive and optical-pumped magnetometers, ensuring overall measurement accuracy across all devices. It turns out that the largest correction factor required for the magnetoresistive and optical-pumped sensors are 1.10 and 1.17, respectively.

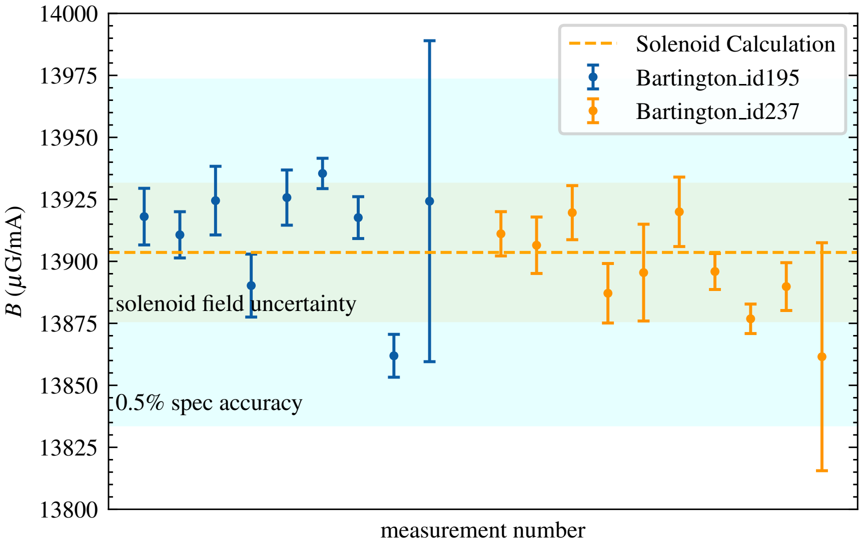

Figure 4.18: **The Calibration of the fluxgate magnetometer.** Two fluxgate magnetometers were calibrated with a constructed coil whose field can be precisely calculated. The 0.5% spec accuracy and the uncertainty for the solenoid field calculation are indicated.

4.7.2 Setup for field measurements

To precisely measure the residual fields within the spin-precession volume, we first employed optical-pumped magnetometers, translating them through the spin-precession volume. This translation was along the x coordinate through the central beamline, and along the z coordinate at $y = 0$ and $x = \pm 500$ cm. Given the small expansion of the molecule beam in the y and z directions, the probulation along x coordinate predominantly captures the magnetic field distribution within the spin-precession volume. The consistency and low variation across the transverse directions were then validated through additional scans along the z coordinate.

To continuously monitor magnetic field variations when it is not possible to put magnetometers in the spin-precession volume, eight optical-pumped magnetometers were inserted into designated pockets within the interaction chamber, as mentioned in Section 4.3.1. Two magnetometers were installed on each side face and four on the top face of the chamber. Magnetometers can be inserted to the end of the pocket, which is a cylindrical aluminum tube that extends into the interior region of the interaction chamber. This configuration allowed the magnetometers to be inserted from outside as close as possible to the spin-precession volume. A schematic of this design is depicted in Figure 4.19 The real-time data collected from these magnetometers will be crucial for monitoring any perturbations in the magnetic field during eEDM measurements.

(a) side view

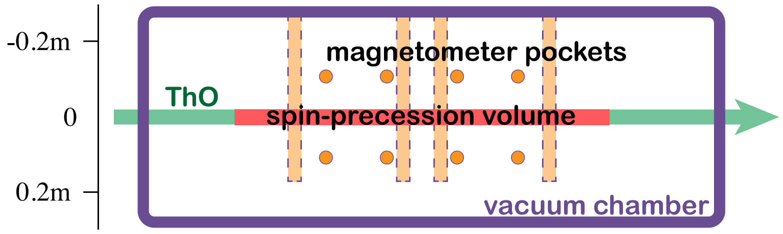

(b) top view

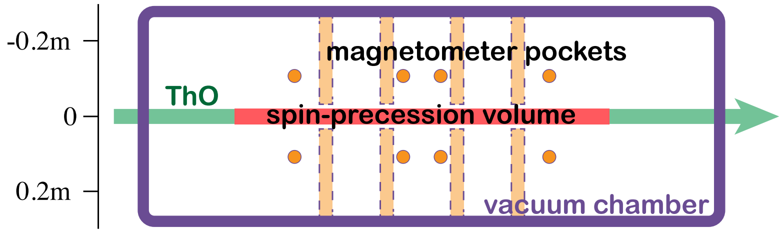

Figure 4.19: **The schematic of the interaction chamber with magnetometer pockets.** Views are from side (a) and top (b). the pockets are aluminum cyliners that extends into the interior region of the chamber, allowing the magnetometers in atmosphere to be inserted as close as possible to the spin-precession volume.

In addition to the measurement system mentioned above, the ThO molecule beam itself will be used to probe the magnetic field [115]. This technique offers a substantial advantage as it measures the magnetic field precisely at the location of the molecule beams. The metastable Q $^3\Delta_2$ state of ThO was chosen for this purpose. It exhibits a long lifetime of about 0.6 seconds, which ensures that the population of the molecules remains stable throughout their transit time in the apparatus, typically a few milliseconds. This state is characterized by a large magnetic moment ($g_Q \sim 2$), providing enhanced sensitivity to magnetic fields compared to other states like the H state ($g_H \sim 0.0088$) used for probing the electron EDM, or the X state ($g_X < 0.001$) which is the ground state of ThO [115]. Furthermore, the existing electrostatic focusing lens upstream of the experiment in ACME III, which exploits the same Q state to collimate the molecule beam due to its large Stark shift, also facilitates state preparation with no additional effort or cost. The same Ω-doubling structure with a $2\pi \times 10$ kHz splitting makes the polarization of the Q state straightforward with the same electric field plate system used for H state, resulting exactly same experiment protocols for probing magnetic field.

This method reads the Zeeman phase shift of Q state in presence of magnetic fields. Based on the statistics of the readout system in ACME III, an integral of a few seconds would let the sensitivity of the Q-state magnetometers below $1\,\mu$G. Operational range of $250\,\mu$G can be achieved, which corresponds to the Zeeman phase becomes 2π. However, only time-averaged magnetic field was measured in the spin-precession volume, over the course of a few ms which is the travel time of molecule beam in the apparatus, limiting its bandwidth to a few hundreds of Hz.

While the Q-state magnetometry is specifically sensitive to the B_z component, this is the most crucial element to control in electron EDM measurements. The state preparation is executed by directing a strong, short laser pulse counter-propagating to the molecular beam, initialize the state across all x coordinates of the molecular beam. As the molecules travel toward the detector, they experience magnetic fields that is varied in space, accumulating phase shifts that are directly proportional to the field strength. Resolving the phase for fluorescence signals at different time would resolve the magnetic field distribution on different location of x.

The compatibility of the Q-state magnetometry with the existing measurement protocols used for electron EDM experiments is particularly beneficial. It allows for the implementation of numerous experimental controls designed to reject systematic effects, thereby enabling error-free absolute measurements of B_z. As of the completion of this thesis, this method was demonstrated to be able to accurately resolve magnetic fields as fine as $1\,\mu$G and gradients as subtle as $0.1\,\mu$G/cm. The Q-state magnetometry will be integrated into eEDM measurement sequence, likely every few hours, to monitor the magnetic field in-situ as the measurement data accumulates.

4.8 Characterization of shield performance

In Section 4.1, we discussed the importance of suppressing magnetic fields and their gradients within the spin-precession volume to levels below $10\,\mu$G and $1\,\mu$G/cm, respectively. These stringent requirements are necessitated by the high precision demanded in ACME III. The total magnetic field environment within this volume is influenced by two primary sources: the residual magnetization emanating from the shields themselves and any ambient fields that penetrate the shielding apparatus. This section presents a comprehensive characterization of the ACME III shield performance with respect to both of these contributing factors. Our analysis aims to quantify the efficacy of the shielding system in mitigating these potential sources of magnetic interference, thereby ensuring the integrity of our experimental measurements.

4.8.1 The residual field

To measure the residual fields from the mu-metal shields after degaussing, an optical-pumped magnetometer is inserted into the magnetic shield through various access holes. The magnetometer is mounted on a non-magnetic sliding rail system that allows precise positioning within the shield, with an accuracy of ± 1 mm. At each position along the rail, the magnetometer was rotated about the x axis to remove offsets in the B_y and B_z measurements. Offsets in B_x were removed by reversing the probe's direction along the z axis.

Figure 4.20 presents a comprehensive analysis of the residual magnetic field within the shielding apparatus. Panel (a) illustrates the field distribution along the x coordinate at $y = z = 0$, while panel (b) depicts the field variation along the z coordinate at $y = 0$ for x values of -500, 0, and $500,$ cm. Our measurements reveal that the residual fields were consistently maintained below $10, \mu$G, with gradients not exceeding $0.1, \mu$G/cm throughout the spin-precession volume. These results are in agreement with the design specifications outlined in Section 4.1, and are the central results of our evaluation of the ACME III magnetic shielding system's performance. Given its critical importance, we conducted multiple rigorous measurements over an extended period to ensure reproducibility and reliability. Specifically, over the course of more than one year following the completion of shield construction, the shielding assembly underwent three complete cycles of dismantling and reassembly. Notably, the residual field measurements obtained after each reassembly was consistent.

The Rb sensor offsets were observed to be stable over time, as described in Section 4.7.1. This allows the possibility of measuring these offsets in a separate, smaller calibration shield (Bartington TLMS) with known residual field and stability. A reliable database of offsets thus can be made and referenced in real-time during experimental measurements, thereby enhancing the efficiency of magnetic field data collection. The low levels of residual magnetic field observed were attainable only after the degaussing process discussed in Section 4.5, which serves to equilibrate the magnetization of the mu-metal components of the shield with the external magnetic field.

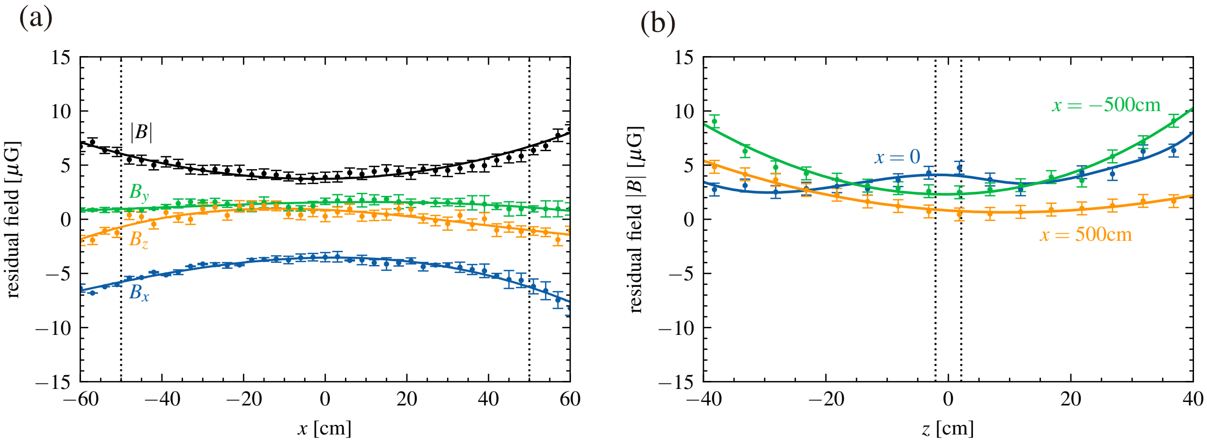

Figure 4.20: **The residual field within the shield.** (a) shows the field scanned along x coordinate at $y = z = 0$, while (b) shows the field scanned along z coordinate at $y = 0$, $x = -500, 0, 500\,\text{cm}$. Sensor offsets are corrected by rotating the sensor at each data point, with their scale factor calibrated.

4.8.2 The shielding factor

We initially tested the shielding capability for the changes of ambient field with a high solenoid in the lab. The solenoid was capable of producing a field of -5.5T to 5.5T in its internal region. Given that it's only about 6 m away from the ACME III apparatus, operation of this solenoid has been one of the largest concern for the magnetic field stability of the ACME III experiment. The fringe field from this solenoid, measured about 2 m right above the ACME III shield, was $-260\,\text{mG}$ to $260\,\text{mG}$ with most of its component pointing to the y direction (along gravity). This field disturbance is about half as the amplitude of the earth's magnetic field in the lab and has been the largest source of magnetic field disturbance we have identified so far.

A comparison of the shielded field with the ambient field can be seen in Figure 4.21. While the ambient field was measured to have a disturbance of about $520\,\text{mG}$ (Figure 4.21 (a)), significant change of the field in the shielded volume was observed, with amplitude of about $29\,\mu\text{G}$ (Figure

4.21 (b)). The shielding factor is thus about $18,000$. Figure 4.21 (c) shows the correlation between the two fields. The change of the solenoid field is within 40 mins, a time scale much slower than the measurement of eEDM. Nevertheless, time delay in the response of the shielded field was spotted.

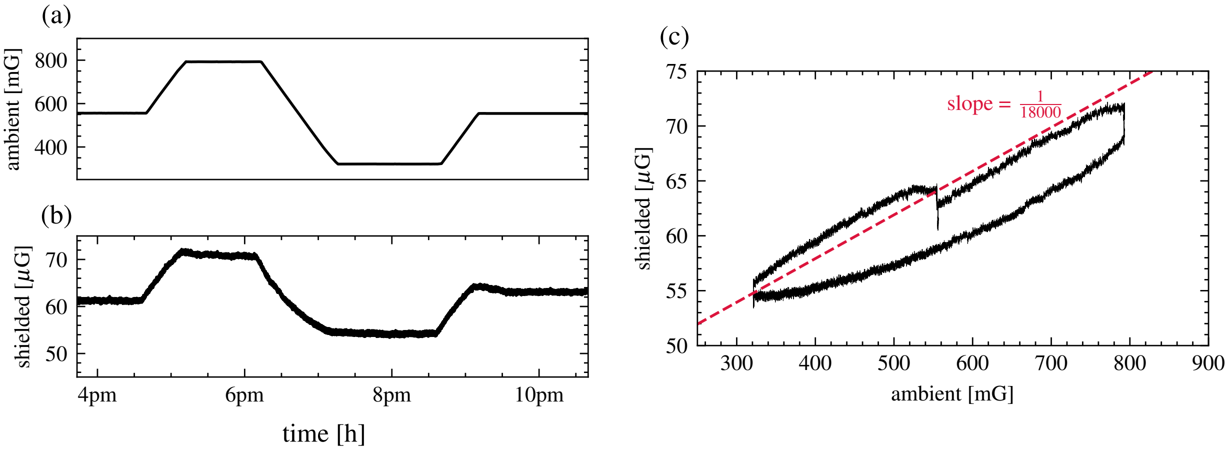

Figure 4.21: **The effect of fast solenoid on the shielded field.** (a) the change of the ambient field, measured approximately 2 m right above the shield. (b) the change of the shielded field, meeasured at the center of spin-precession volume. (c) the correlation between two measured fields. Slope of the reference line indicates the shielding factor.

We continued to explore the interaction between ambient field changes and the degaussing (magnetic equilibration) process. In this test, we ramped the ambient field to $+260\,$mG, and degauss the ACME III shield with the 4 s pulse on all three layers. A residual field distribution similar to Figure 4.20 was recorded, which is below $10\,\mu$G, suggesting that the residual field was not significantly affected by the ambient field. This result is consistent with the expectation that the degaussing process effectively equilibrates the mu-metal magnetization, resulting in field attenuations larger than the shielding factor, and the residual field was primarily determined by the remanence of the mu-metal from the degaussing process.

Further investigations into the shielding properties against time-varying external fields were conducted using three pairs of external coils positioned just outside the outer magnetic shield.

These coils are in a rough Helmholtz configuration and each pair generate magnetic fields in the x, y and z directions, respectively. Field measurements within the shields were performed using an Rb magnetometer placed at the center of the precession volume. The coil currents were varied sinusoidally at different frequencies, and the in-phase component of the detected field was extracted to evaluate the frequency-dependent shielding factor, as shown in Figure 4.22.

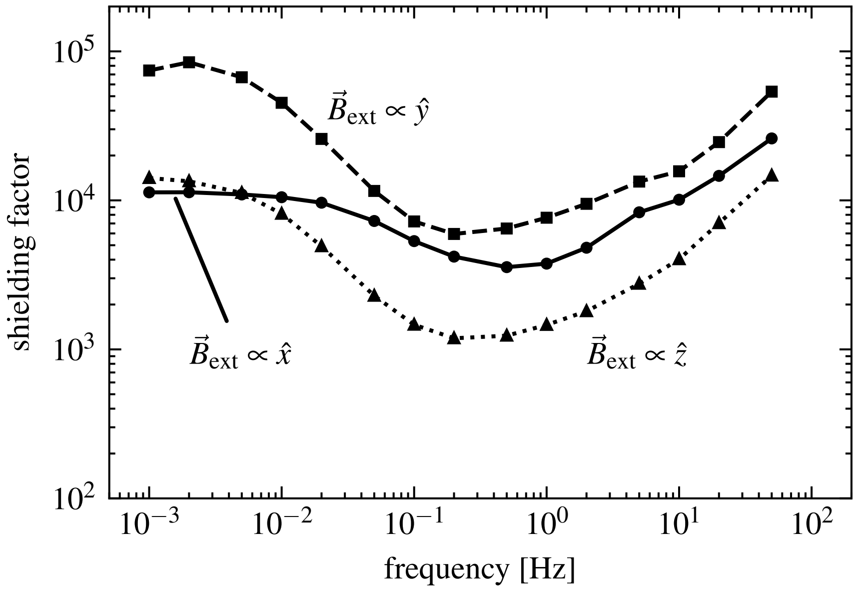

Figure 4.22: **The shielding factor of the ACME III shield.** Measurements are done with the three pairs of external coils aligned in x , y and z directions.

The shielding factor is frequency dependent, because the mu-metal's permeability decreases with the increasing frequency, as explained in Section 4.4.2. On the other hand, the eddy current effect would become more significant at higher frequencies, which would enhance the shielding factor. The combination of these two effects would explain the dependence of shielding factor with frequency.

Due to the difference of dimensions and hole patterns on each face, the shielding factor is also direction dependent. At low frequencies close to DC, the shielding factor is about 10,000 for B_x

and B_z, and 8000 for B_y. At higher frequencies, the shielding factor drops significantly to about 1000 for B_z and about 5000 for B_x and B_y. With frequency higher than about 0.5 Hz, the eddy current shielding starts to play a role and the shielding factor increases with frequency. The trend of shielding factors on x and y axes are similar, unveiling the similar dimensions of shield on these two direction. However, the nearly factor-of-8 discrepancy between their shielding factors remain a mystery. Further investigation is required to understand the cause of this effect. Nontheless, these shielding factors ensures the effective shielding of any ambient field changes to below $10\,\mu$G in the spin-precession volume.

4.8.3 After the shielding studies were completed

Following the completion of these comprehensive shielding studies, it became necessary to dismantle the shields to facilitate the integration of other critical components of the experimental apparatus. These components included the electric field plates, ThO detection system,laser access windows etc., all of which are essential for a complete electron EDM measurement. This reconfiguration imposed certain constraints on our subsequent magnetic field characterization efforts. Specifically, magnetometers could only be positioned approximately 21 cm away from the central x axis, as direct insertion into the precession volume would necessitate a complete disassembly of the apparatus. Given that an electron EDM measurement is currently ongoing, such a disruptive intervention is not feasible at this juncture.

Upon reassembly of the shielding system with the full experimental apparatus in place, we conducted preliminary measurements of the residual field. These measurements revealed a notable increase in the residual field by approximately a factor of three compared to our previous observations when the shields were assembled without the internal apparatus. Concomitantly, we observed a reduction in the AC shielding factor by approximately a factor of two. The precise etiology of these changes remains unclear. At present, we lack sufficient evidence to definitively attribute these alterations to either the presence of the additional ACME apparatus within the shield or a potential deterioration in the magnetic properties of the shielding materials themselves. This matter is currently under rigorous investigation by other members of the ACME collaboration.

However, these observed changes do not presently pose a significant impediment to the ACME III eEDM measurement. The increased residual magnetism can be effectively mitigated through the use of internal compensation coils, a topic that will be discussed in depth in Chapter 5. We found that the residual field levels achieved after the active cancellation remain well within the requirements for a shot-noise limited measurement in the ACME III experiment. Nevertheless, we acknowledge that any further deterioration in shielding performance over time or through repeated assembly and disassembly cycles would be undesirable. In the unlikely event that such a scenario materializes, we retain the option of implementing the extreme remedy of complete dismantling and re-annealing of all mu-metal sheets.

4.9 Summary

The ACME III magnetic shields were designed, constructed, and rigorously tested over a year. It reduced the magnetic field within a $1\,\mathrm{m} \times 4.2\,\mathrm{cm} \times 4.2\,\mathrm{cm}$ spin-precession volume to below $10\,\mu$G and gradient less than $1\,\mu$G/cm despite being disassembled and re-assembled to modify apparatus in the shielded volume. All the desired field requirements for a shot-noise limited eEDM measurement were met, and the residual field achieved by the ACME III shields is comparable with several magnetic shielding systems cited in the literature [128, 158, 159]. The ACME III shields achieve this using less volume, incurs lower costs, and only three layers of mu-metal.

Note added after this thesis work: After this performance was demonstrated for a year, the full

ACME III apparatus was placed in the shielded volume. The residual field increased by about a factor of 3 and the low frequency shielding factor decreased by about a factor of 2. This change, now under study by other members in our Northwestern ACME team, is not yet fully understood. Fortunately, this will not impede the ACME III eEDM measurement in so far as the increased residual field can be cancelled using coils described in the next chapter, and the ambient field is still adequately shielded.

CHAPTER 5

MAGNETIC FIELD COILS

The highly uniform magnetic fields needed for the ACME III electron EDM measurement is produced by a unique double layer, self-shielding magnetic field coil. Moreover, in order to study systematic effects and compensate unwanted residual magnetic fields and gradients, an auxiliary coil system is also designed and constructed, enabling complete magnetic field and gradient control for any component in the ACME III spin-precision volume. This chapter describes its design and construction, and their measured performance.

5.1 Overview of the coil system

5.1.1 The main z coil

The spin precession of the ThO molecules requires a uniform bias magnetic field $\mathbf{B} = B_0\hat{z}$ to be applied horizontal in the lab frame, perpendicular to the direction of travel for the ThO molecules along the x axis. In ACME I and ACME II, this was done by a so-called "cosine-θ" coil, in which the current wirings are wound on the surface of a cylinder, with the wiring density proportional to the cosine of the azimuthal angle [70, 82] to produce a uniform magnetic field on the z direction.

The upgrade of the ACME III coil system was motivated by the following considerations. Firstly, ACME III is planning to achieve a five-fold increase in coherence time compared to its predecessor. This enhancement necessitates a corresponding five-fold increase in the length of the spin-precession volume. Such a significant change in experimental parameters demanded a complete redesign of the coil system to accommodate the extended geometry while maintaining the required field uniformity.

Secondly, we wanted this redesign to feature a shift from cylindrical to rectangular geometry for the whole coil system, in accordance with the magnetic shielding system that was also redesigned to be rectangular in ACME III. The adoption of a rectangular design offers increased compactness and modularity of the entire experimental assembly, minimizes the apparatus volume and cost. It also eliminated the need to maintain a cylindrical structure for the coil and shielding system, which is typically heavy and challenging to keep in shape during extended experimental runs and frequent maintenance.

Thirdly, we wanted to minimize the shield magnetization produced by the exterior fields from the coil. Experience from the ACME II experiment revealed a critical issue: the fringe field generated by the cosine-θ coil induced residual magnetization in the inner layer of the magnetic shield. This unwanted magnetization substantially reduced the effectiveness of the shielding system. To address this problem, we implemented a novel "self-shielding" coil design. This approach arranges the coil windings in a configuration that largely cancels the net field outside the coil boundary, significantly reducing shield magnetization.

The concept of active shielding, which inspired this design, originated from our team's previous work on actively-shielded, high-field solenoids [160, 161]. While the principle of active shielding is well-established for axial fields in solenoids and MRI magnets [162, 163], our application required adaptation for a field perpendicular to the coil's long axis, as briefly sketched in Figure 5.1. This unique requirement led to the development of a novel mathematical method for determining the optimal coil geometry, which will be detailed in Section 5.2.2.

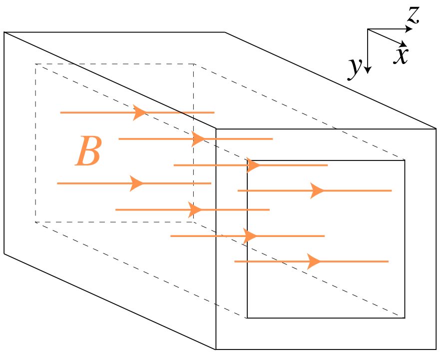

Figure 5.1: **Demonstration of desired field geometry for the main z coil.** The desired field is uniform along the z direction inside the coil, and zero outside the coil.

5.1.2 The auxiliary coils

The ACME experiment's sensitivity to magnetic fields and gradients necessitates precise control and characterization of these parameters within the spin-precession volume. To address this critical need, we have designed and implemented a set of auxiliary coils that serve two essential functions:

- Residual field compensation: The auxiliary coil system is primarily designed to compensate for any residual magnetic fields that persist despite the presence of magnetic shielding. This compensation capability ensures that the spin-precession volume maintains the high degree of magnetic field uniformity required for accurate EDM measurements.
- Systematic error evaluation: In addition to field compensation, the auxiliary coils play a crucial role in assessing systematic uncertainties in our EDM measurements. By deliberately introducing controlled field perturbations, usually much larger than the typical amplitude

of system imperfections in the actual eEDM measurement, we quantify the experiment's sensitivity to various magnetic field errors.

The auxiliary coil system comprises three distinct coils: B_x, B_y and dB_z/dx. Each coil is designed with reversible current sections, allowing for the generation of both uniform fields and linear field gradients. We shall see soon that the combination of these coils cover all independent magnetic field and gradient components. Figure 5.2 presents a schematic overview of the auxiliary coil configuration, illustrating their spatial arrangement and field orientations. This design allows for independent control of magnetic fields and gradients along multiple axes, providing the flexibility needed for both error compensation and systematic studies. For the auxiliary coils, no self-shielding design is implemented in order to minimze the complexity and the cost of the system.

According to Maxwell's equation, in free space, a static magnetic field satisfies:

$$\nabla \cdot \mathbf{B} = 0, \quad \nabla \times \mathbf{B} = 0 \tag{5.1}$$

This produces constrains on magnetic field gradients:

$$\frac{\partial B_x}{\partial x} + \frac{\partial B_y}{\partial y} + \frac{\partial B_z}{\partial z} = 0 \tag{5.2}$$

$$\frac{\partial B_x}{\partial y} - \frac{\partial B_y}{\partial x} = 0 \tag{5.3}$$

$$\frac{\partial B_x}{\partial z} - \frac{\partial B_z}{\partial x} = 0 \tag{5.4}$$

$$\frac{\partial B_y}{\partial z} - \frac{\partial B_z}{\partial y} = 0 \tag{5.5}$$

Thus, only 5 of the 9 magnetic field gradient components are independent. For the three "diagonal" gradient components ($\partial B_x/\partial x$, $\partial B_y/\partial y$, $\partial B_z/\partial z$), they are generated by B_x, B_y, and self-

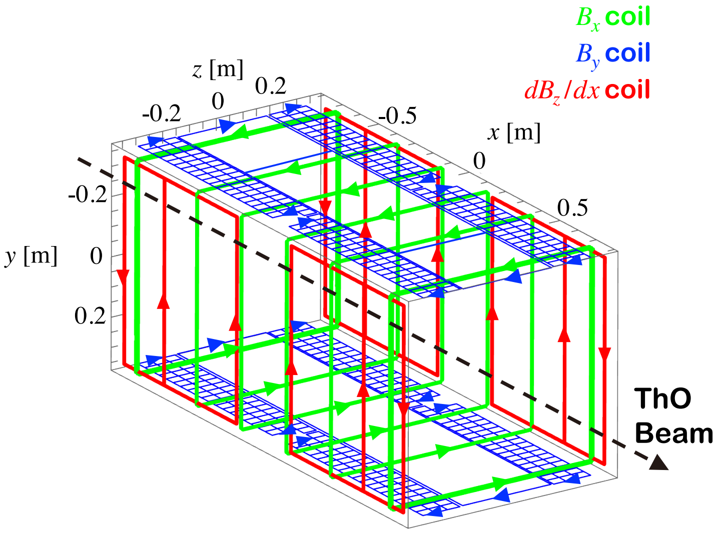

Figure 5.2: **Schematic of all the auxiliary coils. green:** B_x and dB_x/dx; **blue:** B_y, dB_y/dx, dB_y/dy and dB_y/dz; **red:** dB_z/dx. Combined with the gradient mode of the main z coil, all the independent magnetic field gradients can be generated.

shielding main B_z coil, respectively, while current is reversed on half of the coil. As constrained in Eq. 5.2, controlling one of the component necessarily alters the values of other gradients. By applying linear combinations of these gradients, their systematic effects on the eEDM measurement can be analyzed individually. The off-diagonal components, as described in Eqs. 5.3 - 5.5, are characterized by pairs of equal but opposite components. We control these as follows:

- dBy/dy and dBy/dz: Controlled by y coils
- dBz/dx: Controlled by a dedicated dBz/dx coil

5.2 Design of the main coil

5.2.1 Boundary value problem for magnetic fields

The design of the main z coil was approached by solving a time-independent boundary value problem on a two-dimensional plane [164, 165], as illustrated in Figure 5.3. The model is situated in free space, where the relationship between magnetic field $\mathbf{B}$ and magnetic field intensity $\mathbf{H}$ is given by $\mathbf{B} = \mu_0 \mathbf{H}$, with μ_0 being the permeability of free space. Current flow is confined to the boundaries of the model.

In each domain depicted in Figure 5.3(a), the magnetic field can be expressed in terms of a scalar potential φ:

$$\mathbf{H} = -\nabla\varphi \tag{5.6}$$

The scalar potential satisfies Laplace's equation:

$$\nabla^2\varphi = 0 \tag{5.7}$$

Dirichlet boundary conditions for the scalar potential φ are imposed on the boundaries where the normal field component equals to 0, while Neumann boundary conditions are assigned on the boundaries where normal field component equals to B_0. The continuity of the normal components of the magnetic field across these boundaries is ensured by the divergence-free nature of $\mathbf{B}$ field, i.e., $\nabla \cdot \mathbf{B} = 0$. As shown in Figure 5.3(a), the two vertical inner boundaries have the condition $\partial\varphi/\partial\hat{\mathbf{n}} = \pm B_0/\mu_0$ where B_0 is the desired magnetic field strength, and all other boundaries satisfy $\partial\varphi/\partial\hat{\mathbf{n}} = 0$. Here, $\hat{\mathbf{n}}$ denotes the unit normal vector to the boundary.

The distribution of the magnetic scalar potential was obtained using a finite-element method, with the results presented in Figure 5.3(b). It is important to note that the potential is discontinuous across the boundaries due to the presence of current. Consequently, the potential is solved separately in each domain. This discontinuity is related to the current density $\mathbf{J}$ on the boundary through Maxwell's equation:

$$\hat{\mathbf{n}} \times (\nabla\varphi_1 - \nabla\varphi_2) = \mathbf{J} \tag{5.8}$$

This equation implies that the local current density on the boundary is equal to the difference of the gradients of the magnetic scalar potential on both sides of the boundary [166]. In practice, this continuous current distribution is approximated by a discrete set of windings. Each winding is positioned to coincide with the equipotential lines of the magnetic scalar potential. The difference of the scalar potential values between adjacent equipotential lines are equal, ensuring that the current flowing through the windings is uniform. This discretization allows for the practical implementation of the coil design while maintaining the desired magnetic field characteristics.

The methodology described above allows for the solution of the magnetic scalar potential for an arbitrary desired magnetic field. In practice, the current wirings in the target domain and the return domain naturally form two discrete sets of wirings, which are constructed as separate structures in

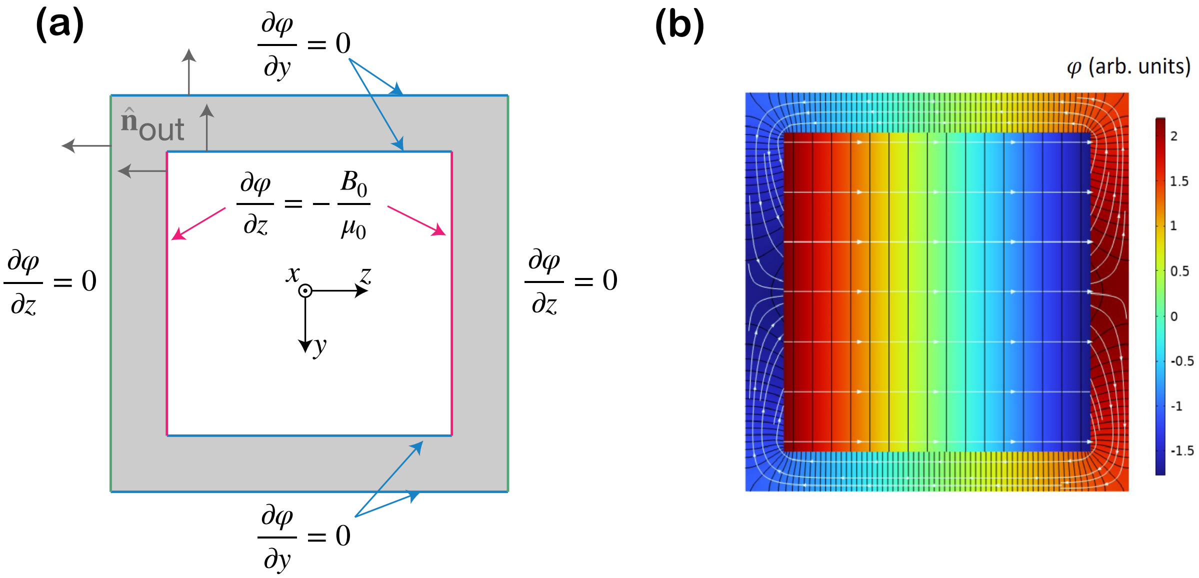

Figure 5.3: **The 2D boundary problem for the main z coil.** (a) The desired field is uniform inside the coil, and zero outside the coil. This defines the boundary conditions of the magnetic scalar potential on the corresponding boudaries. (b) The solved magnetic scalar potential. The black lines are the equipotential lines, which we will show shortly that they coincide with the ideal coil windings to generate the desired field. B field lines are shown in white arrows.

the physical implementation. As illustrated in Figure 5.3(b), the equipotential lines of the scalar potential are nearly linear segments, and this approximation was adopted in the actual ACME III coil construction to simplify the manufacturing process while maintaining the desired field characteristics.

It is important to note that the transition from the idealized mathematical model to a practical coil design introduces several sources of error. These include the approximation of a continuous current distribution by discrete wires, geometric inaccuracies in wire positioning, necessary wire reroutings around structural holes or obstacles, and the generalization of the two-dimensional problem to a three-dimensional reality. Each of these potential error sources was carefully evaluated and minimized through comprehensive numerical simulations, as will be discussed in the next section.

5.2.2 Wiring approximations

The discrete wire approximation was optimized through a delicate balance between competing design constraints. On one hand, closely-spaced wires were necessary to accurately replicate the continuous current distribution predicted by the scalar potential solution. On the other hand, reasonable spacing between wires was maintained to minimize intersections with access holes and mounting structures, thereby reducing the rerouting error. The optimized 2D pattern was then generated into a 3D structure by projecting onto the two end surfaces of the coil, perpendicular to the coil's long axis (x direction), and connected by straight wire segments running parallel to the x axis.

The final wire configuration was determined through an extensive process combining numerical simulations with manual adjustments, resulting in a design consisted of two distinct coil sections (see Figure 5.4): an 16-turn inner coil, corresponding to the target domain of the scalar potential solution, and an 198-turn outer coil, representing the return domain. The outer coil can be intuitively understood as a return yoke for the flux generated by the inner coil, while engineered so that their net field adds for a very uniform field in the target volume and largely cancels outside the coil boundary.

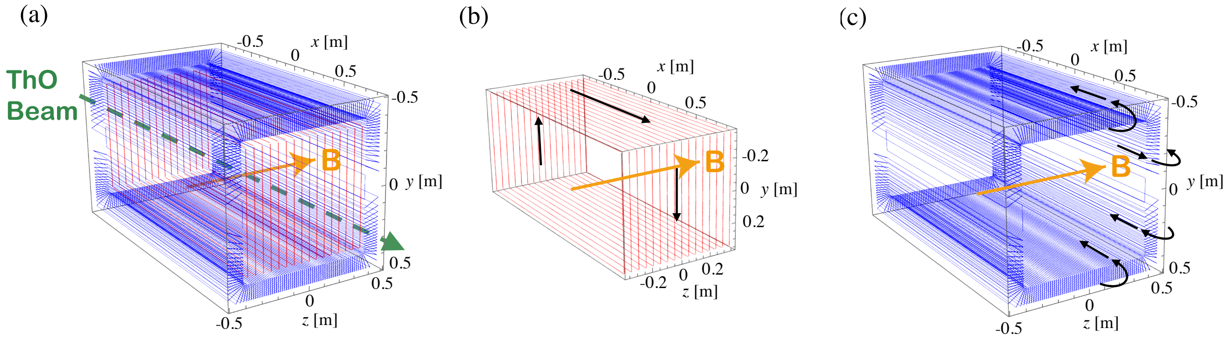

Figure 5.4: **The design of the main z coil.** (a) The main z coil is a combination of an inner coil and an outer coil. (b) The inner coil. (c) The outer coil. The direction of ThO molecule beam, the flow of current, and the direction of generated magnetic field is shown.

In the practical implementation of the coil design, it was necessary to reroute certain wires to accommodate structural features such as access holes. These reroutings were modeled as small current loops in close proximity to the straight wire segments, as illustrated in Figure 5.5. Given that the spin-precession volume is situated at a considerable distance from the coil surface where the current-carrying wires are located, the magnetic field effect of these rerouting loops can be approximated using the magnetic dipole model. Its contribution to the magnetic field contribution at a far point can be expressed as:

$$B_{\text{loop}} = \frac{\mu_0 I r^2}{2d^3} \tag{5.9}$$

Where r is the characteristic radius of the loop, d is the distance from the loop to the spin-precession volume, and I being the supplied current. To evaluate the magnitude of this effect,

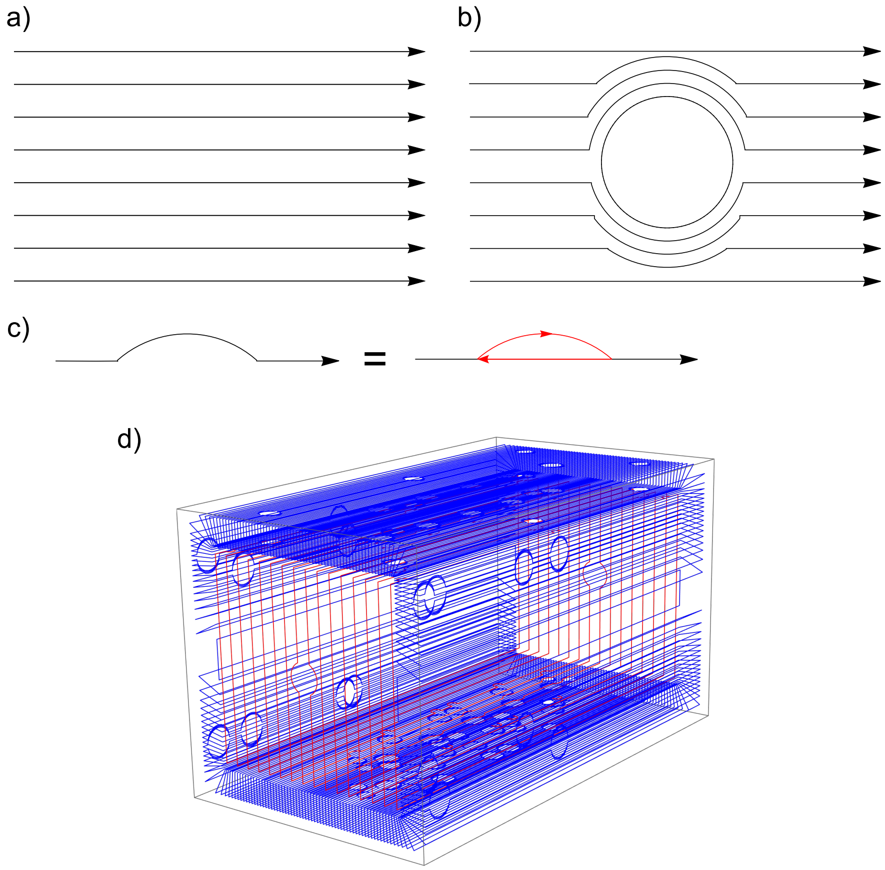

Figure 5.5: **Wire reroutings accounting for the holes on the magnetic field coils.** (a) A set of straight coil wirings. (b) The wires rerouting around a hole. (c) The effect of the rerouting is equivalent to adding a small current loop near the straight wiring. (d) The simulation model taking all the reroutings into account.

we considered a worst-case scenario with $r \approx 40\,\mathrm{mm}$, $d = 390\,\mathrm{mm}$, and calculated the magnetic field contribution from a single loop:

$$B_{\text{loop}} \approx 0.15\,\mu\text{G/mA} \tag{5.10}$$

This result indicates that the effect of each individual hole rerouting is negligible when compared to the overall magnetic field. However, the cumulative effect of multiple reroutings necessitated a more comprehensive analysis. The coil design incorporates approximately 40 holes, each requiring 2 to 4 wire reroutings. Although many of these contributions are on opposite surfaces and might cancel with each other, the total effect of these reroutings has the potential to exceed our design goal of $1\,\mu$G/mA field uniformity. Thus, we performed detailed simulations to accurately model the exact design of the ACME III coil, including the collective effect of all reroutings and discrete wire configurations.

5.2.3 Coil simulations

To validate our coil design and assess its performance, we employed the Radia software package [167] for simulating the magnetic field distribution in free space. This simulation, based on the boundary-integral method, serves as a complementary approach to the finite-element method used in our initial design phase. Compared with the finite element method conducted in COMSOL, demonstrated significantly higher computational efficiency, but exhibits limitations in handling complex ferromagnetic material configurations. Consequently, we primarily employed boundary-integral method when assessing the free-space field, while switched to finite-element method when we realized the field with the shield is the key. We conducted parallel simulations using identical geometric models and found agreement between these computational methods, with discrepancies consistently below 0.5%. The comprehensive simulation model, which incorporates all wire reroutings, is depicted in Figure 5.5(d).

The simulated field distribution, presented in Figures 5.6, demonstrates the effectiveness of our design. By combining the inner and outer coils, we achieved a uniform magnetic field of approximately $256.6\,\mu$G/mA within the target volume. As we are targeting at $B_z \sim 100\,\mu$G in ACME III (see Section 4.1), the applied current should be around 0.39 mA. Our analysis revealed that without considering wire reroutings, the field uniformity was within $0.8\,\mu$G/mA throughout the spin-precession volume. The cumulative effect of all hole reroutings resulted in an increased $1.06\,\mu$G/mA inhomogeneity to the field, which is relatively insignificant. This minimal impact can be attributed to the fact that holes pass through both the inner and outer surfaces of the coil. As the currents flowing on these surfaces are in opposite directions, the fields generated by the reroutings largely cancel each other, mitigating their overall effect on field uniformity. Fields on the x and y axes were both found to be less than $10^{-3}\,\mu$G/mA in simulations throughout the spin-precession volume.

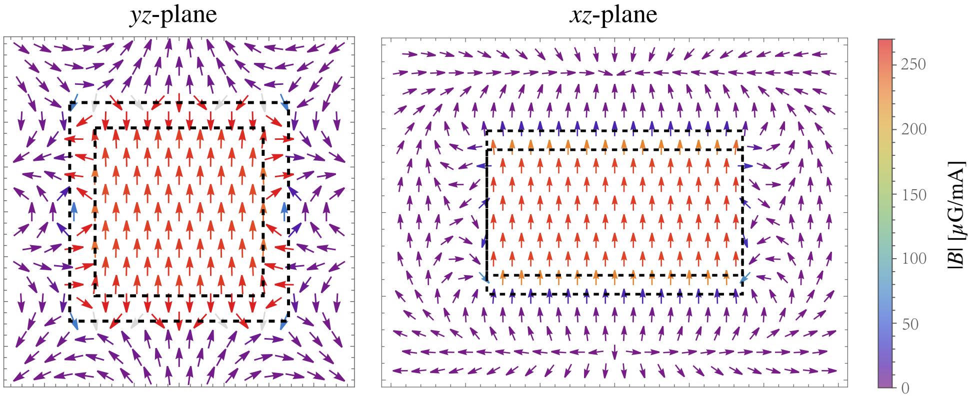

Figure 5.6: **Simulated z coil field distribution.** Fields are shown in (a) yz-plane and (b) xz-plane.

The self-shielding capabilities of our coil design were further validated through the analysis presented in Figure 5.7. The maximum fringe field was measured at approximately $13.2\,\mu$G/mA

(Table 5.1), primarily resulting from flux leakage around wire reroutings near holes on the side surfaces. The fringe field on the front and back surfaces coincides with the pivot point for current direction reversal between the top and bottom halves of the outer coil (Figure 5.4), but still maintains mostly below $10\,\mu$G/mA.

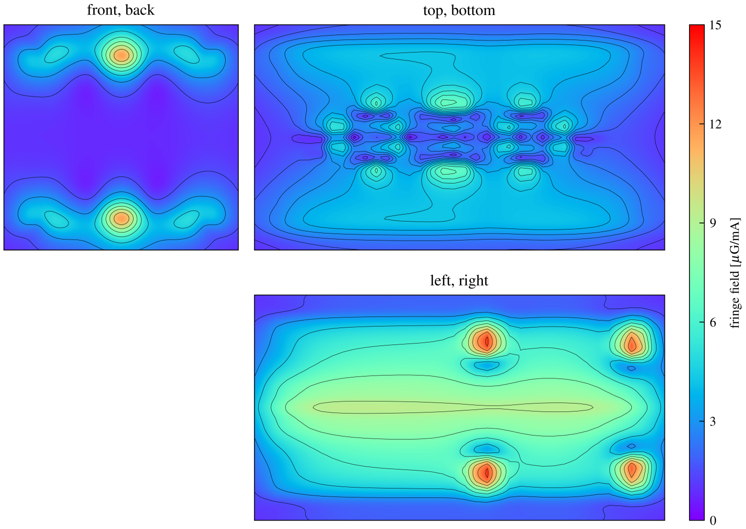

Figure 5.7: **The field distribution at the location of inner-layer mu-metal shield.** $|B|$ was shown when applying 1mA in the spin precession region: top/bottom faces, side faces, front/back faces.

The mean fringe field of $3.4\,\mu$G/mA represents only 1.3% of the applied field in the spin-precession volume. This marks a significant improvement over previous designs, such as the ACME II cosine-θ coil ($\sim 40\%$) and the ACME III coil geometry without self-shielding ($\sim 35\%$). Our design effectively reduces the total magnetic flux that could potentially magnetize external mu-metal layers by a factor of approximately 30. Even when considering maximum fields, our self-shielding design exhibits a mere 5.3% fringe field compared to 78% in ACME II.

These results underscore the efficacy of our self-shielding coil design in producing uniform field and minimizing exterior fringe fields at the design stage, setting the stage for the successful construction and implementation in the ACME III experiment.

shield face	**max field**	**mean field**
top/bottom	5	2.8
sides	13.2	5.0
front/back	11	3.1
overall	**13.2**	**3.4**

Table 5.1: **Fringe magnetic field produced by coils at each shield face.** Values are in μG per 1 mA of current supplied to the coil. Holes and reroutings are considered.

5.2.4 Implementation

The realization of our coil design necessitated meticulous attention to material selection and construction techniques to ensure optimal performance and minimal magnetic interference. The coil assembly was fabricated using high-density polyethylene (HDPE) sheets mounted onto non-magnetic aluminum extrusion frames. Aluminum and titanium fasteners were exclusively used to secure the components.

Precision-milled grooves in the HDPE sheets, whose locations were determined through our comprehensive simulations, serve as pathways for the wire windings. Insulated solid copper wire was carefully inserted into these grooves, achieving a tight fit that ensures positional stability of the windings. The assembly comprises the outer and inner z coils, each constructed on separate aluminum-extrusion frames. These frames are mounted on a common experimental table, providing structural fixture while maintaining precise alignment. All auxiliary coils, described in Section 5.1.2, are attached to the inner coil frame. Figure 5.8 illustrates both a mockup of the coil assembly design and the final constructed apparatus.

The coil system incorporates various wire gauges and groove specifications to accommodate different field requirements. Single-loop coils, responsible for generating B_z and B_x fields, utilize 1/16 inch wide grooves and are wound with 18 AWG wire. In contrast, coils requiring multiple turns, specifically those generating B_y and $\partial B_z/\partial x$ fields, are seated in 1/8 inch grooves and

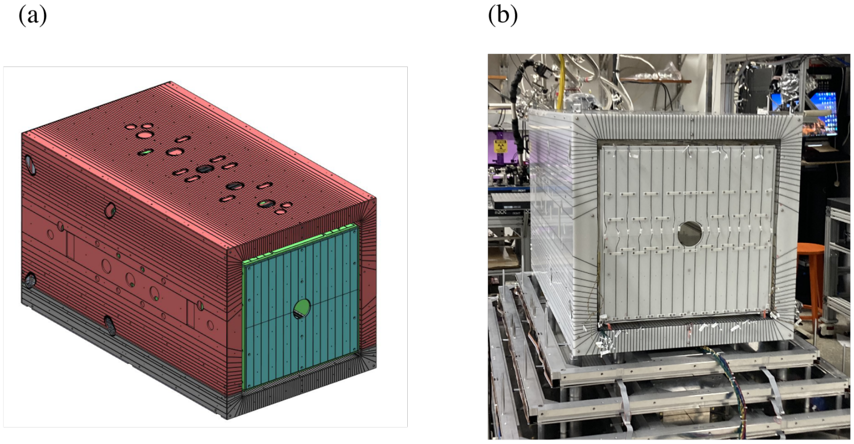

Figure 5.8: The CAD model (a) and the picture of the coil as constructed in the lab (b).

wrapped with 24 AWG enameled wire. To ensure the wires remain securely in place, we implemented HDPE clamps throughout the assembly.

Given the coil's location within a magnetically shielded volume, we implemented stringent material selection criteria. Every component of the coil assembly, including frames, HDPE sheets, screws, wires, and electrical connectors, underwent rigorous testing to verify their non-magnetic properties, confirmed with less than $1\,\mu$G field disturbance when brought in proximity (< 3 cm) with a QuSpin QZFM magnetometer.

A key feature of our coil assembly design is its modularity. The top and side sections of both the inner and outer coils can be lifted as a single unit, facilitating easy access to the interior volume of the coil. This design consideration significantly enhances the maintainability and adaptability of the experimental setup. To maintain electrical continuity between the top and bottom sections of the coil when assembled, we employed a set of non-magnetic connectors (SPHD-001T-P0.5 and SPAL-001T-P0.5).

The precision current supply for the coil system is provided by a combination of high-performance sources. Four SRS CS-580 current sources are utilized for generating B_z, B_y, and $\partial B_z/\partial x$ fields, while a GPP4323 current supply is dedicated to the B_x field. To ensure clean, stable current delivery, the supply lines incorporate 500 Hz low-pass filters, effectively reducing high-frequency noise. Continuous current monitoring is achieved through precision $1\,\Omega$ resistors integrated into each supply channel. Current distribution to various coil components is managed by a custom-designed relay box. This control system consists of two 32-channel relay boards (Numato 32ETHRL001) interfaced with a computer via Ethernet connection. This setup allows for fast, programmable control over the activation of individual coil elements, enhancing the flexibility and reproducibility of our experimental protocols. The outer main coil exhibits a resistance of $18\,\Omega$, while the inner main coil has a resistance of $3.2\,\Omega$.

5.3 Main coil characterization

5.3.1 Free space field uniformity

Following the construction of the main z coil, a comprehensive field characterization was first conducted in lab environment to assess its performance. To eliminate the influences of ambient magnetic fields, field fluctuations, drifts, and potential offsets in magnetometer readings, we employed a lock-in measurement technique. The drive current for the coil was modulated as a sinusoidal wave with frequencies ranging from 0.5 Hz to 5 Hz and an amplitude of 1 mA. This approach allowed us to isolate the field produced exclusively by our coil by measuring the amplitude of the sinusoidal signal at the corresponding frequency using magnetometers positioned at various locations.

For the primary sensor in our free-space field characterization, we selected the Twinleaf VMR magnetometer from among the various magnetic sensors described in Section 4.7.1. This choice was motivated by several factors. Firstly, the Twinleaf VMR is capable of operating effectively in the typical Earth's magnetic field strength of several hundred mG. Secondly, its magnetoresistive working principle results in minimal cross-talk between sensors placed in close proximity. Additionally, the relatively compact size of these sensors enabled us to deploy an array of five Twinleaf VMR sensors within the spin-precession volume, equally spaced over the range $z \in [-3, 3]$ cm, fully encompassing the width of the ThO beam.

To obtain a comprehensive field distribution map of the spin-precession volume, we scanned the sensor array along the x direction. However, as detailed in Section 4.7.1, the gain factor of the Twinleaf VMR is not precisely calibrated by the manufacturer, potentially leading to errors in absolute field readings as large as 20%. To address this limitation, we implemented a separate calibration procedure prior to our field characterization measurements. This calibration process allowed us to determine accurate gain factors for each sensor, significantly reducing the error in field readings to approximately 0.5%. Notably, we observed that these calibration factors remained stable throughout the entire course of our experiment.

Our scan along the x direction consisted of 35 distinct measurement points, with a spacing of 3 cm between adjacent points. At each measurement location, the sensor array was allowed to collect data for a duration of 20 seconds, ensuring sufficient statistical robustness in our results. Concurrent with the magnetic field measurements, we recorded the supply current by monitoring the voltage drop across a precision shunt resistor. The amplitude of the sinusoidal field signal was then calculated using the same lock-in computation technique, with the supply current serving as the reference signal.

This lock-in approach can be mathematically expressed as follows:

$$B_{\text{amp}} = \frac{1}{T} \int_0^T B(t) \cdot I(t) dt \tag{5.11}$$

Where $I(t) = I_0 \sin(\omega_0 t)$ is the supplied current and T is the data integration time, chosen to be

20 s for our case. This calculation assumes that the field produced by the coil is in phase with the supplied current, which is true for any frequencies below 200 Hz, limited by the bandwidth of Twinleaf magnetometers. The resulted B_{amp} is stable within 0.02 mG for each measurement point on any sensor. We then correct the each B_{amp} by multiplying the corresponding calibration factor to obtain the actual field strength at each point.

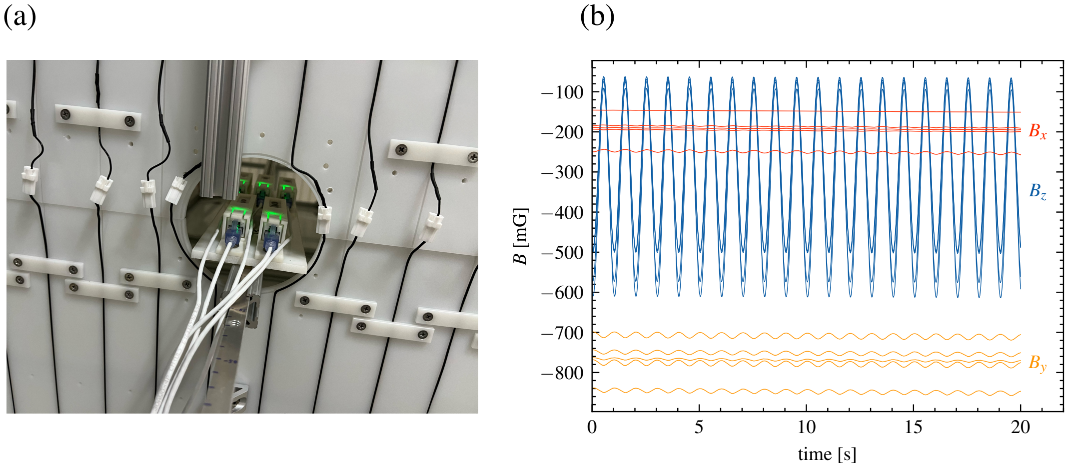

Figure 5.9: **Magnetic field from a sinusoidally modulated supply current on main z coil.** (a) The Twinleaf sensor array that was inserted to the spin-precession volume. (b) The sensor readings at $x = 0$ and $I_0 = 1$ mA. The field amplitude is mostly significant on z direction.

The comprehensive field distribution measurements, as depicted in Figure 5.10, reveal the precise magnetic field characteristics of our main z coil design. As intended, the generated field is predominantly aligned along the z direction, exhibiting a gain factor of $B_z = 257.2\,\mu$G/mA. This experimental value demonstrates remarkable agreement with our simulated prediction of $B_z = 256.6\,\mu$G/mA, showing a discrepancy of merely 0.2%. Such close correspondence between theoretical predictions and empirical measurements validates the accuracy of our simulation methodologies and the precision of our construction techniques.

A critical parameter for the performance of our experimental apparatus is the field uniformity

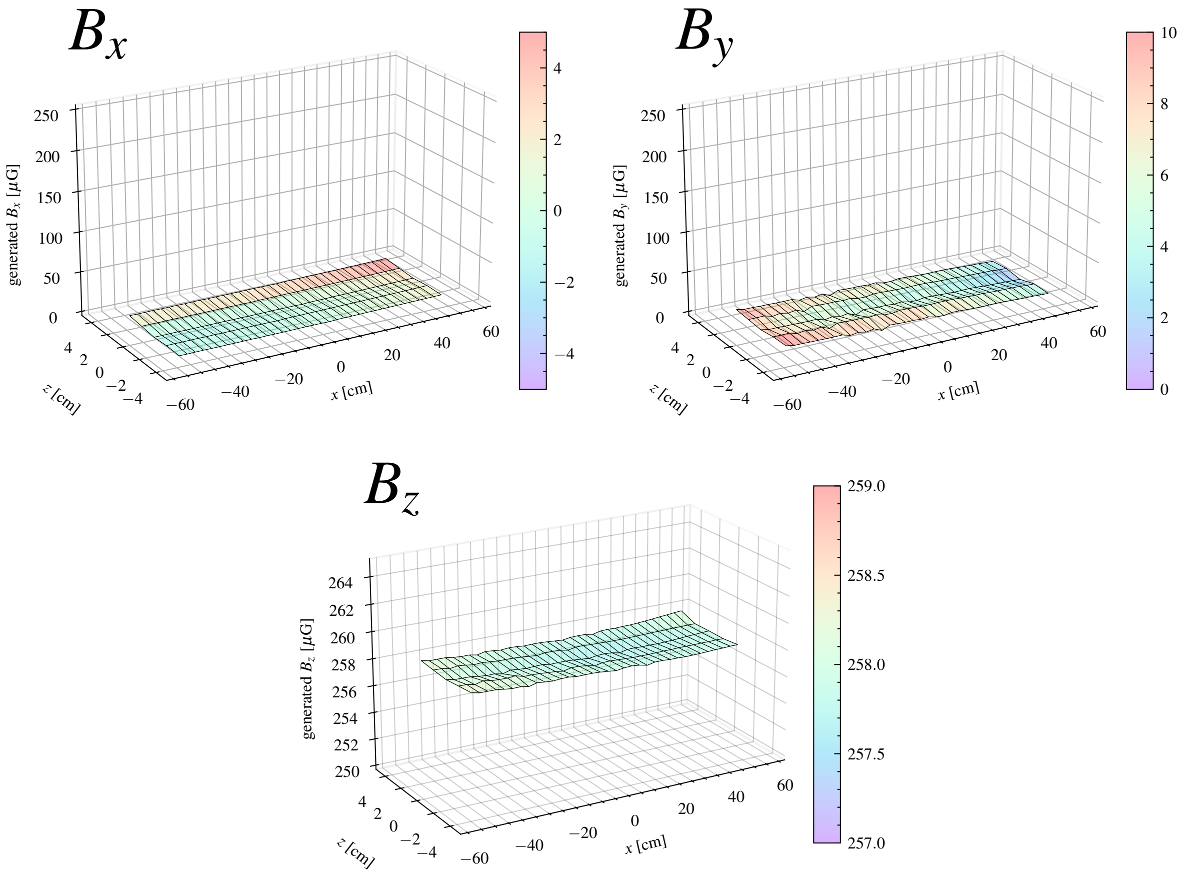

Figure 5.10: **Measured magnetic field distribution for the main z coil on xz plane.**

within the spin-precession volume. Our measurements reveal that the field uniformity is maintained within $0.8\,\mu$G/mA throughout this crucial region. This variation represents only 0.31$\%$ of the applied field, a result that aligns closely with our simulation predictions. To contextualize this achievement, it's important to note that our design goal for field uniformity was set at $10\,\mu$G/mA. The negligible contribution of the main coil to magnetic field gradients means that any field inhomogeneities experienced by the ThO molecules will be predominantly due to residual fields from the magnetic shielding rather than from the coil itself. This characteristic greatly simplifies the analysis of experimental data and enhances our ability to isolate and study the systematic uncertainties.

To provide a comprehensive view of the field distribution, Figure 5.11 presents a comparison between the measured and simulated B_z field distributions along the x, y, and z axes. This multi-axis comparison not only demonstrates the three-dimensional uniformity of our field but also further validates the accuracy of our simulation models.

While the coil was designed to generate a field primarily along the z axis, our measurements also detected minor field components in the x and y directions. The maximum observed values for these orthogonal components were $B_x = 1.7\,\mu$G/mA and $B_y = 3.0\,\mu$G/mA, respectively. These small transverse field components, while higher than simulated results, are significantly smaller than the primary z direction field. These unexpected field components may be attributed to assembly tolerances in the coil construction and misalignments between the coil and sensor axes.

Taking the maximum values of B_x and B_y into account, we can infer a misalignment of approximately 0.8° between the magnetic field and the z coordinate. In the context of the ACME experiment, the z coordinate is defined as the direction of the $\vec{E}$ field. This slight misalignment introduces a magnetic field component normal to the z axis, which may give rise to systematic effects when coupled with the quadratic Stark effect. To evaluate the potential impact of this

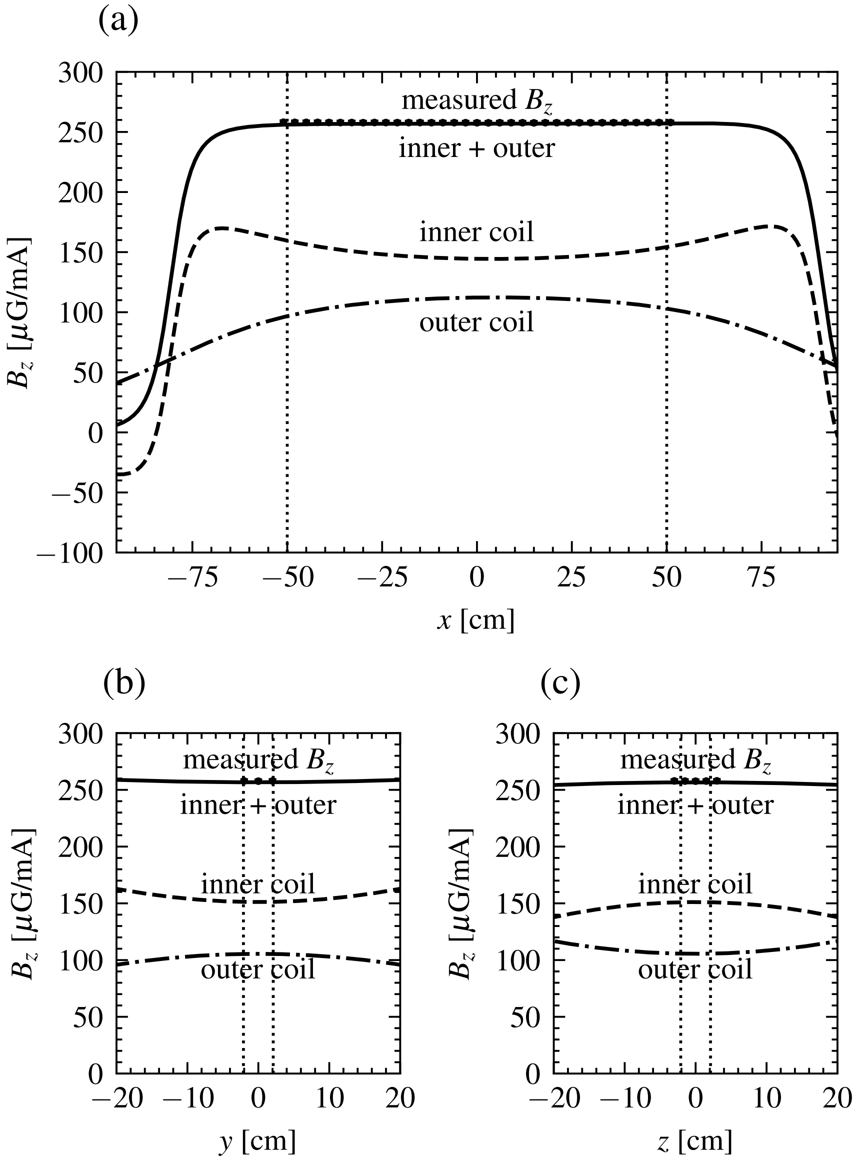

Figure 5.11: **The measured main z coil field comparing with simulation results.** (a), (b), (c) shows the field component B_z on x, y, z axis, respectively. Measured free-space coil field are shown as black data points comparing with simulated curves in the graph.

misalignment, we follow the discussing elucidated by [61]. The energy shift resulting from this misalignment can be expressed as:

$$\delta E \cong 2 g_F \mu_B \left(B_z - \frac{1}{2} \left(\frac{g \mu_B B_z}{\Delta} \right)^2 \frac{B_y^2 + \frac{\mathcal{E}^2 v^2}{c^2} + 2 \frac{\mathcal{E} v}{c} B_y}{|B_z|} \right) \tag{5.12}$$

In this equation, g_F represents the g-factor of the corresponding state, μ_B is the Bohr magneton, B_z denotes the magnetic field parallel to the molecule polarization axis, and B_y signifies the total field perpendicular to the molecule polarization axis. Additionally, $\mathcal{E}$ represents the applied electric field, with $\Delta \propto \mathcal{E}^2$ being the quadratic Stark shift, and v is the speed of the molecular beam.

The first term on the right-hand side of the equation corresponds to the Zeeman shift, which is directly influenced by B_z. The second term, often referred to as the motional magnetic field shift, is suppressed by the square factor $\frac{g\mu_B B_z}{\Delta}$. This factor represents the ratio of the Zeeman shift to the Stark shift. For ThO molecules in the H state, under nominal experimental conditions of $B_z \sim 100\,\mu$G and $|\mathcal{E}| \sim 100$ V/cm, this factor is approximately $(10^{-9})^2 = 10^{-18}$. The magnitude of this suppression factor is crucial, as it effectively mitigates the influence of the off-axis field component to a level well below the detection sensitivity of the ACME III experiment. To put this into perspective, the shot-limit sensitivity of the ACME III experiment is only 10^{-7} of the nominal Zeeman shift. Consequently, the systematic effects arising from the slight misalignment of the magnetic field are rendered negligible within the context of the experiment's precision capabilities.

5.3.2 Field confinement

The confinement of the magnetic field within the boundaries of the main coil is also a crucial aspect of its performance. To directly verify the effectiveness of this self-shielding feature, we conducted measurements of the fringe field magnitude at the location of the shields, positioned about 9.4 cm from the outer surface of the coil. The same sinusoidal modulating procedure was used for the supply current, allowing us to isolate and measure the fringe field produced exclusively by the main coil. Figure 5.12 illustrates the fringe field distribution at the location of the inner-layer shield. We employed a uniform 5×5 measurement grid on each accessible face of the coil. It should be noted that the field on the bottom face was not evaluated due to physical constraints in accessing the area beneath the apparatus. However, given the symmetry of the coil geometry along the xz plane, we anticipate that the field distribution on the bottom face would closely mirror that of the top face.

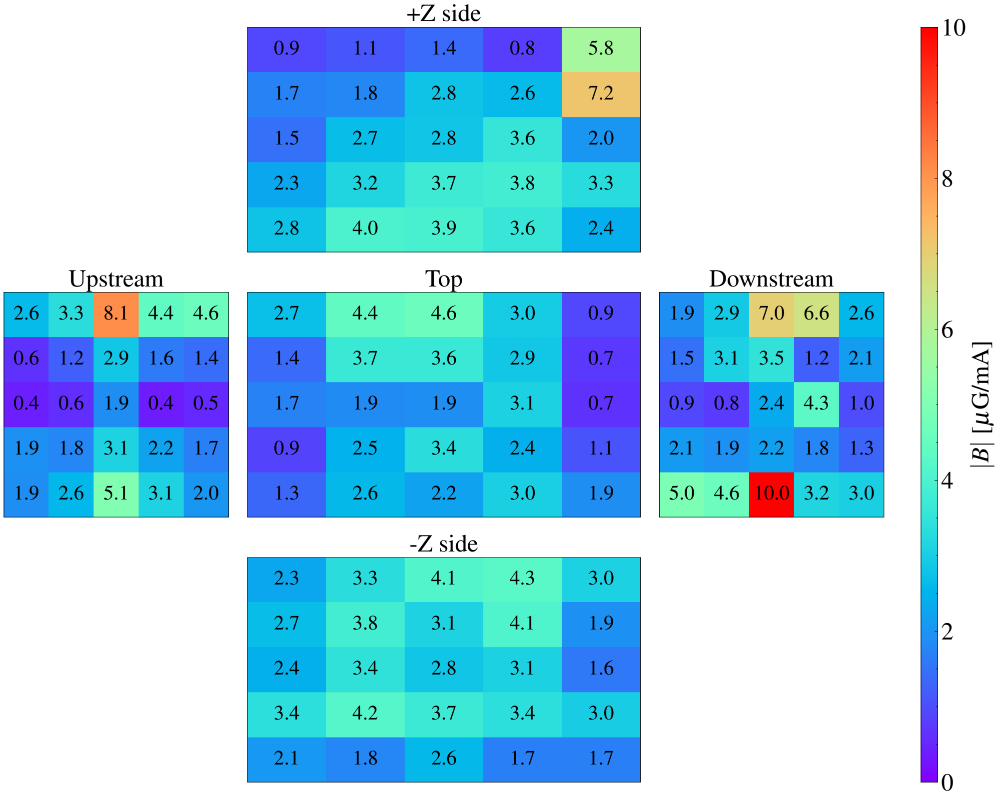

+Z side

0.9	1.1	1.4	0.8	5.8
1.7	1.8	2.8	2.6	7.2
1.5	2.7	2.8	3.6	2.0
2.3	3.2	3.7	3.8	3.3
2.8	4.0	3.9	3.6	2.4

Upstream

2.6	3.3	8.1	4.4	4.6
0.6	1.2	2.9	1.6	1.4
0.4	0.6	1.9	0.4	0.5
1.9	1.8	3.1	2.2	1.7
1.9	2.6	5.1	3.1	2.0

Top

2.7	4.4	4.6	3.0	0.9
1.4	3.7	3.6	2.9	0.7
1.7	1.9	1.9	3.1	0.7
0.9	2.5	3.4	2.4	1.1
1.3	2.6	2.2	3.0	1.9

Downstream

1.9	2.9	7.0	6.6	2.6
1.5	3.1	3.5	1.2	2.1
0.9	0.8	2.4	4.3	1.0
2.1	1.9	2.2	1.8	1.3
5.0	4.6	10.0	3.2	3.0

-Z side

2.3	3.3	4.1	4.3	3.0
2.7	3.8	3.1	4.1	1.9
2.4	3.4	2.8	3.1	1.6
3.4	4.2	3.7	3.4	3.0
2.1	1.8	2.6	1.7	1.7

Figure 5.12: **The field distribution at the location of inner-layer mu-metal shield.** a grid of 5×5 points are scanned along x and y direction, and the field is measured at $z = 9.4$cm. The field is shown in x and y direction.

The observed fringe field distribution demonstrates qualitative agreement with our simulation results, as depicted in Figure 5.7. Notably, the maximum fringe field occurs at the front and back faces, specifically near the pivot points where the current direction reverses between the top and bottom halves of the outer coil. Quantitatively, we measured a maximum fringe field amplitude of $\sim 10\,\mu$G/mA, which corresponds to 3.9% of the field applied in the spin-precession volume, Agreeing with simulations. This result directly confirms the coil's effective self-shielding capabilities.

5.3.3 Coil characteristics with the presence of shields

To comprehensively validate the performance of the integrated magnetic field control system, including both the magnetic shields and the coil, we conducted field uniformity measurements in the presence of the magnetic shield. As illustrated in Figure 5.13, the measured field with the shield in place differs from the free-space field by a mere 0.4%. This minimal difference serves as a strong indicator that the fringe field outside the coil boundary is negligible.

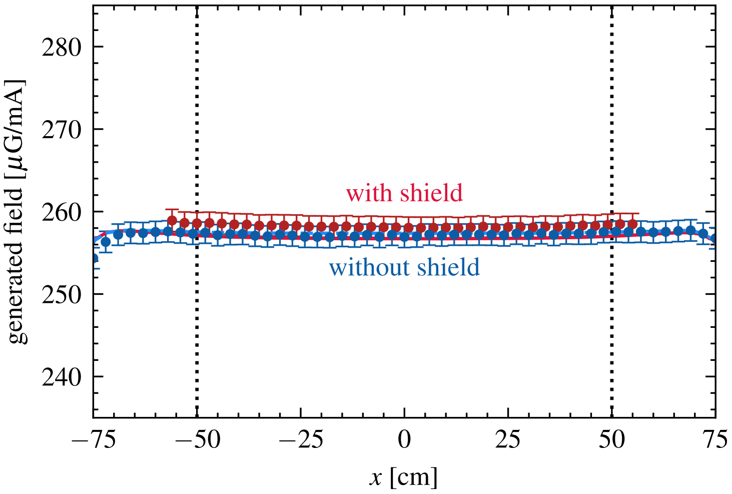

Figure 5.13: **Comparison of coil fields with/without shield.** The field applied by the main coil when the shield is present only increased by 0.4% compared to the free-space field, indicating minimum influence from the shield and thus effective self-shielding of the fringe field. Error-bars are assigned based on the standard deviation of the field measurements.

For context, we will demonstrate in Section 5.4.2 that coils lacking effective self-shielding typically experience a much more pronounced influence from the shield. This is because the shield enclosing the coil effectively functions as a return yoke for the magnetic flux. Generally, a coil with a return yoke produces larger field values compared to an identical coil without one. However, for our self-shielding z coil, this increase is minimal, underscoring the effectiveness of our self-shielding design, thus preventing the shield from being magnetized by the coil.

The inhomogeneity of the coil inside the shield was measured at 0.9 μG/mA, which remains virtually unchanged from its free-space value. This consistency further validates the robustness of our coil design and its performance within the shielded environment.

We also conducted a detailed investigation of any potential "build-up" process of residual fields in the spin-precession volume following the application of a magnetic field. Any irreversible magnetization of the magnetic shield induced by the main coil would manifest as a change in the residual field. Figure 5.14 (a) illustrates our findings when applying magnetic fields of various amplitudes and measuring the subsequent change in residual field at the spin-precession volume center. Notably, even for applied fields 100 times larger than the typical B_z value used in actual EDM measurements, the change in residual field remained consistent with zero, indicating no significant magnetization of the magnetic shield.

Figure 5.14 (b) presents the residual field change when a 2 mG field is applied and its direction reversed every 30 seconds, for varying numbers of cycles. Our results suggest that while magnetization does accumulate, it does so at a remarkably low rate of approximately 5 μG per 1000 cycles, equivalent to about 17 hours of operation. This observation not only demonstrates the build-up of magnetization but also highlights the stability of the residual field over the course of the measurement. Any observed residual field changes can be effectively eliminated by degaussing only the inner magnetic shield. The results presented in Figure 5.14 (b) suggest the possibility of

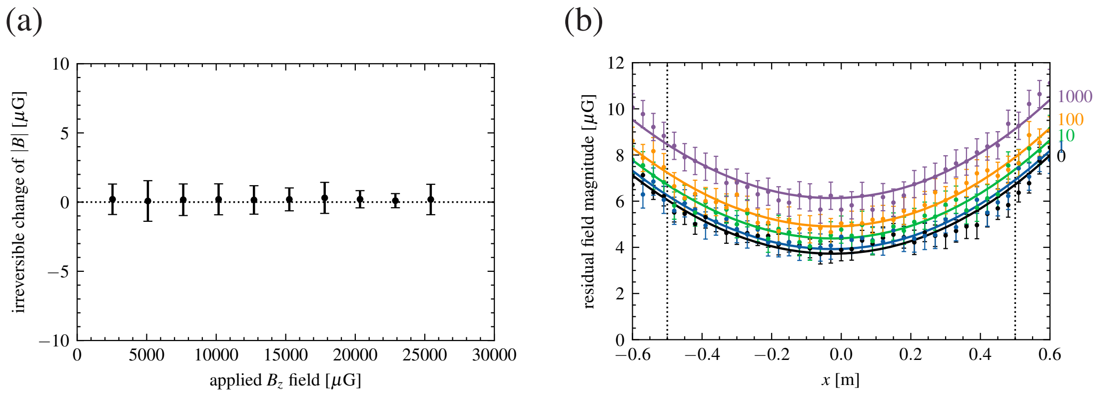

Figure 5.14: **Change of residual field after applying a magnetic field.** (a) Applying a magnetic field that is up to 100 times larger than the typical B_z field, the change of residual field is consistent with 0. (b) the residual field after the application of a 2 mG alternating field for 1, 10, 100 and 1000 cycles. Error-bars are assigned based on the standard deviation of the field measurements.

conducting measurements over extended periods of field switching without the need for frequent degaussing, thereby optimizing valuable measurement time.

5.4 Design and characterization of auxiliary Coils

5.4.1 dB_z/dz coil

The self-shielding z coil generates a highly uniform field in the spin-precession volume, as discussed in Section 5.3.1. We designed both the outer and the inner part of the main coil to be consisted with two halves that are separated horizontally, on $+z$ and $-z$ side, respectively. To generate a uniform field, both the $+z$ and $-z$ halves of the coil are connected in series and the same current is supplied to both halves. This design is also capable of generating a dB_z/dz field by reversing the current on the $-z$ half of the coil, which is realized by a relay that switches between two circuits that have opposite wiring polarities. The dB_z/dz field is depicted in Figure

5.15. As clearly seen, a uniform dB_z/dz gradient is generated, while the coil simutaneously generates dB_y/dy and dB_x/dx gradients. The dB_y/dy gradient is not explicitly seen on xz plane in this graph, but is confirmed through a separate probe along y axis.

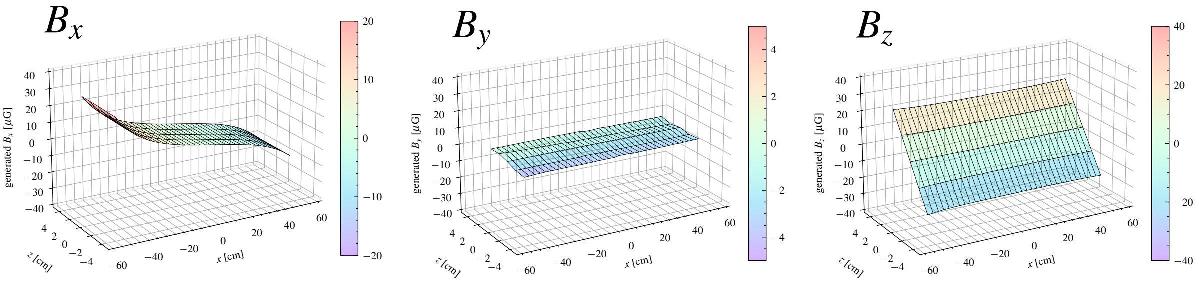

Figure 5.15: **Measured field distribution for dB_z/dz coil on xz plane.** dB_z/dz coil also generate dB_y/dy and dB_x/dx at the same time. The dB_y/dy gradient is not explicitly seen on xz plane but is confirmed through a separate probe along y axis.

Their values are:

$$
\begin{aligned}
\frac{dB_z}{dz} &= 7.78\,\mu\text{G/(mA}\cdot\text{cm)} \\
\frac{dB_y}{dy} &= -7.35\,\mu\text{G/(mA}\cdot\text{cm)} \\
\frac{dB_x}{dx} &= -0.45\,\mu\text{G/(mA}\cdot\text{cm)}
\end{aligned}
\tag{5.13}
$$

Their sum is very close to 0, which is consistent with $\nabla \cdot \mathbf{B} = 0$. The geometry of the main z coil is roughly translational-symmetric along x coordinate for the spin-precession volume, thus it is expected that the dB_z/dz coil primarily induce dB_y/dy, while little dB_x/dx would be generated alongside. All the other gradient components generated by the dB_z/dz coil are negligibly small. In contrast with the self-shielding feature when applying an uniform z field, the dB_z/dz coil loses the self-shielding feature even with the same coil geometry. The maximum fringe field for a 1mA applied current is $\sim 130\mu$G, which is more than 50% of the generated uniform field from the same amount of current.

5.4.2 B_x and dB_x/d_x coil

The long extent of the whole apparatus along x direction makes it a relatively straightforward task to generate a uniform B_x field. In the ACME III coil assembly, this is done by eight single-turn square loops around the inner coil frame (shown in green in Figure 5.2). During the assembling and disassembling stage, these square loops have to be split into two detachable segments on the side surface, one fixed to the upper half of the structure and one sticks to the bottom half. This strongly advocates the single-turn design to minimize the interconnections between segments.

The locations of the loops are $x = \pm 125, 370, 695, 705\,\mathrm{mm}$, primarily chosen to avoid intersections with any holes on the side, top and bottom faces of the inner coil, and to maintain the symmetry on the x coordinate respect to the spin-precession volume. The current on each loop is optimized in free space by a Radia simulation. To generate $B_x = 1\mu\mathrm{G}$ uniform field, the optimized current vector is:

$$I = [23.2, 20.2, 22.1, 20.6, 20.6, 22.1, 20.2, 23.2]\,\mu\mathrm{A} \tag{5.14}$$

The supplied current is symmetric between $+x$ and $-x$ part of the coil. Of course, these currents can be proportionally scaled to produce arbitrary values of B_x field. This field is confirmed by the measurement in free space, seen in Figure 5.16. The uniformity of the free-space field is within 2.3%. However, once we put the shield on that encloses the coil, the field is changed significantly. The mean field is increased by 12% and the maximum field variation is increased to 17%. This is due to the fact that the B_x coil is not self-shielded, the field generated by the coil is significantly influenced by the enclosing shield. The asymmetric potisioning of the magnetic shield relative to the B_x coil also causes significant field gradient between $-x$ and $+x$ side of the spin-precession volume.

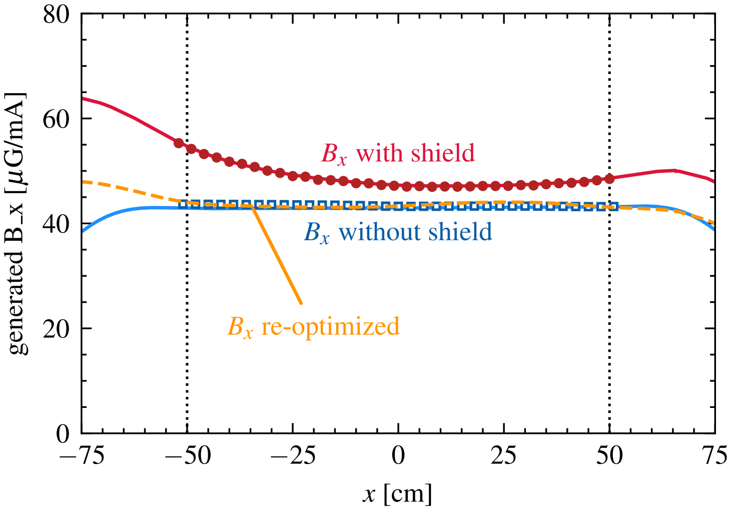

Figure 5.16: **Measured and simulated field distribution for x coil on central beamline.** The field with shield, without shield, and the result for re-optimized supply currents for the shielded coil are shown.

For the case of the B_x field with shield enclosed around the coil, it is possible to adjust the supply current vector to compensate the field distortion and result in a field with higher uniformity. A tentative optimization of the supply current for B_x field in is performed by COMSOL with Nelder-Mead optimization algorithm, and is shown in orange curves in Figure 5.16. The re-optimized field has a significantly improved uniformity of 0.77% in the spin-precession volume, with the following current vector:

$$I = [23.8, 4.3, 21.7, 19.3, 19.1, 21.7, 11.0, 24.6]\,\mu\text{A} \tag{5.15}$$

This current vector is not symmetric between $+x$ and $-x$ side of the coil, and requires additional current supply channels to x coil. Relevant hardware upgrade is currently underway at the time of completion of this thesis. We observed that this optimization result is independent of shield parameters, including the permeability and the residual magnetization of the shielding layers. In this case, the shielding layers can be approximated as a perfect permeation layer of magnetic field and its influence converges to a certain value.

In principle, this field can be optimized to cancel any B_x component of the residual field in the spin-precession region with high precision using the same method. More robust optimization algorithms, such as Genetic Algorithm or Deep Neural Networks, can be used to further improve the performance of the field optimization.

By reversing the current direction on the $-x$ side of the B_x coil, a linear dB_x/dx gradient can be generated. The optimized current vector for producing $dB_x/dx = 1\mu$G/cm is:

$$I = [-1890, -1890, -849, -302, 302, 849, 1890, 1890]\,\mu\text{A} \tag{5.16}$$

These currents can be proportionally scaled to produce arbitrary values of dB_x/dx field. The field is depicted in Figure 5.17. A uniform dB_x/dx gradient is generated, while the coil simutaneously generates dB_y/dy and dB_z/dz gradients. We expect the dB_y/dy and dB_z/dz generated by the dB_x/dx coil are roughly of the same amount, because the coil is invariant under rotations by $90°$ around x axis, which makes the coil geometry equivalent on $\hat{y}$ and $\hat{z}$ axes. The measured values agree with this expectation:

$$\begin{aligned}\frac{dB_x}{dx} &= 0.55\,\mu\text{G/(mA}\cdot\text{cm)}\\ \frac{dB_y}{dy} &= -0.31\,\mu\text{G/(mA}\cdot\text{cm)}\\ \frac{dB_z}{dz} &= -0.26\,\mu\text{G/(mA}\cdot\text{cm)}\end{aligned} \tag{5.17}$$

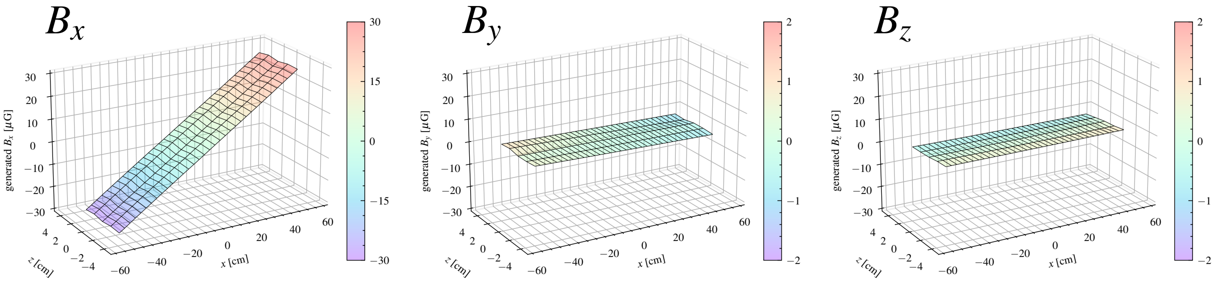

Figure 5.17: **Measured field distribution for dB_x/dx coil on xz plane.** dB_x/dx coil also generate dB_y/dy and dB_z/dz at the same time.

5.4.3 B_y and dB_y/dx, dB_y/dy, dB_y/dz coil

The magnetic field on another transverse direction, B_y, could be generated using the same self-shielding design as the main z coil. However, the B_y field is not required during the measurement of the electron EDM, its purpose is to study the systematic effects on electron EDM that are sensitive to the B_y field, as well as potentially cancelling residual field along $\hat{y}$ direction. Thus, we adopted a simpler and more flexible design for the B_y coil, which follows the the idea of using square loops and shims to generate field. By reversing the current some part of the coil, dB_y/dx, dB_y/dy and dB_y/dz can be independently generated. It is shown in Figure 5.18 (a), and also as the blue coil in Figure 5.2.

The y coil is located on the xz plane with $y = \pm 350$ mm. On each plane, there is a square loop of 1576 mm by 326 mm (x dimension and z dimension) 'center' coil, and two square loops of 383 mm by 326 mm 'side coil' to shim the field far from the center on $\hat{x}$ direction. There are also four 'patch coil' on the four corners of each plane, to further shim the field on the far region in $\hat{x}$ and $\hat{z}$ direction. Each patch coil consists of a 3×20 grid of square loops with 36 mm × 43 mm each, with the number of turns on each grid optimized to minimize the B_y field inhomogeneity in the spin-precession volume by Radia simulation, and is shown in Figure 5.18 (b). The 'center' coil

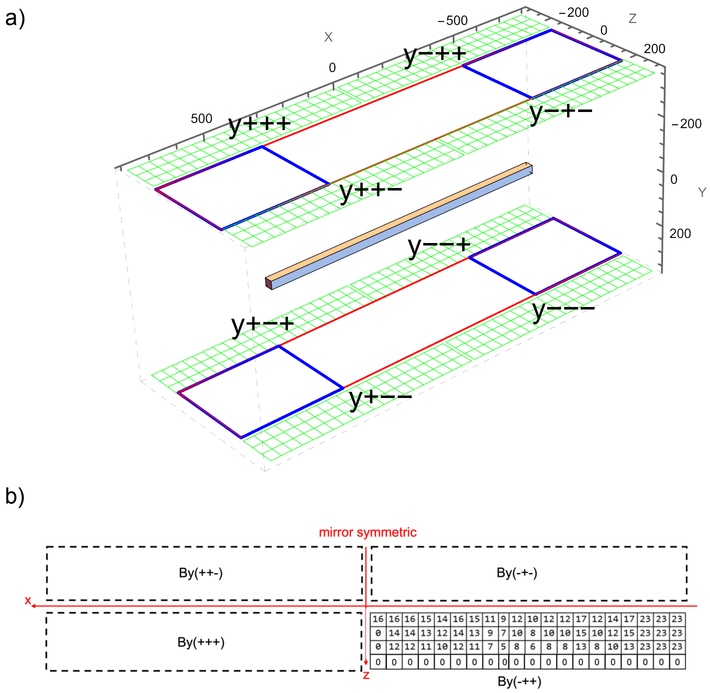

16	16	16	15	14	16	15	11	9	12	10	12	12	17	12	14	17	23	23	23
0	14	14	13	12	14	13	9	7	10	8	10	10	15	10	12	15	23	23	23
0	12	12	11	10	12	11	7	5	8	6	8	8	13	8	10	13	23	23	23
0	0	0	0	0	0	0	0	0	0	0	0	0	0	0	0	0	0	0	0

Figure 5.18: **The schematics for B_y coil.** (a) the B_y coil consists of a pair of 'center' coils (red), two pairs of'side' coils (blue) and eight 'patch' coils (green). The box-shaped spin-precession volume is also shown. (b) Number of turns on each grid of the patch coil, optimized so that the B_y field inhomogeneity is minimized.

have 5 turns and 'side' coil have 10 turns each. Table 5.2 shows the mode of operation and the corresponding components to activate for the B_y coil. (-) in the table indicates that the polarity of the current is reversed respect to the coordinate which the field gradient is on.

Mode	Lattice coils	Center coils	Side coils
uniform $\mathcal{B}_y$	On (+)	On (+)	Off
$\partial\mathcal{B}_y/\partial x$	On (-)	Off	On (-)
$\partial\mathcal{B}_y/\partial y$	On (-)	On (-)	Off
$\partial\mathcal{B}_y/\partial z$	On (-)	Off	Off

Table 5.2: **The mode of operation for the B_y coil.**"(-)" indicates that the polarity for the coil component is reversed for gererating certain gradients.

The field generated by the B_y coil is shown in Figure 5.19. Just as B_x, distribution of B_y field is significantly distorted by the enclosing shield because of the lack of self-shielding design. The asymmetric positioning of the magnetic shield relative to the B_y coil also causes significant linear field gradient in $\hat{x}$. The field and the uniformity of the free-space field is $72.5\,\mu$G/mA and 4.95%, respectively. These numbers increased to $111\,\mu$G/mA and 11.0% for the case with shield.

With the technique mentioned in section 5.4.2, the shielded field uniformity can be improved by a re-optimization of the ratio of the supply currents between the center coils, side coils, and patch coils. While $I_{\text{side}} = -0.197 I_{\text{patch}}$ and $I_{\text{center}} = -0.123 I_{\text{patch}}$, the minimum field inhomogeneity of 4.8% is achieved, although at the cost of a slightly reduced field strength of $49.7\,\mu$G/mA. Supplying independent currents to each of the center, side and patch coil may result in a further improvement of the field uniformity, and the work is currently underway at the time of completion of this thesis.

The three gradient modes generated by the B_y coil are characterized and shown in Figure 5.20. The gradient dB_y/dx, together with its Maxwell counterpart dB_x/dy, is generated when the current is supplied on the four side coils and eight patch coils, with current supply for the $-x$ side reversed:

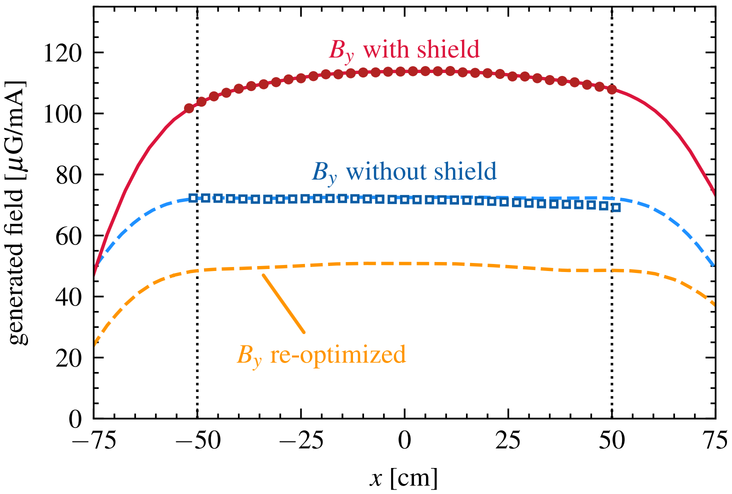

Figure 5.19: **Measured and simulated field distribution for B_y coil on central beamline.** The field with shield, without shield, and the result for re-optimized supply currents for the shielded coil are shown.

$$\frac{dB_y}{dx} = \frac{dB_x}{dy} = 2.1\,\mu\text{G/(mA}\cdot\text{cm)} \tag{5.18}$$

dB_y/dy is generated when the current is supplied on the two center coils and eight patch coils, with current supply for the $-y$ side reversed. This should also generate dB_x/dx and dB_z/dz at the same time. Given that the extent of the blue coils on x coordinate is roughly 2.6 times as it is on z coordinate, we expect that the produced dB_z/dz in this mode is roughly 2.6 times of dB_x/dx. The simulation and the measurement both gives:

$$\begin{aligned} \frac{dB_y}{dy} &= 1.81\,\mu\text{G/(mA}\cdot\text{cm)} \\ \frac{dB_x}{dx} &= -0.41\,\mu\text{G/(mA}\cdot\text{cm)} \\ \frac{dB_z}{dz} &= -1.40\,\mu\text{G/(mA}\cdot\text{cm)} \end{aligned} \tag{5.19}$$

This satisfies the Maxwell's equation of $\nabla\cdot\mathbf{B} = 0$.

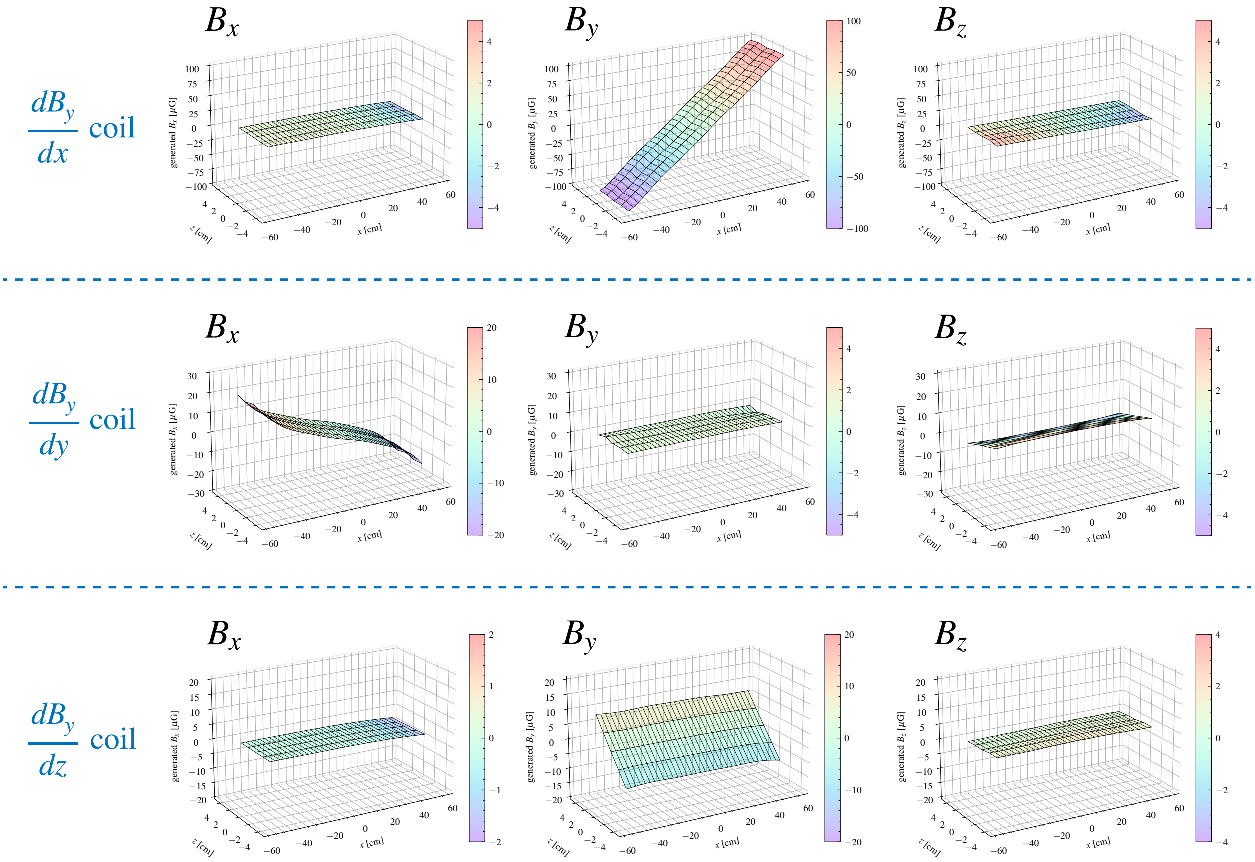

Figure 5.20: **The gradients generated by B_y coil.** For each gradient mode, the field distribution of B_x, B_y and B_z on the xz plane are shown.

The gradient dB_y/dz, together with its Maxwell counterpart dB_z/dy, is generated when the current is supplied only on the eight patch coils, with current supply for the $-z$ side reversed. The simulation and the measurement both gives:

$$\frac{dB_y}{dz} = \frac{dB_z}{dy} = 3.0\,\mu\text{G/(mA} \cdot \text{cm)} \tag{5.20}$$

5.4.4 dB_z/dx coil

The last independent gradient to control is dB_z/dx. The idea for this coil is to use a couple of rectangular loops on the side faces of the inner coil to generate B_z that is opposite in direction on the $+x$ and $-x$ region. Shim coils are put on the far side on the $\hat{x}$ direction to reduce the field deviation from a linear gradient. In the ACME III coil assembly, the large rectangular loops have 8 turns of AWG24 enameled wires, and the shim coils have 16 turns of the same wire.

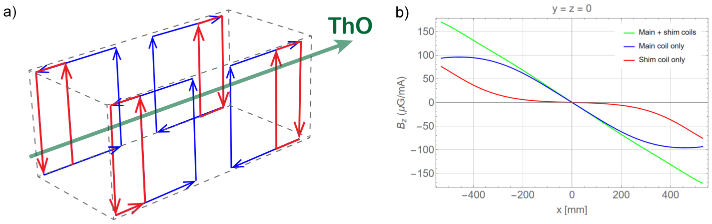

Figure 5.21: **The schematics for dB_z/dx coil.** (a) the dB_z/dx coil consists of two pairs of rectangular loop (blue) and two pairs of shim coils (red). (b) The field profile generated by each component on the central beamline.

The field for dB_z/dx coil is shown in Figure 5.21. This coil simutaneously generate the following two gradients:

$$\frac{dB_z}{dx} = \frac{dB_x}{dz} = 3.2\,\mu\text{G/(mA} \cdot \text{cm)} \tag{5.21}$$

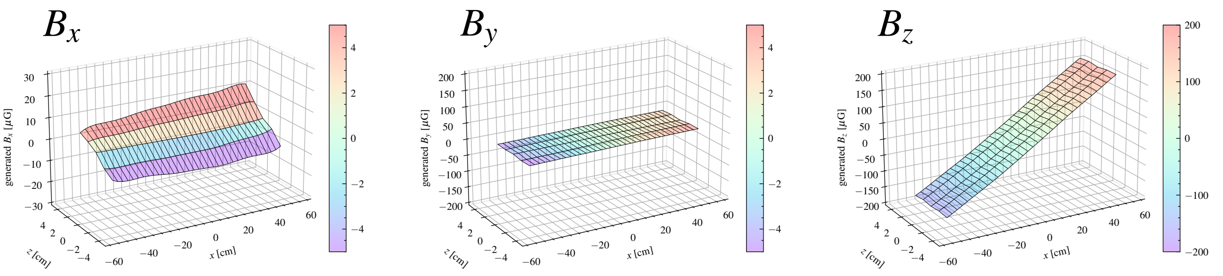

Figure 5.22: **Measured field distribution for dB_z/dx coil on xz plane.** dB_z/dx coil also generates dB_x/dz gradient with equal amount.

5.5 Summary

In conclusion, the next-generation coil system for ACME III electron EDM search has been designed, fabricated and tested. The main B_z coil is capable of applying a highly-uniform magnetic field over the large 1 m long spin-precession volume, with a field uniformity of 0.31%. Its self-shielding design suppresses the total fringe field to only 1.3% of the the field applied, a factor of 30 improvement compared with previous generations. This enables us to perform the spin precession measurement continuously without the need to degauss the shield for over tens of hours.

The auxiliary coils and the independent control of every gradient components enable the complete study of systematic effects of every magnetic field and gradient components in the entire spin-precession volume. A summary of all the gradient coil fields on the central beamline can be seen at Figure 5.23. The conversion factor of the gradients varies for different coils, but arbitrary field gradients can be generated by scaling the current supplied to each coil. Even for the dB_y/dy coil with the smallest gradient conversion factor, the coil system is capable to apply a field gradient as large as $100\,\mu$G/(mA $\cdot$ cm), more than ten times of the typical field gradient in any direction that the ThO molecules see during the electron EDM measurement. This also allow a precise control of the magnetic field inhomogeneity in the spin-precession volume, and active cancellation of ambient residual field to first order gradients were made possible.

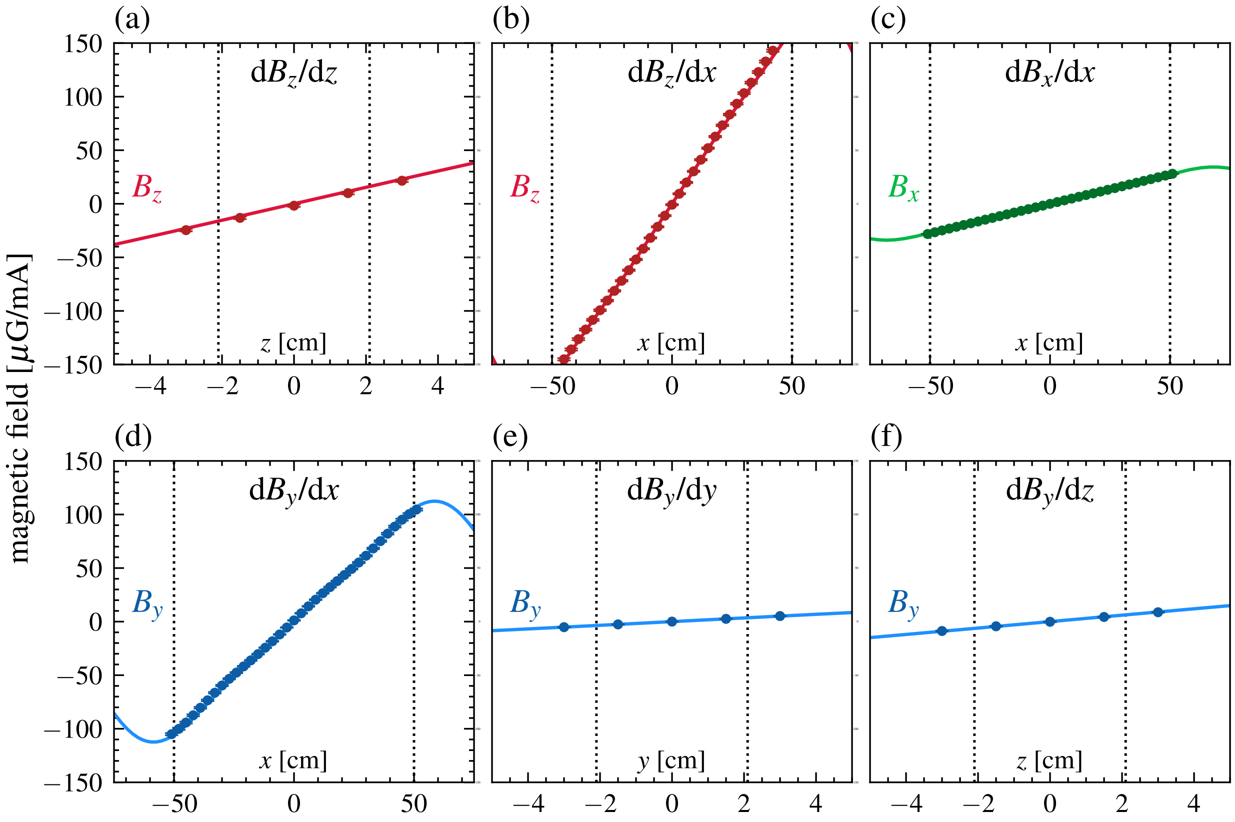

Figure 5.23: **Summary of all gradient fields on central beamline.** The fields are shown for (a) dB_z/dz, (b) dB_x/dx, (c) dB_x/dx, (d) dB_y/dx, (e) dB_y/dy, and (f) dB_y/dz coil. The conversion factor of the gradients varies for different coils, but arbitrary field gradients can be generated by scaling the current supplied to each coil.

CHAPTER 6

CONCLUSION AND OUTLOOK

This thesis chronicles the some of the experimental advancements that will make the ACME III electron EDM measurement possible that is 40 times more sensitive than ACME II. Chapter 1 introduced the theoretical motivations, fundamental methods for measuring the electron EDM, and the present status of the search in this field. Chapter 2 detailed the measurement methodologies and the apparatus of the ACME III experiment, with decent overlaps with the ACME I and II setups but also significant upgrades. Chapter 3 briefly examined the systematic and statistical uncertainties [101, 100, 82], with a focus on those associated with the magnetic field.

As of this writing, all major components of the new ACME III apparatus have been assembled and successfully tested at Northwestern University. This includes the ThO source, electrostatic lens, vacuum chamber, collection optics, SiPM detectors, electric field plates, magnetic shields, magnetic coils, and the associated laser systems. The ACME team is now characterizing the assembled apparatus and starting ThO measurements.

Chapters 4 and 5 describe two most significant research efforts that have been central to my work within ACME III. The first is the development of the new magnetic shielding system, the largest single apparatus component in ACME III, which suppressed the residual field more than ten times better than in ACME II [101] and thus eliminated magnetic-field-related noises and systematic effects below the ACME III shot-noise limit. The second effort involves designing and constructing a new coil system facilitated by a novel self-shielding design, which meet stricter magnetic field requirements and significantly reduces fringe fields that potentially magnetize the surrounding magnetic shields. These systems, which reduce magnetic fields to the microgauss level and maintain precise control, are amoung the state-of-the-art achievements [129, 168, 165]. The utility of these systems extends beyond ACME III to applications in fundamental physics measurements, quantum sensing and computing, and advanced biomedical imaging[159, 158].

Enabled by these advances, The ACME experiment is now commissioning a new apparatus that is capable of measuring the electron EDM with an unprecedented sensitivity of $\delta d_e \approx 3.5 \times 10^{-31}\, e \cdot$ cm. This would be an order-of-magnitude improvement over the current best limit [43], and would probe an energy scale of over 100 TeV within the next couple of years.

REFERENCES

1. Gabrielse, G. The standard model's greatest triumph. *Physics Today* **66,** 64–65 (Dec. 2013).
2. Glashow, S. L. Partial-symmetries of weak interactions. *Nuclear Physics* **22,** 579–588 (Feb. 1961).
3. Weinberg, S. A Model of Leptons. *Physical Review Letters* **19,** 1264–1266 (Nov. 1967).
4. Gross, D. J. & Wilczek, F. Asymptotically Free Gauge Theories. I. *Physical Review D* **8,** 3633–3652 (Nov. 1973).
5. Aubert, J. J. t. Experimental Observation of a Heavy Particle J. *Physical Review Letters* **33,** 1404–1406 (Dec. 1974).
6. Perl, M. L. t. Evidence for Anomalous Lepton Production in e^+e^- Annihilation. *Physical Review Letters* **35,** 1489–1492 (Dec. 1975).
7. Herb, S. W. t. Observation of a Dimuon Resonance at 9.5 GeV in 400-GeV Proton-Nucleus Collisions. *Physical Review Letters* **39,** 252–255 (Aug. 1977).
8. Barber, D. P. t. Discovery of Three-Jet Events and a Test of Quantum Chromodynamics at PETRA. *Physical Review Letters* **43,** 830–833 (Sept. 1979).
9. Arnison, G. t. Experimental observation of lepton pairs of invariant mass around 95 GeV/c2 at the CERN SPS collider. *Physics Letters B* **126,** 398–410 (July 1983).

10. Aubert, J. t. The ratio of the nucleon structure functions F_2^N for iron and deuterium. *Physics Letters B* **123,** 275–278 (Mar. 1983).

11. Abachi, S. t. Observation of the Top Quark. *Physical Review Letters* **74,** 2632–2637 (Apr. 1995).

12. Kodama, K. t. Observation of tau neutrino interactions. *Physics Letters B* **504,** 218–224 (Apr. 2001).

13. Collaboration, T. C. Observation of a new boson at a mass of 125 GeV with the CMS experiment at the LHC. *Physics Letters B* **716,** 30–61 (Sept. 2012).

14. Collaboration, T. A. Observation of a new particle in the search for the Standard Model Higgs boson with the ATLAS detector at the LHC. *Physics Letters B* **716,** 1–29 (Sept. 2012).

15. Fan, X., Myers, T. G., Sukra, B. A. D. & Gabrielse, G. Measurement of the Electron Magnetic Moment. *Physical Review Letters* **130** (Feb. 2023).

16. Rubin, V. C. & Ford W. Kent, J. Rotation of the Andromeda Nebula from a Spectroscopic Survey of Emission Regions. *The Astrophysical Journal* **159,** 379 (Feb. 1970).

17. Walsh, D., Carswell, R. F. & Weymann, R. J. 0957 + 561 A, B: twin quasistellar objects or gravitational lens? *Nature* **279,** 381384 (May 1979).

18. Wess, J. & Zumino, B. Supergauge transformations in four dimensions. *Nuclear Physics B* **70,** 3950 (Feb. 1974).

19. Peccei, R. D. & Quinn, H. R. CP Conservation in the Presence of Pseudoparticles. *Physical Review Letters* **38,** 14401443 (June 1977).

20. Milgrom, M. A modification of the Newtonian dynamics as a possible alternative to the hidden mass hypothesis. *The Astrophysical Journal* **270,** 365 (July 1983).

21. Canetti, L., Drewes, M. & Shaposhnikov, M. Matter and antimatter in the universe. *New Journal of Physics* **14,** 095012 (Sept. 2012).

22. Wu, C. S., Ambler, E., Hayward, R. W., Hoppes, D. D. & Hudson, R. P. Experimental Test of Parity Conservation in Beta Decay. *Physical Review* **105,** 1413–1415 (Feb. 1957).

23. Christenson, J. H., Cronin, J. W., Fitch, V. L. & Turlay, R. Evidence for the 2π Decay of the K_2^0 Meson. *Physical Review Letters* **13,** 138–140 (July 1964).

24. Abe, K. t. Observation of Large CP Violation in the Neutral B Meson System. *Physical Review Letters* **87** (Aug. 2001).

25. Aaij, R. t. Observation of CP Violation in Charm Decays. *Physical Review Letters* **122** (May 2019).

26. Sozzi, M. *Discrete Symmetries and CP Violation* ISBN: 9780199296668 (Oxford University Press, Nov. 2007).

27. Lees, J. P. t. Observation of Time-Reversal Violation in the B_0 Meson System. *Physical Review Letters* **109** (Nov. 2012).

28. Khriplovich, I. B. & Lamoreaux, S. K. *CP Violation Without Strangeness* ISBN: 9783642608384 (Springer Berlin Heidelberg, 1997).

29. Kostelecký, V. A. & Russell, N. Data tables for Lorentz and CPT violation. *Reviews of Modern Physics* **83,** 11–31 (Mar. 2011).

30. Gabrielse, G., Hoogerheide, S. F., Dorr, J. & Novitski, E. in *Fundamental Physics in Particle Traps* 1–40 (Springer Berlin Heidelberg, 2014). ISBN: 9783642452017.

31. DiSciacca, J. *et al.* One-Particle Measurement of the Antiproton Magnetic Moment. *Physical Review Letters* **110** (Mar. 2013).

32. Sakharov, A. D. Violation of CP invariance, C asymmetry, and baryon asymmetry of the universe. *Soviet Physics Uspekhi* **34,** 392–393 (May 1991).

33. Griffiths, D. *Introduction to elementary particles* ISBN: 978-3-527-40601-2 (2008).

34. Cabibbo, N. Unitary Symmetry and Leptonic Decays. *Phys. Rev. Lett.* **10,** 531–533 (1963).

35. Engel, J., Ramsey-Musolf, M. J. & van Kolck, U. Electric dipole moments of nucleons, nuclei, and atoms: The Standard Model and beyond. *Progress in Particle and Nuclear Physics* **71,** 21–74 (July 2013).

36. Ema, Y., Gao, T. & Pospelov, M. Standard Model Prediction for Paramagnetic Electric Dipole Moments. *Physical Review Letters* **129** (Nov. 2022).

37. Pospelov, M. E. & Khriplovich, I. B. Electric dipole moment of the W boson and the electron in the Kobayashi-Maskawa model. *Sov. J. Nucl. Phys.* **53,** 638–640 (1991).

38. Yamaguchi, Y. & Yamanaka, N. Large Long-Distance Contributions to the Electric Dipole Moments of Charged Leptons in the Standard Model. *Physical Review Letters* **125** (Dec. 2020).

39. Pendlebury, J. M. t. Revised experimental upper limit on the electric dipole moment of the neutron. *Physical Review D* **92** (Nov. 2015).

40. Graner, B., Chen, Y., Lindahl, E. G. & Heckel, B. R. Reduced Limit on the Permanent Electric Dipole Moment of ^{199}Hg. *Physical Review Letters* **116** (Apr. 2016).

41. Schwinger, J. On Quantum-Electrodynamics and the Magnetic Moment of the Electron. *Physical Review* **73,** 416–417 (Feb. 1948).

42. Fortson, N., Sandars, P. & Barr, S. The Search for a Permanent Electric Dipole Moment. *Physics Today* **56,** 33–39 (June 2003).

43. Roussy, T. S. *et al.* An improved bound on the electron's electric dipole moment. *Science* **381,** 46–50 (July 2023).

44. CERN Yellow Reports: Monographs. *CERN Yellow Reports: Monographs, Vol. 10 (2020): High-Luminosity Large Hadron Collider (HL-LHC): Technical design report* 2020.

45. Schiff, L. I. Measurability of Nuclear Electric Dipole Moments. *Physical Review* **132,** 2194–2200 (Dec. 1963).

46. Sandars, P. The electric dipole moment of an atom. *Physics Letters* **14,** 194–196 (Feb. 1965).

47. Commins, E. D., Jackson, J. D. & DeMille, D. P. The electric dipole moment of the electron: An intuitive explanation for the evasion of Schiff's theorem. *American Journal of Physics* **75,** 532–536 (June 2007).

48. Skripnikov, L. V. Combined 4-component and relativistic pseudopotential study of ThO for the electron electric dipole moment search. *The Journal of Chemical Physics* **145** (Dec. 2016).

49. Denis, M. & Fleig, T. In search of discrete symmetry violations beyond the standard model: Thorium monoxide reloaded. *The Journal of Chemical Physics* **145** (Dec. 2016).

50. Cesarotti, C., Lu, Q., Nakai, Y., Parikh, A. & Reece, M. Interpreting the electron EDM constraint. *Journal of High Energy Physics* **2019** (May 2019).

51. Ramsey, N. F. A Molecular Beam Resonance Method with Separated Oscillating Fields. *Physical Review* **78,** 695–699 (June 1950).

52. Purcell, E. M. & Ramsey, N. F. On the Possibility of Electric Dipole Moments for Elementary Particles and Nuclei. *Physical Review* **78,** 807–807 (June 1950).

53. Shiga, N. & Takeuchi, M. Locking Local Oscillator Phase to the Atomic Phase via Weak Measurement. *New Journal of Physics* **14** (Feb. 2012).

54. Itano, W. M. *et al.* Quantum projection noise: Population fluctuations in two-level systems. *Physical Review A* **47,** 35543570 (May 1993).

55. Salpeter, E. E. Some Atomic Effects of an Electronic Electric Dipole Moment. *Physical Review* **112,** 1642–1648 (Dec. 1958).

56. Wilkinson, D. T. & Crane, H. R. Precision Measurement of the g Factor of the Free Electron. *Physical Review* **130,** 852–863 (May 1963).

57. Nelson, D. F., Schupp, A. A., Pidd, R. W. & Crane, H. R. Search for an Electric Dipole Moment of the Electron. *Physical Review Letters* **2,** 492–495 (June 1959).

58. Goldemberg, J. & Torizuka, Y. Upper Limit of the Electric Dipole Moment of the Electron. *Physical Review* **129,** 2580–2581 (Mar. 1963).

59. Rand, R. E. Determination of the Upper Limit to the Electric Dipole Moment of the Electron at High Momentum Transfer. *Physical Review* **140,** B1605–B1610 (Dec. 1965).

60. Sandars, P. G. H. & Lipworth, E. Electric Dipole Moment of the Cesium Atom. A New Upper Limit to the Electric Dipole Moment of the Free Electron. *Physical Review Letters* **13,** 718–720 (Dec. 1964).

61. Roberts, B. L. & Marciano, W. J. *Lepton Dipole Moments* (WORLD SCIENTIFIC, 2009).

62. Angel, J., Sandars, P. & Tinker, M. Observation of a $v \times E$ effect in an electric dipole moment experiment using a reversible atomic beam machine. *Physics Letters A* **25,** 160–161 (July 1967).

63. Player, M. A. & Sandars, P. G. H. An experiment to search for an electric dipole moment in the $^3P_2$ metastable state of xenon. *Journal of Physics B: Atomic and Molecular Physics* **3,** 1620–1635 (Dec. 1970).

64. Weisskopf, M. C., Carrico, J. P., Gould, H., Lipworth, E. & Stein, T. S. Electric Dipole Moment of the Cesium Atom. A New Upper Limit to the Electric Dipole Moment of the Electron. *Physical Review Letters* **21,** 1645–1648 (Dec. 1968).

65. Murthy, S. A., Krause, D., Li, Z. L. & Hunter, L. R. New limits on the electron electric dipole moment from cesium. *Physical Review Letters* **63,** 965–968 (Aug. 1989).

66. Abdullah, K., Carlberg, C., Commins, E. D., Gould, H. & Ross, S. B. New experimental limit on the electron electric dipole moment. *Physical Review Letters* **65,** 2347–2350 (Nov. 1990).

67. Commins, E. D., Ross, S. B., DeMille, D. & Regan, B. C. Improved experimental limit on the electric dipole moment of the electron. *Physical Review A* **50,** 2960–2977 (Oct. 1994).

68. Regan, B. C., Commins, E. D., Schmidt, C. J. & DeMille, D. New Limit on the Electron Electric Dipole Moment. *Physical Review Letters* **88** (Feb. 2002).

69. Sandars, P. G. H. Measurability of the Proton Electric Dipole Moment. *Physical Review Letters* **19,** 1396–1398 (Dec. 1967).

70. Baron, J *et al.* Order of Magnitude Smaller Limit on the Electric Dipole Moment of the Electron. *Science (New York, N.Y.)* **343,** 269–72 (2014).

71. Hudson, J. J. *et al.* Improved measurement of the shape of the electron. *Nature* **473,** 493–496 (May 2011).

72. Kozlov, M. G. Enhancement of the electric dipole moment of the electron in the YbF molecule. *Journal of Physics B: Atomic, Molecular and Optical Physics* **30,** L607–L612 (Sept. 1997).

73. Denis, M. *et al.* Theoretical study on ThF$^+$, a prospective system in search of time-reversal violation. *New Journal of Physics* **17,** 043005 (Apr. 2015).

74. Petrov, A. N., Mosyagin, N. S., Isaev, T. A. & Titov, A. V. Theoretical study HfF$^+$ in search of the electron electric dipole moment. *Physical Review A* **76** (Sept. 2007).

75. Ng, K. B. *et al.* Spectroscopy on the electron-electric-dipole-moment-sensitive states of ThF^+. *Physical Review A* **105** (Feb. 2022).

76. Lee, J., Meyer, E., Paudel, R., Bohn, J. & Leanhardt, A. An electron electric dipole moment search in the X $^3\Delta_1$ ground state of tungsten carbide molecules. *Journal of Modern Optics* **56,** 2005–2012 (Oct. 2009).

77. Kozlov, M. G. & DeMille, D. Enhancement of the Electric Dipole Moment of the Electron in PbO. *Physical Review Letters* **89** (Sept. 2002).

78. Eckel, S., Hamilton, P., Kirilov, E., Smith, H. W. & DeMille, D. Search for the electron electric dipole moment using Ω doublet levels in PbO. *Physical Review A* **87** (May 2013).

79. Aggarwal, P. *et al.* Measuring the electric dipole moment of the electron in BaF. *The European Physical Journal D* **72** (Nov. 2018).

80. Abe, M., Prasannaa, V. S. & Das, B. P. Application of the finite-field coupled-cluster method to calculate molecular properties relevant to electron electric-dipole-moment searches. *Physical Review A* **97** (Mar. 2018).

81. ACME Collaboration *et al.* Improved Limit on the Electric Dipole Moment of the Electron. *Nature* **562,** 355–360 (2018).

82. ACME Collaboration *et al.* Methods, Analysis, and the Treatment of Systematic Errors for the Electron Electric Dipole Moment Search in Thorium Monoxide. *New Journal of Physics* **19,** 073029 (2016).

83. Zhou, Y. *et al.* Second-Scale Coherence Measured at the Quantum Projection Noise Limit with Hundreds of Molecular Ions. *Physical Review Letters* **124** (Feb. 2020).

84. Alauze, X *et al.* An ultracold molecular beam for testing fundamental physics. *Quantum Science and Technology* **6,** 044005 (July 2021).

85. Ng, K. B. *et al.* Spectroscopy on the electron-electric-dipole-moment-sensitive states ThF^+. *Physical Review A* **105** (Feb. 2022).

86. Collopy, A. L. *et al.* 3D Magneto-Optical Trap of Yttrium Monoxide. *Physical Review Letters* **121** (Nov. 2018).

87. McCarron, D. J., Steinecker, M. H., Zhu, Y. & DeMille, D. Magnetic Trapping of an Ultracold Gas of Polar Molecules. *Physical Review Letters* **121** (July 2018).

88. Williams, H. J. *et al.* Magnetic Trapping and Coherent Control of Laser-Cooled Molecules. *Physical Review Letters* **120** (Apr. 2018).

89. Campbell, S. L. *et al.* A Fermi-degenerate three-dimensional optical lattice clock. *Science* **358,** 90–94 (Oct. 2017).

90. Fitch, N. J., Lim, J, Hinds, E. A., Sauer, B. E. & Tarbutt, M. R. Methods for measuring the electron's electric dipole moment using ultracold YbF molecules. *Quantum Science and Technology* **6,** 014006 (Dec. 2020).

91. Kozyryev, I. & Hutzler, N. R. Precision Measurement of Time-Reversal Symmetry Violation with Laser-Cooled Polyatomic Molecules. *Physical Review Letters* **119** (Sept. 2017).

92. Vutha, A., Horbatsch, M. & Hessels, E. Oriented Polar Molecules in a Solid Inert-Gas Matrix: A Proposed Method for Measuring the Electric Dipole Moment of the Electron. *Atoms* **6,** 3 (Jan. 2018).

93. Vutha, A. C., Horbatsch, M. & Hessels, E. A. Orientation-dependent hyperfine structure of polar molecules in a rare-gas matrix: A scheme for measuring the electron electric dipole moment. *Physical Review A* **98** (Sept. 2018).

94. Shin, S. *et al.* Generation of strong electric fields in an ice film capacitor. *The Journal of Chemical Physics* **139** (Aug. 2013).

95. Vutha, A. C. *et al.* Search for the electric dipole moment of the electron with thorium monoxide. *Journal of Physics B: Atomic, Molecular and Optical Physics* **43,** 074007 (Mar. 2010).

96. Panda, C. D. *et al.* Stimulated Raman adiabatic passage preparation of a coherent superposition of ThO $H^3\Delta_1$ states for an improved electron electric-dipole-moment measurement. *Physical Review A* **93** (May 2016).

97. Ang, D. G. *et al.* Measurement of the $H\ ^3\Delta_1$ radiative lifetime in ThO. *Physical Review A* **106** (Aug. 2022).

98. Wu, X *et al.* Electrostatic focusing of cold and heavy molecules for the ACME electron EDM search. *New Journal of Physics* **24,** 073043 (July 2022).

99. Hiramoto, A. *et al.* SiPM module for the ACME III electron EDM search. *Nuclear Instruments and Methods in Physics Research Section A: Accelerators, Spectrometers, Detectors and Associated Equipment* **1045,** 167513 (Jan. 2023).

100. Lasner, Z. *Order-of-Magnitude-Tighter Bound on the Electron Electric Dipole Moment.* PhD thesis (Yale University, 2019).

101. Panda, C. *Order of magnitude improved limit on the electric dipole moment of the electron* PhD thesis (Harvard University, 2018).

102. Brown, J. M. & Carrington, A. *Rotational Spectroscopy of Diatomic Molecules* (Cambridge University Press, 2003).

103. Demtroder, W. Molecular Physics. Theoretical Principles and Experimental Methods. *Angewandte Chemie International Edition* **45,** 5733–5734 (Sept. 2006).

104. Petrov, A. N. *et al.* Zeeman interaction in ThO for the Electron Electric Dipole Moment search. *Physical Review A* **89** (June 2014).

105. Spaun, B. N. *A Ten-Fold Improvement to the Limit of the Electron Electric Dipole Moment* PhD thesis (Harvard University, 2014).

106. Bickman, S., Hamilton, P., Jiang, Y. & DeMille, D. Preparation and detection of states with simultaneous spin alignment and selectable molecular orientation in PbO. *Phys. Rev. A* **80,** 023418 (2009).

107. Eckel, S., Hamilton, P., Kirilov, E., Smith, H. W. & DeMille, D. Search for the electron electric dipole moment using Ω-doublet levels in PbO. *Phys. Rev. A* **87,** 1–19 (2013).

108. Kirilov, E. *et al.* Shot-noise-limited spin measurements in a pulsed molecular beam. *Phys. Rev. A* **88,** 013844 (2013).

109. Hutzler, N. R., Lu, H. I. & Doyle, J. M. The buffer gas beam: An intense, cold, and slow source for atoms and molecules. *Chem. Rev.* **112,** 4803–4827 (2012).

110. Hutzler, N. R. *et al.* A cryogenic beam of refractory, chemically reactive molecules with expansion cooling. *Phys. Chem. Chem. Phys.* **13,** 18976 (2011).

111. Patterson, D. & Doyle, J. M. Bright, guided molecular beam with hydrodynamic enhancement. *J. Chem. Phys.* **126,** 1–6 (2007).

112. Hutzler, N. *A New Limit on the Electron Electric Dipole Moment: Beam Production, Data Interpretation, and Systematics* PhD thesis (Harvard University, 2014).

113. Meisenhelder, C. *Advances in the Measurement of the Electron Electric Dipole Moment* PhD thesis (Harvard University, 2023).

114. West, A. D. *et al.* An Underappreciated Radiation Hazard from High Voltage Electrodes in Vacuum. *Health Physics* **112,** 33–41 (Jan. 2017).

115. Wu, X *et al.* The metastable Q $^3\Delta_2$ state of ThO: a new resource for the ACME electron EDM search. *New Journal of Physics* **22,** 023013 (Feb. 2020).

116. Kokkin, D. L., Steimle, T. C. & DeMille, D. Branching ratios and radiative lifetimes of the U, L, I states of thorium oxide. *Physical Review A* **90** (Dec. 2014).

117. Kokkin, D. L., Steimle, T. C. & DeMille, D. Characterization of the $I(\Omega = 1) - X^1\Sigma^+(0,0)$ band of thorium oxide. *Physical Review A* **91** (Apr. 2015).

118. Hamamatsu. *Photomultiplier tube R7600U-300*

119. Sul, W.-S., Lee, C.-H. & Cho, G.-S. Influence of Guard-Ring Structure on the Dark Count Rates of Silicon Photomultipliers. *IEEE Electron Device Letters* **34,** 336–338 (Mar. 2013).

120. Hampel, M. *et al.* Optical crosstalk in SiPMs. *Nuclear Instruments and Methods in Physics Research Section A: Accelerators, Spectrometers, Detectors and Associated Equipment* **976,** 164262 (Oct. 2020).

121. Masuda, T. *et al.* Suppression of the optical crosstalk in a multi-channel silicon photomultiplier array. *Optics Express* **29,** 16914 (May 2021).

122. Masuda, T. *et al.* High-sensitivity low-noise photodetector using a large-area silicon photomultiplier. *Optics Express* **31,** 1943 (Jan. 2023).

123. Ang, D. G. *Progress towards an improved measurement of the electric dipole moment of the electron* PhD thesis (Harvard University, 2023).

124. O'Leary, B. R. *In Search of the Electron's Electric Dipole Moment in Thorium Monoxide: An Improved Upper Limit, Systematic Error Models, and Apparatus Upgrades.* PhD thesis (Yale University, 2017), 266. ISBN: 9780355105513.

125. Hao, B. & Kovács, I. A. A positive statistical benchmark to assess network agreement. *Nature Communications* **14** (May 2023).

126. Meng, X., Hao, B., Ráth, B. & Kovács, I. A. *Path Percolation in Quantum Communication Networks* 2024.

127. Panda, C. D. *et al.* Attaining the shot-noise-limit in the ACME measurement of the electron electric dipole moment. *Journal of Physics B: Atomic, Molecular and Optical Physics* **52,** 235003 (Nov. 2019).

128. Altarev, I. *et al.* A large-scale magnetic shield with 10^6 damping at millihertz frequencies. *Journal of Applied Physics* **117,** 183903 (May 2015).

129. Afach, S. *et al.* Dynamic stabilization of the magnetic field surrounding the neutron electric dipole moment spectrometer at the Paul Scherrer Institute. *Journal of Applied Physics* **116,** 084510 (Aug. 2014).

130. Liu, S. *et al.* Compact Actively-Shielded Magnetic Field Coil within Mu-Metal Shields (2024).

131. Petrov, A. N. ac Stark effect in ThO $H\ ^3\Delta_1$ for the electron electric-dipole-moment search. *Physical Review A* **91** (June 2015).

132. Vutha, A. C. *A search for the electric dipole moment of the electron using thorium monoxide* PhD thesis (Yale University, 2011).

133. Vutha, A. & DeMille, D. Geometric phases without geometry (2009).

134. Yashchuk, V. V., Lee, S.-K. & Paperno, E. in *Optical Magnetometry* (eds Budker, D. & Jackson Kimball, D. F.) 225–248 (Cambridge University Press, 2013).

135. Rowland, H. A. XIV. On magnetic permeability, and the maximum of magnetism of iron, steel, and nickel. *The London, Edinburgh, and Dublin Philosophical Magazine and Journal of Science* **46,** 140–159 (Aug. 1873).

136. Mager, A. Magnetic shields. *IEEE Transactions on Magnetics* **6,** 67–75 (Mar. 1970).

137. Thomas, A. Magnetic Shielded Enclosure Design in the DC and VLF Region. *IEEE Transactions on Electromagnetic Compatibility* **EMC-10,** 142–152 (Mar. 1968).

138. Paperno, E., Peliwal, S., Romalis, M. V. & Plotkin, A. Optimum shell separation for closed axial cylindrical magnetic shields. *Journal of Applied Physics* **97** (May 2005).

139. Paperno, E., Koide, H. & Sasada, I. A new estimation of the axial shielding factors for multishell cylindrical shields. *Journal of Applied Physics* **87,** 5959–5961 (May 2000).

140. Sumner, T. J., Pendlebury, J. M. & Smith, K. F. Conventional magnetic shielding. *Journal of Physics D: Applied Physics* **20,** 1095–1101 (Sept. 1987).

141. Magnetic Shield Corp. *Co-NETIC AA Perfection Sheet*

142. Altarev, I. *et al.* Minimizing magnetic fields for precision experiments. *Journal of Applied Physics* **117** (June 2015).

143. Sun, Z., Schnabel, A., Burghoff, M. & Li, L. Calculation of an optimized design of magnetic shields with integrated demagnetization coils. *AIP Advances* **6** (July 2016).

144. Sun, Z. *et al.* Dynamic modeling of the behavior of permalloy for magnetic shielding. *Journal of Applied Physics* **119** (May 2016).

145. Arpaia, P. *et al.* Magnetic characterization of Mumetal® for passive shielding of stray fields down to the nano-Tesla level. *Nuclear Instruments and Methods in Physics Research Section A: Accelerators, Spectrometers, Detectors and Associated Equipment* **988,** 164904 (Feb. 2021).

146. Kasiraj, P., Shelby, R., Best, J. & Horne, D. Magnetic domain imaging with a scanning Kerr effect microscope. *IEEE Transactions on Magnetics* **22,** 837839 (Sept. 1986).

147. Huang, K.-x. *et al.* Anisotropic imaging for the highly efficient crystal orientation determination of two-dimensional materials. *Journal of Materials Chemistry C* **7,** 59455953 (2019).

148. Moskowitz, B. M. *Hitchhiker's Guide to Magnetism* in (2002).

149. Magnetic Shield Corp. *Perfection Annealing*

150. Heanjia Super Metals Co., Ltd. *Mumetal alloy for magnetic shielding devices*

151. Thiel, F., Schnabel, A., Knappe-Grüneberg, S., StollfuSS, D. & Burghoff, M. Demagnetization of magnetically shielded rooms. *Review of Scientific Instruments* **78** (Mar. 2007).

152. Jiles, D. C. & Atherton, D. L. Theory of ferromagnetic hysteresis (invited). *Journal of Applied Physics* **55,** 2115–2120 (Mar. 1984).

153. Jiles, D. & Atherton, D. Theory of ferromagnetic hysteresis. *Journal of Magnetism and Magnetic Materials* **61,** 48–60 (Sept. 1986).

154. Peng, X. *et al.* Jiles-Atherton model prediction and compensation of the hysteresis inside magnetic shields. *AIP Advances* **9** (Mar. 2019).

155. Nagashima, K., Sasada, I. & Tashiro, K. High-performance bench-top cylindrical magnetic shield with magnetic shaking enhancement. *IEEE Transactions on Magnetics* **38,** 3335–3337 (Sept. 2002).

156. Kelha, V., Peltonen, R. & Rantala, B. The effect of shaking on magnetic shields. *IEEE Transactions on Magnetics* **16,** 575–578 (July 1980).

157. Shah, V., Osborne, J., Orton, J. & Alem, O. *Fully integrated, standalone zero field optically pumped magnetometer for biomagnetism* in *Steep Dispersion Engineering and Opto-Atomic Precision Metrology XI* (eds Shahriar, S. M. & Scheuer, J.) (SPIE, Feb. 2018).

158. *et al.*, H. A lightweight magnetically shielded room with active shielding. *Scientific Reports* **12** (Aug. 2022).

159. Bork, J., Hahlbohm, H., Klein, R. & Schnabel, A. *The 8-layered magnetically shielded room of the PTB: Design and construction* in (Jan. 2001).

160. Gabrielse, G. & Tan, J. Self-shielding superconducting solenoid systems. *Journal of Applied Physics* **63,** 5143–5148 (May 1988).

161. Gabrielse, G *et al.* A superconducting solenoid system which cancels fluctuations in the ambient magnetic field. *Journal of Magnetic Resonance (1969)* **91,** 564–572 (Feb. 1991).

162. Hawksworth, D., McDougall, I., Bird, J. & Black, D. Considerations in the design of MRI magnets with reduced stray fields. *IEEE Transactions on Magnetics* **23,** 1309–1314 (1987).

163. Ishiyama, A., Hondoh, M., Ishida, N. & Onuki, T. Optimal design of MRI magnets with magnetic shielding. *IEEE Transactions on Magnetics* **25,** 1885–1888 (1989).

164. Crawford, C. & Shin, Y. *A method for designing coils with arbitrary fields* tech. rep. (University of Kentucky, 2009).

165. Martin, E. & Crawford, C. *A Double Cosine Theta Coil Prototype* tech. rep. (University of Kentucky, 2010).

166. Crawford, C. B. The physical meaning of the magnetic scalar potential and its use in the design of hermetic electromagnetic coils. *Review of Scientific Instruments* **92** (Dec. 2021).

167. Chubar, O., Elleaume, P. & Chavanne, J. A three-dimensional magnetostatics computer code for insertion devices. *Journal of Synchrotron Radiation* **5,** 481–484 (May 1998).

168. Slutsky, S. *et al.* Cryogenic magnetic coil and superconducting magnetic shield for neutron electric dipole moment searches. *Nuclear Instruments and Methods in Physics Research Section A: Accelerators, Spectrometers, Detectors and Associated Equipment* **862,** 36–48 (2017).